

9-20-2018

Modelling, Design, and Optimization of Membrane based Heat Exchangers for Low-grade Heat and Water Recovery

Soheil Soleimanikutanaei
ssole016@fiu.edu

Follow this and additional works at: <https://digitalcommons.fiu.edu/etd>



Part of the [Heat Transfer, Combustion Commons](#)

Recommended Citation

Soleimanikutanaei, Soheil, "Modelling, Design, and Optimization of Membrane based Heat Exchangers for Low-grade Heat and Water Recovery" (2018). *FIU Electronic Theses and Dissertations*. 3921.
<https://digitalcommons.fiu.edu/etd/3921>

This work is brought to you for free and open access by the University Graduate School at FIU Digital Commons. It has been accepted for inclusion in FIU Electronic Theses and Dissertations by an authorized administrator of FIU Digital Commons. For more information, please contact dcc@fiu.edu.

FLORIDA INTERNATIONAL UNIVERSITY

Miami, Florida

MODELING, DESIGN, AND OPTIMIZATION OF MEMBRANE BASED HEAT
EXCHANGERS FOR LOW-GRADE HEAT AND WATER RECOVERY

A dissertation submitted in partial fulfillment of the

requirements for the degree of

DOCTOR OF PHILOSOPHY

in

MECHANICAL ENGINEERING

by

Soheil Soleimanikutanaei

2018

To: Dean John L. Volakis
College of Engineering and Computing

This dissertation, written by Soheil Soleimanikutanaei, and entitled Modeling, Design, and Optimization of Membrane Based Heat Exchangers for Low-grade Heat and Water Recovery, having been approved in respect to style and intellectual content, is referred to you for judgment.

We have read this dissertation and recommend that it be approved.

Yiding Cao

Norman Munroe

Ali Siahpush

Gang Quan

Nezih Pala

Cheng-Xian Lin, Major Professor

Date of Defense: September 20, 2018

The dissertation of Soheil Soleimanikutanaei is approved.

Dean John L. Volakis
College of Engineering & Computing

Andrés G. Gil
Vice President for Research and Economic Development
and Dean of the University Graduate School

Florida International University, 2018

© Copyright 2018 by Soheil Soleimanikutanaei

All rights reserved.

DEDICATION

I dedicate this thesis to my parents, brothers, and friends. Without their patience, understanding, support, and most of all love, the completion of this work would not have been possible.

ACKNOWLEDGMENTS

I wish to thank the members of my committee for their support, guidance and valuable suggestions. Here I will appreciate the time and dedication of Dr. Gang Quan and Dr. Nezhil Pala from the Department of Electrical & Computer Engineering, Prof. Yiding Cao and Prof. Norman Munroe from the Department of Mechanical & Materials Engineering and Dr. Ali Siahpush from the Department of Engineering & Technology at Southern Utah University. My special thanks go to my major advisor Dr. Cheng-Xian (Charlie) Lin for his constant support, time and guidance. I am also grateful for the financial support of the Florida International University for the Doctoral Evidence Acquisition and Dissertation Year Fellowships. In addition, I would like to acknowledge the financial support from the Industrial Technologies Program of the U.S. Department of Energy as well as Gas Technology Institute (GTI). This work would not be possible without the technical support and consultant of Dr. Dexin Wang from GTI. Finally, I want to extend my appreciation to all the faculty members and staff of the Department of Mechanical and Materials Engineering at Florida International University.

ABSTRACT OF THE DISSERTATION

MODELING, DESIGN, AND OPTIMIZATION OF MEMBRANE BASED HEAT
EXCHANGERS FOR LOW-GRADE HEAT AND WATER RECOVERY

by

Soheil Soleimanikutanaei

Florida International University, 2018

Miami, Florida

Professor Cheng-Xian Lin, Major Professor

Transport Membrane Condenser (TMC) is an innovative technology based on the property of a nano-scale porous material which can extract both waste heat and water from exhaust gases. This technology tremendously improves the efficiency of boilers and gas/coal combustors by lowering waste heat and increasing water recovery. Contaminants in the flue gases, such as CO₂, O₂, NO_x, and SO₂ are inhibited from passing through the membrane by the membrane's high selectivity. The condensed water through these tubes is highly pure and can be used as the makeup water for many industrial applications. The goal of this research is to investigate the heat transfer, condensation rate, pressure drop and overall performance of crossflow heat exchangers. In this research, a numerical model has been developed to predict condensation of water vapor over and inside of nano-porous layers. Both capillary condensation inside the nanoscale porous structure of the TMC and the surface condensation were considered in the proposed method using a semi-empirical model. The transport of the water vapor and the latent heat of condensation were applied in the numerical model using the pertinent mass, momentum, turbulence and energy equations.

By using the proposed model and simulation procedure, the effect of various inlet parameters such as inlet mass flow rate, inlet temperature, and water vapor content of the inlet flow on the performance of the cross-flow TMC heat exchanger was studied to obtain the optimum performance of the heat exchangers at different working conditions. The performance of the TMC heat exchangers for inlet flue gas rate 40 to 120 kg/h, inlet water rate 60 to 140 kg/h, inlet flue gas relative humidity 20 to 90%, and tube pitch ratio 0.25 to 2.25 has been studied. The obtained results show that the water condensation flux continuously increases with the increase of the inlet flue-gas flow rate, water flow rate, and the flue-gas humidity. The total heat flux also follows the same trend due to the pronounced effect of the latent heat transfer from the condensation process. The water condensation flux and the overall heat transfer increase at the beginning for small values of the tube pitches and then decreases as the tube pitch increases furthermore.

In addition to the cross-flow TMC heat exchangers, the performance of a shell and tube TMC heat exchanger for high pressure and temperature oxy-combustion applications has been investigated. The performance analysis for a 6-heat exchanger TMC unit shows that heat transfer of the 2-stage TMC unit is higher than the 2-stage with the same number of the heat exchanger in each unit.

TABLE OF CONTENTS

CHAPTER	PAGE
1. Chapter 1: Introduction to Waste Heat Recovery	1
1.1. Waste heat recovery, importance, and opportunities	1
1.2. Heat quality, and grade	2
1.3. Typical waste heat streams in plant perations.....	4
1.4. Condensation and heat transfer over tube walls.....	8
1.5. TMC heat exchangers	9
1.6. Limitation of the existing research and present contribution.....	19
1.7. Proposed research approach.....	20
1.8. Outline of the Dissertation	21
2. Chapter 2: Thermodynamic Properties and Governing Equations	23
1.9. Numerical simulation of condensation phenomena on a solid wall.....	28
1.10. Thermodynamic properties of mixtures and species.....	29
1.11. Thermophysical properties of the multi-component mixture.....	35
1.12. Governing equations	38
1.13. Turbulence modeling	39
1.14. Standard $k - \varepsilon$ and $RNG - k - \varepsilon$ Models.....	39
1.15. Shear-Stress Transport (SST) $k - \omega$ Model.....	42
1.16. Condensation model.....	45
1.17. Wall condensation using fully resolved boundary layer approach	45
1.18. Wall condensation using wall function approach	48
1.19. Volumetric condensation	50
1.20. Numerical validation and implementation.....	51
1.21. Validation of condensation rate against an analytical solution	52
1.22. Validation of heat flux on a condensing wall	55
3. Chapter 3: Modeling and simulation procedure for TMC heat exchangers.....	57
1.23. Laboratory investigation and numerical simulations	57
1.24. Critical dimensions and Schematic of the experimental apparatus.....	58
1.25. Boundary conditions and thermodynamic properties	61
1.26. Thermodynamic properties of the flue-gas mixture.....	64
1.27. Turbulence model	66

1.28.	Thermophysical properties of the TMC tubes	66
1.29.	Condensation model for the TMC heat exchanger and simulation algorithm	68
1.30.	Numerical simulation of the heat and mass transfer in a TMC heat exchanger.....	70
4.	Chapter 4: Mixed condensation model	80
1.31.	Adsorption and desorption.....	80
1.32.	Transport of an adsorbable gas in nanopores.....	81
	Viscous flow of the gas phase.....	81
	Knudsen flow of the gas phase	82
	Transition Flow in the Gas Phase	82
1.33.	Flow in the Capillary Condensate.....	83
	Capillary action.....	83
	Capillary pressure	84
1.34.	Modeling of condensation in TMC heat exchangers	85
1.35.	Condensation of condensable gas over and inside the nanoporous layers.....	86
5.	Chapter 5: Parametric Study of Optimum Performance	92
1.36.	Parametric study of a cross-flow TMC heat exchanger.....	92
1.37.	Effect of inlet flue-gas flow rate	93
1.38.	Effect of inlet water flow rate	94
1.39.	Effect of inlet flue-gas temperature	96
1.40.	Effect of inlet water temperature	97
1.41.	Effect of inlet flue-gas relative humidity	98
1.42.	Effect of tube pitch.....	100
1.43.	Tube pitch effect on the TMC volumetric heat transfer.....	101
6.	Chapter 6: Waste heat and water recovery from pressurized oxy-coal systems	105
1.44.	Pressurized oxy-coal combustion.....	105
1.45.	Critical dimensions for the shell and tube heat exchanger.....	106
1.46.	Numerical modeling of shell and tube TMC unit	108
1.47.	Effect of working conditions on the performance of the TMC unit.....	114
7.	Chapter 7: Conclusion and recommendations	120
	References.....	123
	Appendix.....	129
	VITA.....	134

LIST OF TABLES

TABLE	PAGE
Table 1. Typical flow temperature in industrial applications [3].....	3
Table 2. Summary of TMC potential application and possible savings [16].....	12
Table 3. The coefficient of the polynomial expansion for dynamic viscosity.....	30
Table 4. The coefficient of the polynomial expansion for thermal conductivity.....	30
Table 5. Coefficients of the polynomial expansion for vapor heat capacity.....	31
Table 6. Parameters for wall condensation over a flat plate in laminar forced convection flow...	52
Table 7. Critical dimensions of the test section.....	61
Table 8. Critical dimensions of the tubes and bundle arrangement.....	61
Table 9. Summary of the different zones and boundary conditions in the numerical setup.....	62
Table 10. Typical experimental results for the lab scale TMC rig.....	63
Table 11. Inlet mass fraction of different species for the flue-gas.....	64
Table 12. Thermodynamic properties of the other non-condensable species.....	65
Table 13. Dimensions and physical properties of different types of TMC tubes.....	67
Table 14. Boundary and working conditions for the computational model.....	72
Table 15. Inlet and outlet conditions for the experimental cases 1-6.....	73
Table 16. Inlet and outlet conditions for the experimental cases 7-11.....	75
Table 17. Membrane Bundle Dimensions/Specifications.....	106
Table 18. Off-design performance of the TMC shell and tube heat exchanger.....	118
Table 19. List of the UDFs which have been used in the numerical simulation.....	132

LIST OF FIGURES

FIGURE	PAGE
Figure 1. Energy loss during the power generation process[2].....	1
Figure 2. Schematic of a recuperator and the combustion chamber [4].....	5
Figure 3. Application of a waste heat boiler [4].	6
Figure 4. Application of heat wheels in low and medium temperature waste heat [4].	6
Figure 5. Schematic of an absorption system for waste heat recovery [4].....	7
Figure 6. Photomicrograph of TMC membrane cross-section [16].	13
Figure 7. Membrane transport mode effect [16].	14
Figure 8. Schematic of water transport concept in TMC tubes [16].	15
Figure 9. TMC concept (main component α alumina) [16].	16
Figure 10. Photo of (a) stainless steel based substrates and (b) ceramic based substrates.	17
Figure 11. Schematic of low-grade heat and water recovery in a 2-stage TMC system [16].	18
Figure 12. Computational domain and grid for laminar wall condensation problem.	54
Figure 13. Condensation flux for at 1 m/s over an isothermal flat plate at 364.81 K, MF=0.05... 55	55
Figure 14. Validation of heat flux on the condensing wall.	56
Figure 15. Experimental rig and the test section for the lab scale TMC heat exchangers.	58
Figure 16. Lab scale TMC heat exchanger [1].	59
Figure 17. Schematic of experimental apparatus [25].	60
Figure 18. Schematic of the tube arrangement.	60
Figure 19. Schematic of the computational domain and boundary conditions.	62
Figure 20. Heat and mass transfer coefficient of TMC and stainless-steel heat exchangers.	69
Figure 21. Schematic of different zones in the numerical setup.	70
Figure 22. Geometry and computational grid for the lab scale TMC module.	72
Figure 23. Grid independence study for the cross-flow heat TMC heat exchanger modeling.	73
Figure 24. Comparison between the numerical simulation and experimental data.	77

Figure 25. Temperature and water vapor mass fraction contours for cases 1, 5 and 9.	78
Figure 26. Deviation of numerical prediction from the experimental results.	79
Figure 27. Adsorption and capillary condensation [80].....	83
Figure 28. Capillary action and the pressure at different points [80].....	84
Figure 29. Pressure condition for in a multilayer pore configuration with one meniscus.	87
Figure 30. Comparison of numerical simulation results with the experimental data [26].	90
Figure 31. Comparison between the results of the mixed model with the experimental data.....	91
Figure 32. Effect of inlet conditions on the performance of TMC unit.	94
Figure 33. Effect of inlet water flow rate on the water and heat recovery efficiency.....	95
Figure 34. Effect of inlet flue-gas temperature on the water and heat recovery efficiency.	96
Figure 35. Effect of inlet water temperature on the water and heat recovery efficiency.	97
Figure 36. Effect of flue-gas relative humidity on the water and heat recovery efficiency.	99
Figure 37. Effect of tube pitch on the water and heat recovery efficiency.	100
Figure 38. Effect of inlet humidity and tubes pitch on the heat transfer and Euler number.	102
Figure 39. Effect of tube spacing and humidity on temperature and vapor mass fraction.....	104
Figure 40. TMC Bundle Fabrication Layout [84].....	105
Figure 41. Pilot test module of the TMC shell and tube heat exchangers [84].	106
Figure 42. a) TMC Test System Configuration and Installation [84]	107
Figure 43. 2 and 3 stage configurations of the shell and tube TMC heat exchanger unit.....	108
Figure 44. The contour of temperature on the TMC walls.	110
Figure 45. The contour of heat flux on the TMC walls.	111
Figure 46. Heat transfer and condensation rate at each stage of the heat exchanger unit.....	112
Figure 47. Heat transfer and condensation rate for 2 and 3 stage TMC units.....	113
Figure 48. Comparison of the outlet temperatures between the 2 and 3 stage TMC units.	114
Figure 49. Effect of inlet cooling water flow rate.....	115

Figure 50. Effect of inlet flue-gas flow rate..... 116

Figure 51. Effect of inlet cooling water temperature. 117

Figure 52. (a) design condition (b) FG temperature +30°F, (c) FG flow rate +50%..... 119

ABBREVIATIONS AND ACRONYMS

A	Cell surface area (m^2)
B	Bird suction parameter
C	Correction factor for the condensation rate
D	Species mass diffusivity (m^2/s)
h	Vapor latent enthalpy (J/kg)
J	Condensation flux ($\text{kg}/\text{h}/\text{m}^2$)
M	Molar mass (kg/mol)
p	Pressure (Pa)
q	Heat flow (J/s)
R	Gas constant ($\text{J}/\text{mol}/\text{K}$)
T	Temperature (K)
t	Time (s)
\vec{u}	Velocity vector (m/s)
V	Cell volume (m^3)
Y	Species mass fraction

Greek Letters

μ	Viscosity
ρ	Fluid density (kg/m^3)
k	Turbulence kinetic energy [J/kg]

ε	Dissipation rate [J/kg.s]
λ	Thermal conductivity [W/m.K]
α	Permittivity
τ	Tortuosity
η	Efficiency

Subscripts or Superscripts

<i>cap</i>	Capillary
<i>cell</i>	Computational cell properties
<i>fg</i>	Fluid to gas
<i>hr</i>	Hours
<i>i</i>	Inner
<i>in</i>	Inlet
<i>min</i>	Minimum
<i>max</i>	Maximum
<i>m</i>	Mean
<i>out</i>	Outlet
<i>s</i>	Steam

1. Chapter 1: Introduction to Waste Heat Recovery

1.1. Waste heat recovery, importance, and opportunities

Thermal loss from heat processing equipment can waste energy and reduce productivity which account for over ten quadrillions Btu of energy each year in the US industry which represents about 30.8% of the total energy used in the US [1]. As an example, in natural gas-fired industrial process units such as boilers, kilns, ovens, and furnaces, waste heat exits the units and devices. Based on the report published by the US Department of energy [2], energy loss during the power generation process is one of the significant opportunities for the waste recovery technologies in the US industries (Figure 1).

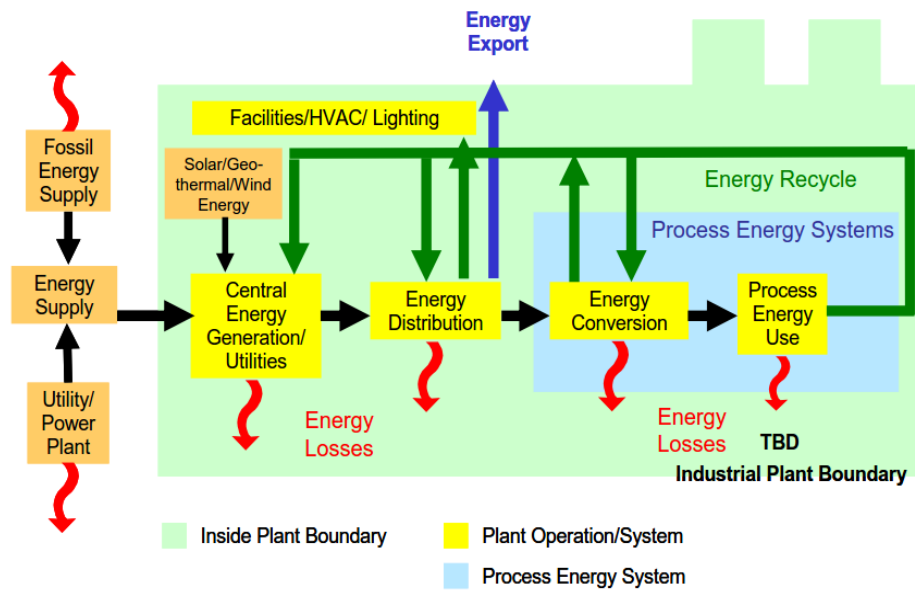


Figure 1. Energy loss during the power generation process[2].

The advantages of waste heat recovery in power plant and other industrial processes include the following:

- Fuel cost reduction and increasing of the efficiency.
- Reduction of pollutions such as SO_x, NO_x, CO, CO₂ and other unburned hydrocarbons.

- Size reduction or elimination of cooling-water and air cooler.
- Achieving higher flame temperatures by using the preheated air.

1.2. Heat quality, and grade

The quality and grade of waste heat in an industrial process can be categorized based on the temperature of the flow stream in that process. The total available energy for the recovery purpose can be estimated as follow:

$$\dot{Q}_{total} = \dot{Q}_{sensible} + \dot{Q}_{latent} \quad (1)$$

where the sensible and latent heat of the process are:

$$\dot{Q}_{sensible} = \rho VA c_p \Delta T, \quad \dot{Q}_{latent} = \dot{m} h_{fg} \quad (2)$$

A (ft²) is the cross-sectional area, V (ft/s) is the flow velocity, ρ (lb/ft³) is the density of the fluid, c_p (BTU/lb.F^o) is the specific heat capacity, and ΔT (F^o) is the temperature difference between heat source and heat sink. \dot{m} (lb/s) and h_{fg} (BTU/lb) are the mass flow rate of the condensable gas and latent heat of condensation respectively. The waste heat in a process is based on the flow stream temperature and can be categorized into the following grades:

- Ultra-low temperature: for flow stream below 250°F.
- Low temperature: 250°–450°F.
- Medium temperature: 450°–1,200°F.
- High temperature: 1,200°–1,600°F.
- Ultra-high temperature: >1,600°F.

The temperature range and characteristics for some of the industrial waste heat sources are summarized in Table 1.

Table 1. Typical flow temperature in industrial applications [3].

High temperature	
Types of Device	Temperature, °C
Nickel refining furnace	1370 –1650
Aluminum refining furnace	650-760
Zinc refining furnace	760-1100
Copper refining furnace	760- 815
Steel heating furnaces	925-1050
Copper reverberatory furnace	900-1100
Open hearth furnace	650-700
Cement kiln (Dry process)	620- 730
Glass melting furnace	1000-1550
Hydrogen plants	650-1000
Solid waste incinerators	650-1000
Fume incinerators	650-1450
Medium temperature	
Gas turbine exhausts	370-540
Reciprocating engine exhausts	315-600
Reciprocating engine exhausts (turbo charged)	230- 370
Heat treating furnaces	425 - 650
Drying and baking ovens	230 - 600
Annealing furnace cooling systems	425 - 650
Low temperature	
Process steam condensate	55-88
Cooling water from: Furnace doors	32-55
Injection molding machines	32-88
Annealing furnaces	66-230
Forming Dies	27-88
Pumps	27-88

Internal combustion engines	66-120
Air conditioning	32-43
Liquid still condensers	32-88
Drying, baking and curing ovens	93-230
Hot processed liquids	32-232
Hot processed solids	93-232

1.3. Typical waste heat streams in plant operations

Based on the working fluid in the waste heat recovery processes in power plants the conventional heat recovery methods can be categorized into two different groups:

a) Exhaust Gases or Vapors:

These processes include high-temperature gases leaving a combustor; hot air or flue gases containing some amount of moisture; make-up air which has been mixed with combustion products or large amounts of water vapor combined with small amounts of other non-condensable gases

b) Heated Water or Liquid:

Discharged heated water from cooling systems; particulate hot water and hot water containing dissolved gases are some of the commonly used waste heat recovery systems in different industrial processes[4].

Recuperator

In a recuperator, heat transfer happens between the hot flue gases and inlet air using metallic or ceramic walls (see Figure 2).

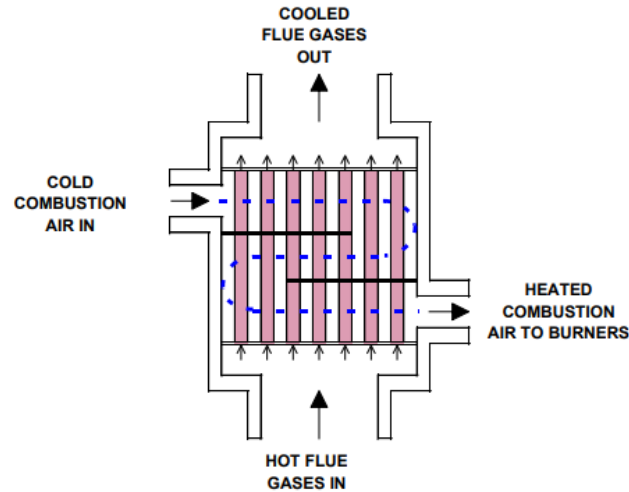


Figure 2. Schematic of a recuperator and the combustion chamber [4].

Hybrid recuperators can also be used to recover heat through the radiation in addition to the convection and conduction mechanisms. The ceramic tube in the recuperator has been used to overcome the temperature limitations of metallic recuperators.

Regenerators:

Glass and steel melting industries are the primary consumers of regenerators. Regenerators can recover heat from high-temperature exhaust gases, generally above 2,500°F (1,370°C). The regenerators are usually made of high-temperature refractory bricks or specially designed ceramic shapes. The efficiency and performance of the regenerators are highly depend on the time span between the reversals. The bricks in regenerators are heated up during the high-temperature cycle and release the absorbed heat during the next period.

Waste heat boiler application for gas turbine exhaust gases

The waste heat can also be used directly for power generation application. The exhaust gas from a gas turbine can be used to generate high-pressure steam to run a steam turbine (Figure 3)

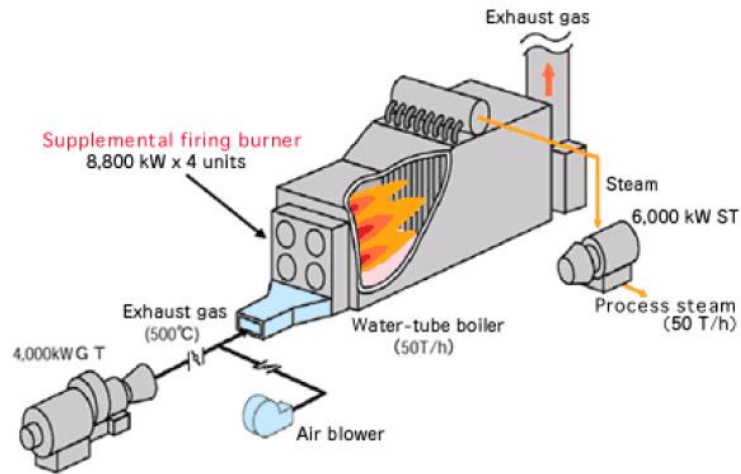


Figure 3. Application of a waste heat boiler [4].

Heat wheels

A heated wheel is a metallic disk that rotates slowly and transfers heat between the hot and cold stream using its high thermal capacity (Figure 4). The working limits of the heat wheels are usually 600°F (315°C) and work in low- to medium-temperature waste heat recovery systems. The overall efficiency of sensible heat transfer of this kind of regenerator can be as high as 85%.

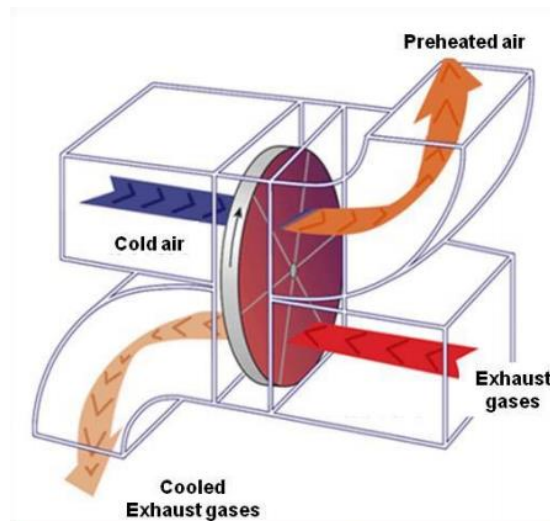


Figure 4. Application of heat wheels in low and medium temperature waste heat [4].

Heat pipe

Heat pipes can transfer heat between the hot and cold medium using the condensation/evaporation process with the help of capillary pressure in a porous medium. They can be used to recover waste heat by installing them between a hot and cold flow stream. The working fluid inside the heat pipe transfers heat from the hot stream to the cold stream by evaporation and condensation respectively.

Absorption chillers

Waste heat can be used as a heat source in an absorption system. As seen in Figure 5 Ammonia–water can be used in different application such as small refrigerators or large heat-recovery machines installed in power plants.

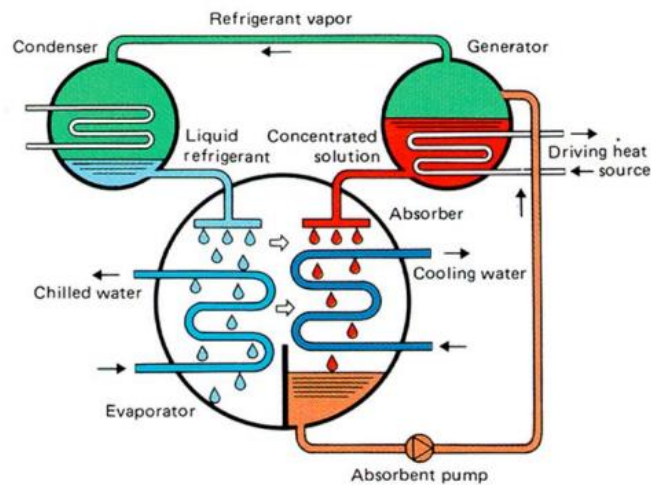


Figure 5. Schematic of an absorption system for waste heat recovery [4].

Thermo-electric power generation

Thermoelectric generators (TEG) [5] can directly convert the heat waste to electricity using the electrical properties of semiconductor materials. TE materials produce electricity when joined together and subjected to a temperature difference across the junctions.

1.4. Condensation and heat transfer over tube walls

Single and multiphase flow over tube walls has been studied extensively by many researchers both numerically and empirically in the past. Browne and Bansal [6] reviewed the heat transfer characteristics of shell and tube and tube bundles condensing heat exchangers. They also cited numerous experimental studies on the effects of surface geometry, condensate inundation, vapor shear, and gravity. Osakabe et al. [7] investigated condensation heat transfer on horizontal stainless-steel tubes experimentally. They used an actual flue gas from a natural gas boiler in their experiment. They conducted their investigation at different air ratios of the flue gas and a wide range of tube wall temperatures. The results revealed that by decreasing the wall temperature, the wall region covered as a thin liquid film increased.

Zhou et al. [8] studied steam condensation in a vertical tube bundle passive condenser operating in a through flow mode experimentally. The experiments were carried out for various system pressures, inlet steam flow rates, and non-condensable gas concentrations. The experimental results indicated a substantial deterioration in condensation when non-condensable gas was presented. Moreover, they showed that with an increase in steam flow rate and system pressure the condensate rate increased, and the boundary layer thickness and non-condensable gas concentration also increased along the condenser tube length. In the companion paper, Henderson et al. [9] studied the capability of tube bundles in heat removal in the complete condensation mode of a passive condenser. The results showed a similar trend for condensation heat transfer compared to the single tubes, except condensate mass flux was slightly higher.

Che et al. [10] used the Colburn-Hougen method to analyze the heat and mass transfer process when the water vapor entrained in a gas stream condenses into water on the tube wall. They introduced a new dimensionless number Ch , which is defined as condensation factor. They also

conducted an experimental study using a single row plain tube heat exchanger with the vapor-air mixture to simulate flue gases. Their results showed that the convection-condensation heat transfer coefficient is 1.5 times higher than that of the forced convection without condensation. In another study, Liang et al. [11] studied forced convection heat transfer with water vapor both theoretically and experimentally. They conducted their experiments using the air-steam mixture to simulate the flue gas of a natural gas fired boiler and for the vapor mass fraction range of 3.2 to 12.8%. Using theoretical analysis, they derived a new dimensionless number defined as augmentation factor which accounts for the effect of condensation of the relatively small amount of water vapor on convection heat transfer. They also proposed a correlation based on the experimental data for the combined convection–condensation heat transfer Nusselt number.

Mosthaf et al. [12] studied two-component non-isothermal flow with two phases inside the porous medium and one phase in the free-flow region numerically. They used Darcy's law for the porous medium and Navier-Stokes equations for the free-flow region as the governing equations. They developed a coupling concept, which was able to deal with miscible flow and a two-phase system inside the porous medium. The proposed model was also able to account for evaporation and condensation processes at the interface. Nabati studied condensation phenomena of water vapor from a mixture of CO₂/H₂O on a vertical plate numerically [13]. Two condensation models were developed, and appropriate numerical approaches were used to implement those models. The results indicated that the proposed condensation models could predict the trends in condensation behavior of binary mixture.

1.5. TMC heat exchangers

A significant portion of waste heat in power plants is of low-grade heat which has low temperature and high water vapor content. The water vapor in the flue gas accompanies different corrosive gas

in many processes. For instance, in a typical coal-fired power plant boiler the relative humidity of flue gas reaches up to 100% and water vapor content of the flue gas may vary from 20-40% in volume. Discharging flue gases with high water vapor content into the atmosphere and losing its latent heat decreases the thermal efficiency of industrial units [14]. On the other hand, recovering 40-60% of this water can significantly increase the power plant's thermal efficiency.

Heat recovery associated with the latent heat of water vapor is significantly higher than the amount of heat which can be recovered from the sensible heat at the operating temperature of the condensing heat exchangers and convective heat transfer.

Transport Membrane Condenser (TMC) [1] is a ceramic nano-porous membrane-based technology which aims to separate the water vapor from the air or flue gas flow stream. This innovative type of membrane can recover both water and latent heat in addition to sensible heat from the low-temperature gas flows which contains high water vapor contents. Flue gas with low temperature and high water vapor content are widely available in many industrial processes such as food industry, cement industry, metal industry, petroleum industry, chemical industry and paper industry. In addition to recovering sensible heat, the TMC technology can recover pure water and latent heat of condensation which are difficult to be retrieved using conventional heat recovery technologies. Performance of conventional heat exchangers is typically poor when the temperature difference of two flow streams is not significant, and the vapor-related corrosion is always a challenging issue.

The walls of a TMC based heat exchanger are made of nanoporous materials. These types of materials have nanoscale pores over their surface and can extract pure condensate water from the flue gas in the presence of other non-condensable gases (i.e., CO₂, O₂, and N₂). These tube walls have three porous layers with different porous sizes. Water vapor from the flue gas is transported through the membrane structure by first condensing inside the inner separation membrane layer

(60Å to 80Å pore size), then moving through the intermediate layer (500Å pore size) and finally through the last layer (0.4 µm pore size) and at the end will join the cooling water stream.

Contaminants in the flue gases, such as CO₂, O₂, NO_x, and SO₂ are inhibited from passing through the membrane by the membrane high selectivity. The condensed water through these tubes is highly pure and can be used as the makeup water for many industrial applications. In power plant applications this condensed water along with its heat which has been recovered during the condensation of water combines with the cold boiler feed water, can help to raise the water temperature before entering the boiler feed water tank. The amount of heat and water which can be recovered by this innovative type of heat exchanger is almost twice of the conventional types of heat exchangers in the power plants.

To clarify the importance of low-grade heat and water recovery and TMC technology it should be mentioned that in the year 2000 the U.S. net electric power generation was 3,802 billion kWh. From this amount, 1,966 billion kWh was the portion related to coal-fired generation, and natural gas-fired generation was another 613 billion kWh [14]. Considering 35% efficiency for the fuel to electricity, the total firing rate can be estimated at 25 trillion Btu/hr. Hence the water saving corresponding to the TMC technology would be 8.3 billion tons per year. This value corresponds to the total annual saving of \$4.3 billion in water cost alone [15]. Moreover, the TMC technology can enhance the thermal efficiency of boiler 0.1-0.2% by recovering the latent heat during the condensation process which corresponds to 3.0 billion kWh power output efficiency in the U.S. Table 2 shows some a summary of possible energy saving and amount of CO₂ emission which can be avoided by using TMC technology.

Table 2. Summary of TMC potential application and possible savings [16].

	Energy Saving (Trillion Btu/year)	Avoided CO ₂ (million tons/year)
Industrial and commercial boilers [17]	1,207	60.4
Coal-fired utility boilers with Flue Gas Desulfurization (FGD)	2,535	126.8
Refining industry with wet scrubbers	18.9	0.945
Portland cement industry with a wet scrubber	2.6	0.13
Iron and steel industry with wet scrubbers	5.7	0.286
Pulp and paper industry with wet scrubbers	38.5	1.924
Residential home furnaces [18]	331	16.6
Total	4,139	207.1

Low-grade water and heat recovery using TMC tubes address DOE Industrial Technologies Program's (ITP's): Energy Intensive Processes (EIP) Portfolio - Waste Heat Minimization and Recovery platform [19]. Simulation, design, and optimization of TMC heat exchangers is a Collaborative research project sponsored by US Department of Energy (DOE), between Gas Technology Institute (GTI) and the Department of Mechanical and Materials Engineering at Florida International University (FIU). This project is aimed to maximize the performance of TMC heat exchanger for industrial applications in the US. Commercialization of TMC based heat exchangers can save a significant amount of energy and money and reduce greenhouse gas emissions during the power generation or other industrial processes. The primary target market of TMC heat exchanger technology is the power generation industries where flue gases containing water vapor is available in high mass and flow rate. To fully understand the advantage and mechanism of heat and water recovery using TMC heat exchangers, it is required to review and understand the condensation mechanism and previous works which have been conducted on condensation and heat recovery using regular tubes and heat exchangers. Moreover, the physics behind the condensation

over a solid surface will be the starting point for modeling and optimization of TMC heat exchangers in this research.

Membrane technology is among the most common methods for liquid and gas separation in industrial scale which benefits from low cost and high separation ratio. Membranes can be categorized as porous and nonporous materials. For the porous membrane, the pore size usually is sub-micron/nano. In the case of gas separation, the pore size of the membrane needs to be less than 50 nm for different applications. Previous investigations have shown that separation of water vapor from flue gas has the highest rate when the capillary condensation occurs which allows passing of condensed phase through the membrane [16].

Kelvin equation predicts that condensation occurs in small pores when the partial pressure of the condensing species is below its vapor pressure i.e., 50-80% of the saturation vapor pressure. For water vapor, this value corresponds to a relative humidity of the mixture [16]. A typical ceramic membrane and its pore size distribution are shown in Figure 6.

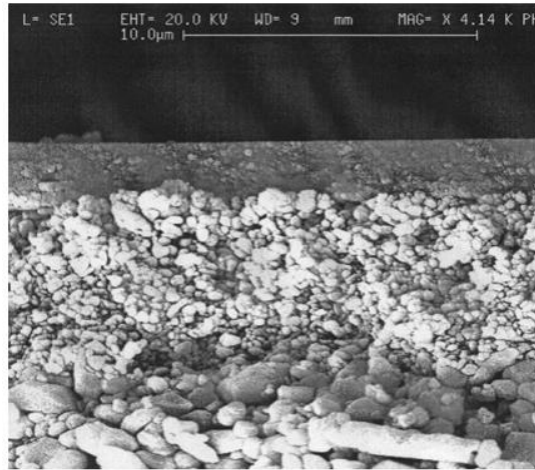


Figure 6. Photomicrograph of TMC membrane cross-section [16].

The membrane in gas separation industries can be categorized as non-porous and porous membranes. In the non-porous membrane, the separation of mixture components is based on

different solubility and diffusivity [20]. The separation ratio is usually high however their transport flux is low [21] and [22]. On the other hand, separation process in porous membrane relies on a combination of molecular sieving, surface effects and diffusivity [6] which themselves depend on pore size and surface characteristic. Separation of water vapor in the porous membrane can be considerably improved when the condensed water completely blocks the nanopores on the outer surface of the TMC tubes and prevents the transport of other non-condensable gases [23],[24]. Due to the complexity of capillary condensation, the literature on this topic is relatively little especially regarding modeling and numerical simulation.

Previous experiments carried out by GTI [16] showed that the nanoporous ceramic membrane with pore size 6 nanometer has low water vapor transport flux when working in Knudsen diffusion transport mode. But when the flue-gas stream is sufficiently cooled by the cooling water inside the porous tubes and the relative humidity of the flue gas increases, capillary condensation becomes the dominant condensation mechanism on the nanoporous layer. Pertinent experimental data on condensation and transport of water vapor in Knudsen and capillary modes indicates that the water vapor flux and separation ratio of nanoporous membrane increase 5 and 100 times respectively when the transport mode changes from Knudsen to capillary mode (see Figure 7).

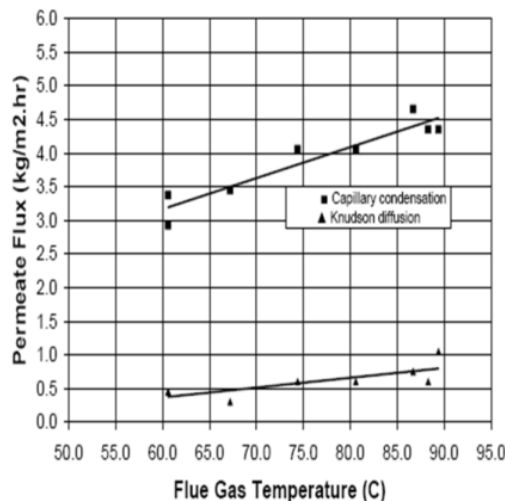


Figure 7. Membrane transport mode effect [16].

Hence the onset of capillary condensation mode is necessary to have a high-performance TMC heat exchanger. The concept of capillary condensation on the nanoporous surface and transport of water from the flue-gas to the cooling water inside the porous tube is shown in Figure 8. As seen in this figure, the water vapor condenses inside the outer separation nano-porous layer (60\AA to 80\AA pore size) (~ 2 to $4\ \mu\text{m}$ thick) then moves to the intermediate layer with a pore size of 500\AA (typically 20 to $50\ \mu\text{m}$ thick). From there the condensed water joins the cooling water mainstream after passing the substrate ($0.4\ \mu\text{m}$ pore size) ($\sim 1\ \text{mm}$ thick). The condensed water in the first layer blocks the other gases in the flue gas. A small vacuum is maintained on the water side of the TMC heat exchangers to prevent backflow of water from inside of the TMC tubes to the outside.

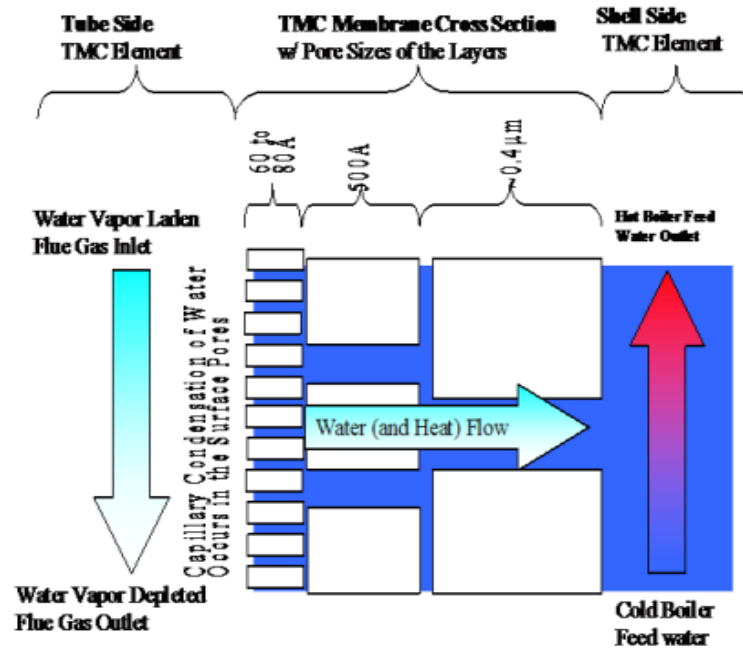


Figure 8. Schematic of water transport concept in TMC tubes [16].

Experimental studies also show that the heat transfer and condensation process significantly increases by using TMC bundle tubes compared to impermeable solid tubes [1] and [25]. Moreover, continues transport of water from the outer surface of the TMC tubes to the cooling water stream inside the TMC tubes helps the convective heat transfer mechanism by diminishing the water film

from the outer surface which works as an insulating layer. The experimental results [25] also indicate that the convective Nusselt number for the TMC tube bundle is 50% to 80% higher than that of solid stainless steel tube bundle. The condensation rate is also enhanced 60% to 80% by using TMC tubes compared to solid tubes.

The TMC tubes which have been used by GTI (Gas Technology Institute) [26] are made of corrosion-resist nanoporous ceramic materials with superior conductivity which work based on capillary condensation mechanism. Figure 9 shows the schematic of a TMC membrane and the TMC wall micrograph.

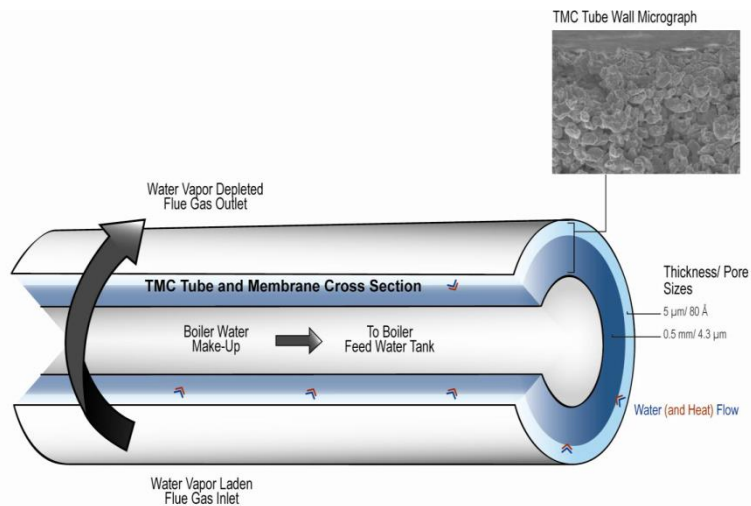


Figure 9. TMC concept (main component α alumina) [16].

GTI has also conducted an experimental test to evaluate the performance of a two-stage TMC water and heat recovery unit for the potential host power plant coal-fired flue gas condition [16]. For this unit, two separated cooling water stream has been used to enhance the overall performance of the TMC unit. In the first stage, the cooling water was provided from the condenser in the power generation process, and the outlet water from the first stage feeds in the deaerator for boiler water makeup. In the second stage, the inlet comes from the condenser, and the outlet of this stage was routed to the cooling water stream. A pilot-scale has been designed and fabricated at GTI for TMC,

3 million Btu/hr natural gas-fired the boiler. Based on the obtained data a pilot scale TMC system could recover a tremendous amount of heat and pure water from the flue gas. Experimental study on the performance of TMC unit for a typical 550 MW power plant has been conducted as well.

Beside the alumina-based ceramic membrane, GTI also developed metallic based (stainless steel) substrate to be used in TMC heat exchangers (see Figure 10). One of the most significant advantages of the metallic membrane over the ceramic membrane is the higher thermal conductivity of metallic substrates which results in superior performance of these porous tubes. Moreover, a metallic based substrate is more robust and easy to fabricate for large industrial applications.



(a)



(b)

Figure 10. Photo of (a) stainless steel-based substrates and (b) ceramic based substrates.

Optimization of TMC tube arrangement and pore size can facilitate the heat and water recovery process in both first and second stages of a two-stage TMC heat exchanger system and reduce the

unfavorable fouling effect in the system. The two staged TMC system has been optimized by GTI and its partners based on the coal-fired power plant data provided by SmartBurn LLC [27]. The optimization for the two-stage TMC system is carried out in the way that the first stage recovers maximum heat and enough water for the boiler makeup and the second stage recover the maximum amount of water. Membrane pore size was 8 to 25 nanometer for different TMC tubes. In a power plant power generation loop, there are two cooling water streams: the turbine stream condensate and the condenser cooling water. The temperature of the cooling water in the turbine steam condensate is lower and typically is about 25 times of the boiler feed water stream. Experiments showed that using a two-stage TMC system up 90% of the water vapor from the flue gas of a coal-fired power plant can be extracted [16]. Schematic flow diagram for a two-stage TMC system is shown in Figure 11.

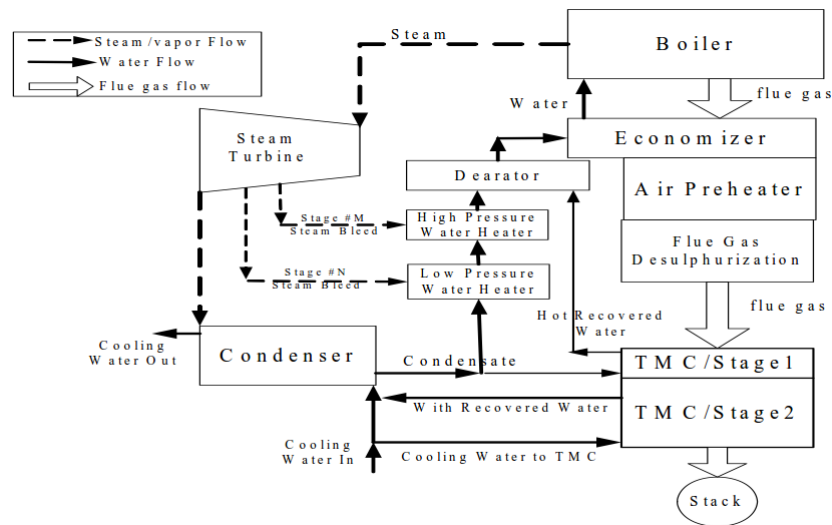


Figure 11. Schematic of low-grade heat and water recovery in a 2-stage TMC system [16].

The inlet cooling water for the first stage was obtained from the steam condensate of the condenser and the outlet water containing the recovered water vapor from the flue gas goes to the deaerator as the makeup water for the boiler. The outlet temperature of the cooling water in the first stage is between 130°F to 160°F which increases the overall efficiency of the boiler by about 0.5%. The

amount of recovered water was about 1% of the main water stream which is more than the required makeup water for the boiler. The second stage TMC was placed between the FGD unit and the stack, the inlet water was a part of cooling water of the condenser, and the outlet water from this stage was routed back to cooling water stream.

Recently, the performance of a single tube membrane regarding heat and water recovery has been studied experimentally by Wang et al. [28] and Chen et al. [29] for different water and vapor-air mixture conditions. In another study, Wang et al. [30] investigated the amount of heat and water recovery in a multichannel tubular ceramic membrane. They compared the performance of the multichannel membrane with that of a mono-channel tube and concluded that the multichannel membrane has lower mass and heat transfer rates. Effect of membrane wettability on the condensation rate and heat recovery of a TMC tube has been studied by Hu et. al. [31]. Their experimental results indicate that the hydrophilic surface has higher performances regarding heat transfer and condensate recovery.

1.6. Limitation of the existing research and present contribution

The current waste heat recovery technologies are suffering from different practical issues. Most of these technologies require high-grade waste heat. Moreover, the cost of recovered heat and complexity of the waste heat recovery procedures are among the most critical challenges. The existence of the condensable gases in the flow stream, although increase the heat transfer rate due to the latent condensation heat, would also create a significant issue of corrosion as the condensed water exposes to the other non-condensable gases at a lower temperature. The TMC technology is a low-cost technology which has been developed to address the shortcomings of the currently available waste heat recovery methods. Prediction of the performance of TMC heat exchangers is one of the most critical issues which slows down the development and commercialization of this

technology in various industrial applications. A literature review on the modeling of TMC revealed that the current modeling of the ceramic membrane is limited to the 1D cases and based on analytical equations. This means that many design aspects for the ceramic membrane including the geometrical and design conditions cannot be considered or predicted. Here a numerical model and simulation procedure was developed for performance evaluation of TMC. The model considers both capillary and solid wall condensation on the surface of the TMC tubes as well as the species and heat transport procedures inside the TMC tubes. Contrary to the previous researches and available models, the proposed model can accurately predict the condensation and heat transfer rates in a TMC heat exchanger by fully modeling of the physical domain. By using both diffusion-based condensation (condensation mechanism on a solid wall) and capillary condensation (condensation mechanism inside nanopores), this model can predict the performance of TMC heat exchangers for a wide range of working conditions.

1.7. Proposed research approach

The stages of this study are broken into three primary sections. In the first stage, a simplified model base on the experimental data and by implementing a correction factor was used. The available experimental data are provided by Gas Technology Institute and conducted using the test rigs for lab scale TMC heat exchangers. These data are used to calculate the correction factor in the simplified model and initial evaluation of the performance of TMC heat exchangers to meet the requirements of the DOE project. The simplified model is based on the Fick's model of diffusion but does not consider some parameters and effect of a nanoporous layer on the condensation and transport process of water vapor. In the second stage of the project, a model was developed to predict the condensation and transfer rate of water vapor by considering nanoscale vapor transfer mode inside nanoporous materials, the capillary condensation. During the modeling stage and

validation, the further experimental investigation will be conducted if necessary. In the third stage, optimization of tube pitches for TMC heat exchangers will be carried out with the objective functions to be maximizing the heat transfer.

1.8. Outline of the Dissertation

The remaining chapters of this dissertation are organized as follow:

- In chapter 2 the fundamental of the condensation process over a solid wall are presented. Also, thermodynamic relations, governing equations, properties of materials and other pertinent considerations are covered in chapter 2. At the end of chapter 2 validation of the prepared model for various cases are carried out to verify the accuracy of the numerical model.
- Chapter 3 is aimed to present a simplified model for a model for heat and mass transfer inside TMC heat exchangers based on the solid wall condensation model. The condensation model for the solid wall is modified using a correction factor based on the experimental data.
- In chapter 4, a numerical model is proposed for the simulation of condensation over a TMC tube. The proposed model has been implemented in the numerical solver and verified against the available experimental data.
- In chapter 5, using the proposed model in the previous chapters, parametric study and optimization of the tube pitches in cross-flow TMC heat exchangers have been conducted.
- In chapter 6, the performance of shell and tubes TMC heat exchangers are evaluated. High pressure and temperature application for the transport membrane and water and heat

recovery for different working conditions and various arrangements of the TMC heat exchanger in a TMC unit have been studied and reported.

- Chapter 7 presents the summary of the dissertation and the conclusion.

2. Chapter 2: Thermodynamic Properties and Governing Equations

Naturally, condensation occurs when the vapor/steam temperature reaches the saturation temperature (T_{sat}) at the operating condition pressure. In most of the applications, condensation near a cold wall with a surface temperature of (T_s) is the essential type of condensation compared to bulk condensation or condensation at the interface of a gas and a liquid [13]. Film/Wall condensation has been accepted to be the most common condensation mechanism in the heat exchangers [32], [33].

During the condensation process, the condensed vapor forms a liquid film on the solid surface which drips down under the effect of gravity force. This liquid film suppresses both heat transfer and condensation rate on the solid surface. Previous experimental studied relived that the non-condensable gases in a mixture have an adverse effect on the condensation process [34], [35]. During the condensation process, the non-condensable gases move toward the cold wall along with the vapor and accumulate there and block the vapor path to the surface. Moreover, this accumulation of non-condensable gases near the solid increases the partial pressure of the non-condensable gases near the wall compared to that of in the mixture and produce a driving force for the non-condensable gas toward the bulk flow. This diffusion of the non-condensable gases is the water vapor movement and suppresses the condensation rate.

Wall condensation models can be divided into three major categories:

- 1- Condensation models based on experimental correlations, which are obtained by fitting experimental results on heat transfer coefficients as a function of non-condensable gas concentration, some of these well-known corrections are achieved by Tagami [36] and Uchida et al. [37].
- 2- Models based on the heat and mass transfer analogy (HMTA) in the boundary layer (Chilton–Colburn–Cougen analogy, [38]) which are semi-empirical.

3- Mechanistic models (diffusion based model) which do not require any closure [39].

The advantage of the experimental based models is their simplicity hence they can be used in different numerical modeling or to verify other numerical models for specific cases. The disadvantage of these models is they are limited to specific geometry or operating conditions and cannot be generalized. The models based on the heat and mass transfer analogy are usually more realistic and still simple enough to be used be implemented in different numerical models. The mechanistic models are generally the best between the three condensation models and can be used for different geometries and operating conditions, but the implementation of them are much more complicated than the two previous models.

Nabati [13] studied condensation of water vapor in a $\text{CO}_2/\text{H}_2\text{O}$ mixture on a vertical flat plate numerically. The results of numerical simulation indicated that the condensation rate decreases as the mass fraction of non-condensable gas in the mixture increased.

Chen and Lin [40] studied the two-dimensional turbulent film condensation on a horizontal tube in the presence of non-condensable gases numerically. They used a finite volume method in curvilinear coordinate to solve the governing equations for both mixture phase and liquid film phase. They also considered the effect of inertia and pressure gradient on the condensation by using a two-phase model. Their results confirmed that even a small concentration of non-condensable gases in the mixture reduces the heat transfer coefficient and film thickness considerably. Moreover, as the inlet velocity increased, the heat transfer coefficient on the tube enhanced while the thickness of liquid film decreases.

Dehbi et al. [39] studied wall condensation of steam is the presence of non-condensable gases using ANSYS CFD code FLUENT. They applied the condensation model and the appropriate source/sink terms using appropriate User Defined Functions (UDF). Effect of liquid film thermal resistance has been ignored which implies that the applied model was valid for mixture with a significant mass

fraction of non-condensable gases (more than 0.1). After introducing a correction factor based on the Bird's suction parameter for high condensation rate case they validated their model against different experimental cases for both laminar and turbulent flows.

Kljenak et al. [41] numerically studied contaminant atmosphere mixing and stratification using CFD code CFX 4.4. Using a single-phase model, they simulated steam condensation on vessel walls after applying the mass and energy sinks. Condensation rate has been calculated based on the correlation proposed by Uchida [42]. Comparison of the CFD prediction and previous experimental results showed a good agreement.

Malet et al. [43] investigated wall condensation due to natural convection for TOSQAN test facility using TONUS-CFD code [39]. TOSQAN project has been created to study the thermal-hydraulic flow condition in the presence of non-condensable gases which is the case during severe pressurized water reactor accidents. They conducted the numerical and compared their results for eight test cases. They also mentioned that the limitation of the numerical modeling was mainly due to the turbulent model and in the boundary layer region.

De la Rosa et al. [44] studied the effect of a suction factor on the mass transfer in both laminar and turbulent flow. They concluded that using the Bird's suction factor; which has been used commonly in laminar flow; for turbulent flows overpredicts the mass transfer in turbulent flow. They also proposed an alternative suction factor for turbulent flow and compared their results with the results obtained by Bird's original formulation in a condensation over a flat plate case. They demonstrated that their new formulation is more suitable for turbulent natural convection while the Bird's formulation works better for laminar flow scenario.

Bucci et al. [45] simulated wall condensation on a flat plate using the different turbulent model to study the transpiration effects on condensation rate using classical suction and blowing multiplier. They compared the obtained numerical results with classical correlations of Nusselt and Sherwood

numbers. By comparison between the results of different turbulent models, they concluded that the conventional correction factors overestimate suction in case of condensation while in case of evaporation all of the turbulent models performed relatively accurate when their results were compared with the classical theory.

Karkoszka and Anglart [46], studied the free convection condensation problem for binary and ternary mixture of condensable and non-condensable gases both analytically and numerically. They demonstrated in case of a binary mixture the results of both methods are equivalent while for a ternary mixture the latter method must be used in conjunction with the mechanistic CFD-based model.

Houkema et al. [47] used the commercial code CFX4 [48] to simulate the condensation phenomenon in the presence of non-condensable gases and compared their results with previously published experimental data. They also investigated the deviation of the numerical prediction from the experimental results and proposed a different suggestion for improvement of their numerical model. The most essential recommendations were improving the automatic wall treatment by application of adaptive mesh refinement near the boundary and determining appropriate sub-models for turbulence damping due to stratification for standard two-equation turbulence models.

Asbik et al. [49] studied vapor condensation on a horizontal tube for pure saturated water vapor numerically using a finite difference method. They also considered the effects of flooding and showed that the separation of vapor boundary layer depends on the Froude number.

Sparrow et al. [50] analytically studied the effect of non-condensable gas on condensation for a forced convection boundary layer problem in a laminar regime.

Zschaeck et al. [51] studied wall condensation in the presence of non-condensable gases when conjugate heat transfer for the solid wall exist numerically using ANSYS CFX. They validated their results against the previous experimental works and verified their numerical algorithm.

Ambrosini et al. [52] investigated the evaporative film cooling problem in rectangular channel numerically. They also compared their results with the available experimental data. Their main propose was to evaluate and compare the evaporative film cooling with pure convection regarding cooling capability. The authors have used Fluent 5.4 code [48] and pertinent User Defined Functions for a two-dimensional channel flow case. The turbulent heat and mass transfer have been simulated by the RNG $k-\varepsilon$ model.

Dehbi [53] studied the accuracy of two common wall condensation simulation approaches; whether the boundary layer is fully resolved, or in case the wall function is used. The results showed that in the developing region of the boundary layer the predicted results using the wall function deviates from the experimental ones, while by developing the boundary layer in the downstream of the flow this prediction becomes more accurate. Moreover, the author suggested that for more complex three-dimensional geometries in which the flow is three-dimensional, boundary layer detachment is expected.

Moukalled et al. [54] carried out numerical simulation and optimization of a rooftop AC unit using a two-phase model. They also used a correction factor in the condensation rate to adjust the numerical simulation with the experimental results.

Benelmir et al. [55] conducted a numerical simulation of condensation water vapor condensation in a fin-and-tube heat exchanger. Their numerical results demonstrated the effect of recirculation behind the tubes on the maximization of air concentration in this region and the heat transfer coefficient decreases when moving from the first to the last row of tubes.

Lee et al. [56] improved the capability of UPID code, which is a transient two-phase flows for simulation of nuclear reactor components, by applying wall condensation in the presence of non-condensable gases and liquid film model. They used the wall function approach and heat and mass transfer analogy to avoid the solution of the boundary layer and to refine the mesh near the boundary to increase the computational efficiency of the code.

Lehmkuhl et al. [57] focused on the simulation of wall condensation for contaminant scale problem using single-phase method along with wall function to have proposed an accurate and low computational cost approach. As it has been mentioned by the authors, the standard wall functions are developed to simulate fluid flow and the major simplifications in the wall function are not suitable for condensation problems. The authors also developed two wall functions to address the limitation of conventional wall functions in the prediction of wall condensation and the pertinent heat transfer.

Vyskocil et al. [58] developed a condensation model for both compressible and incompressible flow considering wall and volume condensation simultaneously. They validated the proposed model by comparing their results with previous experimental cases for the binary air-steam mixture.

Sun et al. [59] studied natural convection with condensation/evaporation in a two-dimensional square cavity. The simulation has been conducted using an unsteady weakly compressible solver. The numerical simulation has been performed for atmospheric pressure and temperature range 300 K to 350 K.

1.9. Numerical simulation of condensation phenomena on a solid wall

In this section, the governing equation, condensation models and relation for the thermodynamic properties of different gases will be described in detail. Moreover, solution procedure and

validation of the condensation setup will be examined by comparison of the numerical setup with the previous experimental results. This setup will be used as the based setup to modify and apply the condensation phenomena over the TMC tubes later. All the equations and properties of species in this section belongs to air-water vapor binary mixture.

1.10. Thermodynamic properties of mixtures and species

Regarding water vapor, air and mixture properties different authors made various assumptions for their numerical simulation. Following are some of the assumptions which have been made to calculate the thermodynamic properties of species and mixture.

Dehbi [53] considered the water vapor and non-condensable mixture to behave as an ideal gas and diffusion coefficient, viscosity, thermal conductivity, etc. were calculated based on the kinetic theory and mixture rules. The effect of gravity has been considered as well in the modeling. As the boundary condition, a fully developed turbulent flow is assumed, and 1/7th power profiles are applying for on the inlet boundary for the velocity. The turbulent inlet intensity and the ratio of laminar to turbulent viscosity are assumed to be 5% and 5.

Zschaeck et al. [51] considered that the fluid was an ideal multi-component mixture of air and water vapor in their simulations and considered the air to be their constraint species. For the air, the perfect gas properties are used. The IAPWS-IF97 equation of state was considered to be valid for the water vapor while the density of the cooling water was taken to be constant. The molecular diffusivity of water vapor in the air was taken from Poling et al [60].

Benelmir et al. [55] also considered the mixture of air/vapor as an ideal incompressible Newtonian flow. They also neglected the effects of radiation and viscous dissipation. They used the following

physical properties for the air: $D_v = 2.065 \times 10^{-5} \text{ m}^2 \text{ s}^{-1}$; $k = 0.0242 \text{ W m}^{-1} \text{ K}^{-1}$; $c_p = 1,013.484 \text{ J kg}^{-1} \text{ K}^{-1}$; $\rho = 1.219 \text{ kg m}^{-3}$; $\mu = 1.785 \times 10^{-5} \text{ kg m}^{-1} \text{ s}^{-1}$ and $Pr = 0.747$.

Sun et al. [59] used the equations given by Lide and Kehiaian [61] for thermodynamic properties of air and water vapor which are applicable for the range of [273 K, 600 K]:

- Dynamic viscosity:

$$\mu = A_1 T + A_2 T^2 + A_3 T^3 + A_4 T^4 \quad (\text{kg m}^{-1} \text{ s}^{-1}) \quad (3)$$

where the coefficients of the polynomial expansion are defined in Table 3.

Table 3. The coefficient of the polynomial expansion for dynamic viscosity.

	μ at 298.15 K	A_1	A_2	A_3	A_4
Dry air	18.5×10^{-6}	7.72488×10^{-8}	-5.95238×10^{-11}	2.71368×10^{-14}	–
Water vapor	9.9×10^{-6}	5.75100×10^{-8}	-1.73637×10^{-10}	3.90133×10^{-13}	-2.69021×10^{-16}

- Thermal conductivity:

$$k = A_1 T + A_2 T^2 + A_3 T^3 + A_4 T^4 \quad (\text{W m}^{-1} \text{ K}^{-1}) \quad (4)$$

where the coefficients in the thermal conductivity equation are defined in Table 4.

Table 4. The coefficient of the polynomial expansion for thermal conductivity.

	k at 298.15 K	A_1	A_2	A_3	A_4
Dry air	26.1×10^{-3}	0.965×10^{-4}	-9.96×10^{-9}	-9.31×10^{-11}	8.882×10^{-14}
Water vapor	18.6×10^{-3}	0.349×10^{-4}	1.511×10^{-7}	-2.576×10^{-10}	2.050×10^{-13}

- Heat capacity:

$$C_{p,air} = 1000 + 2.5 \times 10^{-7} T^3 \quad (\text{J K}^{-1} \text{ kg}^{-1}) \quad (5)$$

$$C_{p,vapor} = A_0 + A_1T + A_2T^2 + A_3T^3 \quad (\text{J K}^{-1} \text{ kg}^{-1}) \quad (6)$$

where the coefficients in the heat capacity equations are defined in Table 5.

Table 5. Coefficients of the polynomial expansion for vapor heat capacity.

	$C_{p,vapor}$ at 298.15 K	A_0	A_1	A_2	A_3
Water vapor	1866.1	1877.8	-0.4417	1.568×10^{-3}	-7.286×10^{-7}

- Latent heat of condensation

$$h_v = 2.7554 \times 10^6 - 3.46T_w^2 \quad (\text{J kg}^{-1}) \quad (7)$$

- The saturated vapor pressure is calculated:

$$P_{H_2O,sat} = 10^5 \exp\left(18.79 - 0.0075T - \frac{5965.6}{T}\right) \quad (\text{Pa}) \quad (8)$$

where T is in Kelvin.

- Dewpoint temperature corresponding to the partial pressure P_{H_2O} of the water vapor:

$$T_d = 66.67 \left(B - \sqrt{B^2 - 178.968} \right) \quad (\text{K}) \quad (9)$$

where $B = 18.79 - \ln(10^{-5} P_{H_2O})$ and P_{H_2O} is in Pa.

For the air-vapor mixture, the relative humidity can be calculated:

$$RH = \frac{P_{H_2O}}{P_{H_2O,sat}} = \frac{\chi_v \bar{P}}{P_{H_2O,sat}} \quad (\%) \quad (10)$$

where χ_v is the mole fraction of water vapor which can be obtained from the mass fraction of air and vapor in the mixture at each location:

$$\chi_v = \frac{W_v}{W_v + M^* (1 - W_v)} \quad (11)$$

The equations are given by Rao et al. [62] were used to evaluate the gas mixture properties:

- Dynamic viscosity

$$\mu = \frac{(\sqrt{18}\mu_v\chi_v + \sqrt{29}\mu_a\chi_a)}{(\sqrt{18}\chi_v + \sqrt{29}\chi_a)} \quad (\text{N s m}^{-2}) \quad (12)$$

- Thermal conductivity:

$$k = \frac{\chi_v k_v}{\chi_v + \chi_a A} + \frac{\chi_a k_a}{\chi_a + \chi_v A} \quad (\text{W m}^{-1} \text{K}^{-1}) \quad (13)$$

where

$$A = \frac{1}{3.6} [0.8876(1 + \sqrt{K_v/K_a})]^2 \quad (\text{W m}^{-1} \text{K}^{-1}) \quad (14)$$

- The heat capacity of the mixture is calculated as:

$$C_p = (1 - W_v)C_{p,a} + W_v C_{p,v} \quad (\text{J K}^{-1} \text{kg}^{-1}) \quad (15)$$

- The diffusion coefficient of water vapor in the air was calculated based on the local temperature and pressure of the mixture in atmospheres (\bar{P}) and T in Kelvin:

$$D_{av} = \frac{1.87 \times 10^{-10} \times T^{2.072}}{\bar{P}} \quad (\text{m}^2 \text{s}^{-1}) \quad (16)$$

Sarairoh [63] used the following thermophysical properties for simulation of condensation using a mechanistic model. The following thermodynamic relations have been used for the water liquid, air and water vapor in the numerical simulations:

The diffusion coefficient of water vapor in the air was calculated by:

$$D = (2.775 \times 10^{-6} + 4.479 \times 10^{-8} T + 1.656 \times 10^{-10} T^2) P / 100 \quad (\text{m}^2 \text{s}^{-1}) \quad (17)$$

The mass fraction of water vapor was calculated by:

$$Y_v = \frac{\omega}{1 + \omega} \quad (18)$$

where ω is the specific humidity of the air-vapor mixture:

$$\omega = \frac{0.622P_v}{P - P_v} \quad (19)$$

where P_v is the saturation vapor pressure of water as a function of temperature and can be determined by:

$$P_v = 1000 \times \exp\left(-0.4702 + 0.06991T - 2.249 \times 10^{-4}T^2 + 3.563 \times 10^{-7}T^3\right) \quad (20)$$

The latent heat (h_{fg}) of condensation can be expressed as:

$$h_{fg} = 1000 \times \left(3601 - 6.865T + 0.01491T^2 - 1.652 \times 10^{-5}T^3\right) \quad (21)$$

$$h_{fg} = 2,775,400 - 3.464(T - 5)^2 \quad (22)$$

Water Liquid properties

The following properties of liquid water properties are valid from 0°C to 288°C [64]:

Thermal Conductivity:

$$k = 0.56611 + 0.002048T - 1.0205 \times 10^{-5}T^2 + 1.1897 \times 10^{-8}T^3 \quad (23)$$

Specific Heat:

$$c_p = \exp\left(1.4423 - 8.4025 \times 10^{-4}T + 1.41 \times 10^{-5}T^2 - 7.3846 \times 10^{-8}T^3 + 1.4856 \times 10^{-10}T^4\right) \quad (24)$$

Density:

$$\rho = 1002.6 - 0.2177T - 0.0020099T^2 - 1.6478 \times 10^{-6}T^3 \quad (25)$$

Dynamic viscosity:

$$\mu = \exp\left(-6.3933 - 0.026299T + 9.7341 \times 10^{-4}T^2 - 1.3986 \times 10^{-7}T^3\right) \quad (26)$$

Dry Air

The following properties are valid from 0°C to 400°C [64]:

Thermal conductivity:

$$k = 0.02428 + 6.939 \times 10^{-5}T + 2.515 \times 10^{-8}T^2 - 7.194 \times 10^{-11}T^3 \quad (27)$$

Specific heat:

$$c_p = 1.005 - 1.473 \times 10^{-5}T + 7.002 \times 10^{-7}T^2 - 6.846 \times 10^{-10}T^3 \quad (28)$$

Density:

$$\rho = \frac{101.325}{0.287(T + 273.15)} \quad (29)$$

Dynamic viscosity:

$$\mu = \left(13.29 + 0.0879T + 0.0001029T^2 - 3.749 \times 10^{-8}T^3\right) \times 10^{-6} \quad (30)$$

Water Vapor

The following properties are valid for the range of 0 to 200 °C [64]:

$$k = 0.017071 + 5.3167 \times 10^{-5}T + 2.322 \times 10^{-7}T^2 + 3.8962 \times 10^{-10}T^3 \quad (31)$$

Specific heat:

$$c_p = 1.8653 + 1.0881 \times 10^{-5} T - 4.4902 \times 10^{-6} T^2 + 1.0183 \times 10^{-7} T^3 \quad (32)$$

Dynamic viscosity:

$$\mu = 10^{-6} \times (9.1445 + 0.029257 T + 1.9067 \times 10^{-6} T^2) \quad (33)$$

1.11. Thermophysical properties of the multi-component mixture

During the numerical simulation different properties of the mixture needs to be calculated in the solution domain. Ansys Fluent [48] provides various option to enter the properties of materials such as polynomial, piecewise-linear, piecewise-polynomial:

- Polynomial:

$$\phi(T) = A_1 + A_2 T + A_3 T^2 + A_4 T^3 \quad (34)$$

- Piecewise-linear:

$$\phi(T) = \phi_n + \frac{\phi_{n+1} - \phi_n}{T_{n+1} - T_n} (T - T_n) \quad (35)$$

- Piecewise-polynomial:

$$T_{\min,1} < T < T_{\max,1} \quad \phi(T) = A_1 + A_2 T + A_3 T^2 + A_4 T^3 \quad (36)$$

$$T_{\min,2} < T < T_{\max,2} \quad \phi(T) = B_1 + B_2 T + B_3 T^2 + B_4 T^3$$

As it was mentioned by Dehbi et al. [39], using the ideal gas relations limits the application of condensation models to low-pressure cases (less than 10 bar) hence in the mixture the following relations are used to calculate the properties of mixtures:

Density: The density of the multicomponent mixture is calculated the volume-weighted-mixing-law method which is applicable for non-ideal-gas mixtures:

$$\rho = \frac{1}{\sum_i \frac{Y_i}{\rho_i}} \quad (37)$$

where Y_i is the mass fraction and ρ_i is the density of species i .

Viscosity: composition-dependent viscosity of multicomponent mixtures is calculated using mass-weighted-mixing-law [48]:

$$\mu = \sum_i Y_i \mu_i \quad (38)$$

Thermal Conductivity: the mass-weighted-mixing-law is also used to calculate the composition-dependent conductivity of mixtures [48]:

$$k = \sum_i Y_i k_i \quad (39)$$

Specific Heat Capacity: mixing-law [48] is used to calculate specific heat capacity of mixtures:

$$c_p = \sum_i Y_i c_{p,i} \quad (40)$$

Mass Diffusion Coefficients: the diffusion flux for laminar species transport equations using mass and thermal diffusion coefficients reads (Fick's law [39]):

$$J_i = -\rho D_{i,m} \nabla Y_i - D_{T,i} \frac{\nabla T}{T} \quad (41)$$

where $D_{i,m}$ is the mass diffusion coefficient for species i in the mixture and $D_{T,i}$ is the thermal (Soret) diffusion coefficient. In turbulent flows, Equation (41) is replaced with the following form [48]:

$$J_i = -\left(\rho D_{i,m} + \frac{\mu_t}{Sc_t} \right) \nabla Y_i - D_{T,i} \frac{\nabla T}{T} \quad (42)$$

where Sc_t is the effective Schmidt number for the turbulent flow:

$$Sc_t = \frac{\mu_t}{\rho D_t} \quad (43)$$

and D_i is the effective mass diffusion coefficient due to turbulence. It should be noted that the Fick's diffusion law is strictly valid for the dilute mixture ($Y_i \ll 1$ for all i except the carrier gas). Fluent can calculate $D_{i,m}$ by specifying D_{ij} , the binary mass diffusion coefficient of component i in component j using the following relation:

$$D_{i,m} = \frac{1 - X_i}{\sum_{j, j \neq i} (X_j / D_{ij})} \quad (44)$$

where X_i is the mole fraction of species i . In case of turbulent flow, the default constant value is usually acceptable because the turbulent diffusion coefficient overwhelms typically the laminar diffusion coefficient. For cases in which the accuracy of laminar diffusion is also essential the kinetic theory can be used by activating this option for the mixture and defining the Lennard-Jones parameters, and, for each species. The solver will use a modification of the Chapman-Enskog formula [65] to compute the diffusion coefficient:

$$D_{ij} = 0.00188 \frac{\left[T^3 \left(\frac{1}{M_{w,i}} + \frac{1}{M_{w,j}} \right) \right]^{1/2}}{P_{abs} \sigma_{ij}^2 \Omega_D} \quad (45)$$

where P_{abs} is the absolute pressure, Ω_D is the diffusion-collision integral and is a function of T_D^* which is defined as

$$T_D^* = \frac{T}{(\varepsilon/k_B)_{ij}} \quad (46)$$

and k_B is the Boltzmann constant. $(\varepsilon/k_B)_{ij}$ for a mixture is defined as:

$$(\varepsilon/k_B)_{ij} = \sqrt{(\varepsilon/k_B)_i (\varepsilon/k_B)_j} \quad (47)$$

For a binary mixture, σ_{ij} is calculated as:

$$\sigma_{ij} = \frac{1}{2}(\sigma_i + \sigma_j) \quad (48)$$

The thermal diffusion coefficients can be defined as constants, polynomial functions, user-defined functions, or using the following empirically based composition-dependent expression derived from [66] by choosing the kinetic theory option in ANSYS Fluent:

$$D_{T,i} = 2.59 \times 10^{-7} T^{0.659} \left[\frac{M_{w,i}^{0.511} X_i}{\sum_{i=1}^N M_{w,i}^{0.511} X_i} - Y_i \right] \cdot \left[\frac{\sum_{i=1}^N M_{w,i}^{0.511} X_i}{\sum_{i=1}^N M_{w,i}^{0.489} X_i} \right] \quad (49)$$

Fluent also provide the National Institute of Standards and Technology (NIST) database for special requirements such as simulation of species transport in high-pressure condition but using this database is accompanied with various limitation in simulation setup.

1.12. Governing equations

The primary governing equations include mass, momentum, turbulent, and energy conservation equations for fluid flow [67]:

Continuity:

$$\frac{\partial \rho}{\partial t} + \nabla \cdot (\rho \vec{\mathbf{u}}) = 0 \quad (50)$$

Momentum:

$$\frac{\partial}{\partial t} (\rho \vec{\mathbf{u}}) + \nabla \cdot (\rho \vec{\mathbf{u}} \vec{\mathbf{u}}) = -\nabla p + \nabla \cdot (\vec{\tau}) + \rho \vec{g} + \vec{F} \quad (51)$$

where

$$\vec{\tau} = \mu \left[\left(\nabla \vec{\mathbf{u}} + \nabla \vec{\mathbf{u}}^T \right) - \frac{2}{3} \vec{\mathbf{u}} \vec{\mathbf{u}} \right] \quad (52)$$

Energy:

$$\frac{\partial}{\partial t}(\rho E) + \nabla \cdot (\bar{\mathbf{u}}(\rho E + p)) = \nabla \cdot \left(\lambda_{eff} \nabla T - \sum_j h_j \bar{\mathbf{J}}_j + (\bar{\boldsymbol{\tau}}_{eff} \cdot \bar{\mathbf{u}}) \right) + S_h \quad (53)$$

where $\bar{\rho \mathbf{g}}$ and \bar{F} are the gravitational body forces and external body forces, respectively. λ_{eff} is the effective thermal conductivity ($\lambda + \lambda_t$, where λ_t is the turbulent thermal conductivity). In turbulent flow the dynamic viscosity could be replaced with $\mu_{eff} = \mu + \mu_t$ where μ_t is the turbulent viscosity. Both λ_t and μ_t are defined according to the turbulence model. $\bar{\boldsymbol{\tau}}_{eff}$ is the effective stress tensor. $\bar{\mathbf{J}}_j$ is the diffusion flux of species j . E is the total energy including enthalpy h , flow work $-p/\rho$, and kinetic energy $|\mathbf{u}|^2/2$ and S_h is a source term.

The multi-species transport which occurs in the flue gas mixture is governed by the following equation [67]:

$$\frac{\partial}{\partial t}(\rho Y_i) + \nabla \cdot (\rho \bar{\mathbf{u}} Y_i) = -\nabla \cdot \bar{\mathbf{J}}_i + R_i + S_i \quad (12)$$

where Y_i is the mass fraction of the species being calculated, S_i is the rate of creation source term and R_i is the net rate of production by chemical reaction of the species being calculated.

1.13. Turbulence modeling

The standard $k - \omega - SST$ [68] and $RNG k - \varepsilon$ RANS [69] models have been used for validation and simulation of heat and mass transfer in the turbulent regime and implementation of the condensation model.

1.14. Standard $k - \varepsilon$ and $RNG - k - \varepsilon$ Models

The standard $k - \varepsilon$ model [70] is only valid for fully turbulent flows. The turbulence kinetic energy, k , and rate of dissipation, ε , are obtained from solving the following transport equations:

$$\frac{\partial}{\partial t}(\rho k) + \frac{\partial}{\partial x_i}(\rho k u_i) = \frac{\partial}{\partial x_j} \left[\left(\mu + \frac{\mu_t}{\sigma_k} \right) \frac{\partial k}{\partial x_j} \right] + G_k + G_b - \rho \varepsilon - Y_M \quad (54)$$

$$\frac{\partial}{\partial t}(\rho \varepsilon) + \frac{\partial}{\partial x_i}(\rho \varepsilon u_i) = \frac{\partial}{\partial x_j} \left[\left(\mu + \frac{\mu_t}{\sigma_\varepsilon} \right) \frac{\partial \varepsilon}{\partial x_j} \right] + C_{1\varepsilon} \frac{\varepsilon}{k} (G_k + C_{3\varepsilon} G_b) - C_{2\varepsilon \rho} \frac{\varepsilon^2}{k} \quad (55)$$

where, G_k is the generation of turbulence kinetic energy due to the mean velocity gradients, calculated as

$$G_k = -\overline{\rho u'_i u'_j} \frac{\partial u_j}{\partial x_i} \quad (56)$$

and G_b is the generation of turbulence kinetic energy due to buoyancy:

$$G_b = \beta g_i \frac{\mu_t}{Pr_t} \frac{\partial T}{\partial x_i} \quad (57)$$

In Eq. (57), Pr_t is the turbulent Prandtl number for energy and g_i is the component of the gravitational vector in the i th direction. For the standard $k - \varepsilon$ models, the default value of Pr_t is 0.85. In the case of the RNG $k - \varepsilon$ model, where α is given by solving the following equation [70]:

$$\left| \frac{\alpha - 1.3929}{\alpha_0 - 1.3929} \right|^{0.6321} \left| \frac{\alpha + 2.3929}{\alpha_0 + 1.3929} \right|^{0.3679} = \frac{\mu_{mol}}{\mu_{eff}} \quad (58)$$

where $\alpha_0 = 1$. In the high Reynolds number limits ($\mu_{mol}/\mu_{eff} \ll 1$), $\alpha \approx 1.393$. The coefficient of

thermal expansion, β , is defined as $\beta = -\frac{1}{\rho} \left(\frac{\partial \rho}{\partial T} \right)_p$. Y_M represents the contribution of the

fluctuating dilatation incompressible turbulence to the overall dissipation rate, calculated as:

$$Y_M = 2\rho\varepsilon M_t \quad , \quad M_t = \sqrt{\frac{k}{a^2}} \quad , \quad a = \sqrt{\gamma RT} \quad (59)$$

and $C_{1\varepsilon}$, $C_{2\varepsilon}$, and $C_{3\varepsilon}$ are constants. σ_k and σ_ε are the turbulent Prandtl numbers for k and ε , respectively. The turbulent (or eddy) viscosity, μ_t , is computed by combining k and ε as follows:

$$\mu_t = \rho C_\mu \frac{k^2}{\varepsilon} \quad , \quad C_\mu = \text{Constant} \quad (60)$$

The model constants have the following default values $G_{1\varepsilon} = 1.44$, $G_{2\varepsilon} = 1.92$, $G_\mu = 0.09$, $\sigma_k = 1.0$ and $\sigma_\varepsilon = 1.3$. The term G_k , representing the production of turbulence kinetic energy, is modeled identically for the standard and RNG. To evaluate G_k in a manner consistent with the Boussinesq hypothesis,

$$G_k = \mu_t S^2 \quad , \quad S \equiv \sqrt{2S_{ij}S_{ij}} \quad (61)$$

where S is the modulus of the mean rate-of-strain tensor. The RNG $k - \varepsilon$ model was derived using a rigorous statistical technique (called renormalization group theory). It is similar in form to the standard $k - \varepsilon$ model, but includes the following refinements:

- The RNG model has an additional term in its ε equation that significantly improves the accuracy of rapidly strained flows.
- The effect of swirl on turbulence is included in the RNG model, enhancing accuracy for swirling flows.
- The RNG theory provides an analytical formula for turbulent Prandtl numbers, while the standard $k - \varepsilon$ model uses user-specified, constant values.
- While the standard $k - \varepsilon$ model is a high-Reynolds-number model, the RNG theory provides an analytically-derived differential formula for effective viscosity that accounts for low-Reynolds-number effects. Practical use of this feature does, however, depend on the appropriate treatment of

the near-wall region. These features make the RNG $k - \varepsilon$ model more accurate and reliable for a broader class of flows than the standard $k - \varepsilon$ model. The RNG-based $k - \varepsilon$ turbulence model is derived from the instantaneous Navier-Stokes equations, using a mathematical technique called "renormalization group" (RNG) methods. The analytical derivation results in a model with constants different from those in the standard $k - \varepsilon$ model, and additional terms and functions in the transport equations for k and ε .

1.15. Shear-Stress Transport (SST) $k - \omega$ Model

The SST $k - \omega$ model gradually changes from the standard $k - \omega$ model in the inner region of the boundary layer to a high-Reynolds-number version of the $k - \varepsilon$ model in the outer part of the boundary layer. The shear-stress transport (SST) $k - \omega$ model was developed to effectively blend the robust and accurate formulation of the $k - \omega$ model in the near-wall region with the free-stream independence of the $k - \varepsilon$ model in the far field. To achieve this, the $k - \varepsilon$ model is converted into a $k - \omega$ formulation. These features make the SST $k - \omega$ model more accurate and reliable for a more comprehensive class of flows (e.g., adverse pressure gradient flows, airfoils, transonic shock waves) than the standard $k - \omega$ model.

The SST $k - \omega$ model has a similar form to the standard $k - \omega$ model [68]:

$$\frac{\partial}{\partial t}(\rho k) + \frac{\partial}{\partial x_i}(\rho k u_i) = \frac{\partial}{\partial x_j} \left(\Gamma_k \frac{\partial k}{\partial x_j} \right) + G_k - Y_k + S_k \quad (62)$$

$$\frac{\partial}{\partial t}(\rho \omega) + \frac{\partial}{\partial x_i}(\rho \omega u_i) = \frac{\partial}{\partial x_j} \left(\Gamma_\omega \frac{\partial \omega}{\partial x_j} \right) + G_\omega - Y_\omega + D_\omega + S_\omega \quad (63)$$

In these equations, G_k represents the generation of turbulence kinetic energy due to mean velocity gradients and G_ω represents the production of ω . Γ_k and Γ_ω represent the effective diffusivity of k and ω , respectively. D_ω represents the cross-diffusion term and are user-defined source terms.

The effective diffusivity for the SST $k - \omega$ model is given by Two-Equation Eddy-Viscosity Turbulence Models for Engineering Applications:

$$\Gamma_k = \mu + \frac{\mu_t}{\sigma_k} \quad (64)$$

$$\Gamma_\omega = \mu + \frac{\mu_t}{\sigma_\omega} \quad (65)$$

where σ_k and σ_ω are the turbulent Prandtl numbers for k and ω , respectively. The turbulent viscosity, μ_t , is computed as follows [68]:

$$\mu_t = \frac{\mu}{\omega} \frac{1}{\max\left[\frac{1}{\alpha^*}, \frac{SF_2}{\alpha_1\omega}\right]} \quad (66)$$

where S is the strain rate magnitude and

$$\sigma_k = \frac{1}{F_1/\sigma_{k,1} + (1-F_1)/\sigma_{k,2}} \quad (67)$$

$$\sigma_\omega = \frac{1}{F_1/\sigma_{\omega,1} + (1-F_1)/\sigma_{\omega,2}} \quad (68)$$

The blending functions, F_1 and F_2 , are given by

$$F_1 = \tanh(\phi_1^4) \quad (69)$$

$$\phi_1 = \min\left[\max\left(\frac{\sqrt{k}}{0.09\omega y}, \frac{500\mu}{\rho y^2\omega}\right), \frac{4pk}{\sigma_{\omega,2}D_\omega^+ y^2}\right] \quad (70)$$

$$D_{\omega}^{+} = \max \left(2\rho \frac{1}{\sigma_{\omega,2}} \frac{1}{\omega} \frac{\partial k}{\partial x_j} \frac{\partial \omega}{\partial x_j}, 10^{-10} \right) \quad (71)$$

$$F_2 = \tanh(\phi_2^4) \quad (72)$$

$$\phi_2 = \max \left[2 \frac{\sqrt{k}}{0.09\omega y}, \frac{500\mu}{\rho y^2 \omega} \right] \quad (73)$$

where y is the distance to the next surface and D_{ω}^{+} is the positive portion of the cross-diffusion term.

where G_k is defined in the same manner as in the standard $k - \omega$ model. The term G_{ω} represents the production of ω and is given by:

$$G_{\omega} = \frac{\alpha}{\nu_t} G_k \quad (74)$$

Note that this formulation differs from the standard $k - \omega$ model. The difference between the two models also exists in the way the term α_{∞} is evaluated. In the standard $k - \omega$ model, α_{∞} is defined as a constant (0.52). For the SST $k - \omega$ model, α_{∞} is given by

$$\alpha_{\infty} = F_1 \alpha_{\infty,1} + (1 - F_1) \alpha_{\infty,2} \quad (75)$$

where

$$\alpha_{\infty,1} = \frac{\beta_{i,1}}{\beta_{\infty}^*} + \frac{\kappa^2}{\sigma_{\omega,1} \sqrt{\beta_{\infty}^*}} \quad (76)$$

$$\alpha_{\infty,2} = \frac{\beta_{i,2}}{\beta_{\infty}^*} + \frac{\kappa^2}{\sigma_{\omega,2} \sqrt{\beta_{\infty}^*}} \quad , \quad \kappa = 0.41 \quad (77)$$

The term Y_k represents the dissipation of turbulence kinetic energy and is defined similarly as in the standard $k - \omega$ model. The difference is in the way the term f_{β}^* is evaluated. In the standard $k - \omega$

model, f_β^* is defined as a piecewise function. For the SST $k-\omega$ model, f_β^* is a constant equal to 1. Thus:

$$Y_k = \rho \beta^* k \omega \quad (78)$$

The term Y_ω represents the dissipation and is defined similarly as in the standard model. The SST $k-\omega$ model is based on both the standard $k-\omega$ model and the standard $k-\varepsilon$ model. To blend these two models, the standard $k-\varepsilon$ model has been transformed into equations based on k and ω , which leads to the introduction of a cross-diffusion term (D_ω). D_ω is defined as

$$D_\omega = 2(1-F_1)\rho\sigma_{\omega,2} \frac{1}{\omega} \frac{\partial k}{\partial x_j} \frac{\partial \omega}{\partial x_j} \quad (79)$$

The model constants are:

$$\alpha_{k,1} = 1.176, \sigma_{\omega,1} = 2.0, \alpha_{k,2} = 1.0, \sigma_{\omega,2} = 1.168, a_1 = 0.31, \beta_{i,1} = 0.075, \beta_{i,2} = 0.0828.$$

All additional model constants ($\alpha_\infty^*, \alpha_\infty, \alpha_0, \beta_\infty^*, R_\beta, R_k, R_\omega, \zeta^*$ and M_{i0}) have the same values as for the standard $k-\omega$ model.

1.16. Condensation model

As it was mentioned in the introduction section of this chapter the mechanistic models are usually the best for different geometries and operating conditions. In this section, mechanistic models for simulation of wall condensation in turbulent regime will be described.

1.17. Wall condensation using fully resolved boundary layer approach

The underlying assumption in the implementation of this approach is discussed by Dehbi et al. [71]. In this approach, it is assumed that the condensation rate is governed by the rate of diffusion of condensable gases toward the cold surface. In case of water vapor as the condensable species, the

mass fluxes for the non-condensable gas and water vapor at the liquid-vapor interface include both convective and diffusive components. Hence, one can write [71]:

$$\dot{m}_{nc}'' = \rho W_{nc} v - \rho D \frac{\partial W_{nc}}{\partial n} \quad (80)$$

$$\dot{m}_s'' = \rho W_s v - \rho D \frac{\partial W_s}{\partial n} \quad (81)$$

where W 's are the mass fractions, v the mixture velocity, ρ is the mixture density, D is the mass diffusion coefficient, and n the normal direction to the wall (liquid film). Using the fact that the mass fractions of the mixture add up to unity, the mixture mass flux at the liquid-vapor interface can be written as:

$$\dot{m}'' = \dot{m}_{nc}'' + \dot{m}_s'' = \rho v \quad (82)$$

Since the interface is impermeable to the non-condensable gas we have:

$$\dot{m}_{nc}'' = 0 \quad (83)$$

Hence the mass flux of water vapor condensing at the wall may be expressed as:

$$\rho v = \dot{m}_s'' = \frac{1}{(W_s - 1)} \rho D \frac{\partial W_s}{\partial n} \quad (84)$$

The Antoine equation is used to describe the vapor pressure as a function of the surface temperature:

$$\ln \left(\frac{P}{1 \text{ Pa}} \right) = A + \frac{B}{T + C} \quad (85)$$

The coefficients A, B, and C are fitted on data from steam tables. The result of this fitting process yields: A= +23.1512, B= -3788.02 K, and C= -47.3018 K. it should be mentioned that either of Eqs. (8) or (85) can be used to calculate the vapor pressure at the surface temperature. In condensation mass, flux calculation ρ and D are the mixture density and diffusion coefficient.

The condensation rate can be implemented as a sink in the continuity equation of cells adjacent to the cold wall. The result is:

$$\dot{m}_s'' = \dot{m}_s'' \frac{A_{cell-wall}}{V_{cell}} \quad (86)$$

where $A_{cell-wall}$ is the area of the cell on the wall and V_{cell} is the cell volume. In the simulation algorithm, it is assumed that condensation takes place if the wall temperature is less than or equal to the saturation temperature corresponding to the partial pressure of water vapor at the wall-adjacent cell. If the wall temperature is above the saturation temperature for given partial pressure of the vapor, the water vapor mass fraction at the wall is set to a value equal to the value in the wall adjacent cell. The partial pressure of the vapor in a mixture can be calculated using the following equations:

$$P_v = P_{mix} \frac{M_{mix} Y_v}{M_v} \quad (87)$$

where M_{mix} is the mixture molar mass, Y_v is the mass fraction of water vapor and M_v is the water vapor molar mass. To satisfy the local equilibrium assumption above, if the temperature is less than or equal to the saturation temperature, the water vapor mass fraction at the wall is assigned a value corresponding to the vapor saturation pressure at the local wall temperature. To alleviate the problem, we require that the rate at which species enters (or leaves) the computational domain is identical to the net rate at which mass enters (or leaves) the computational domain. To achieve this, the source term in the species equations at the wall adjacent cell must take the diffusive flux into account such as:

$$\dot{m}_s'' V_{cell} = \rho v W_s A_{cell-wall} - \rho D \frac{\partial W_s}{\partial n} A_{cell-wall} \quad (88)$$

Hence the sink term in the continuity equation for the cells adjacent to the walls is:

$$\dot{m}'' = \frac{1}{(W_s - 1)} \rho D \frac{\partial W_s}{\partial n} \frac{A_{cell-wall}}{V_{cell}} \quad (89)$$

A corresponding sink term needs to be included in the water vapor species equation:

$$\dot{m}_s'' = \dot{m}'' W_s \quad (90)$$

$$\dot{m}_s'' = \frac{W_s}{(W_s - 1)} \rho D \frac{\partial W_s}{\partial n} \frac{A_{cell-wall}}{V_{cell}} \quad (91)$$

The other volumetric sinks terms include velocity, energy, and turbulence sink terms for the cells adjacent to the condensing walls:

$$S_{j-mom} = U_j \frac{\dot{m}_s''}{W_{s,i}} \quad (92)$$

$$S_E = h_{fg} \frac{\dot{m}_s''}{W_{s,i}} \quad (93)$$

$$S_k = k_{cell} \frac{\dot{m}_s''}{W_{s,i}} \quad (94)$$

$$S_\omega = \omega_{cell} \frac{\dot{m}_s''}{W_{s,i}} \quad (95)$$

$$S_\varepsilon = \varepsilon_{cell} \frac{\dot{m}_s''}{W_{s,i}} \quad (96)$$

where S refers to the volumetric sinks, U_j to the mixture velocity in the j th direction, h_{fg} to the latent vapor enthalpy and are the turbulent kinetic energy, dissipation, and dissipation rate. The energy sink term will be applied to the near-wall cells in cases of adiabatic walls.

1.18. Wall condensation using wall function approach

In a turbulent regime, the condensation rate on the cold wall can be estimated based on the turbulent wall function [51]. In a turbulent boundary layer, the mass fluxes M_{A_w} and M_{B_w} of a non-condensable component (A) and a condensable component (B) of a binary gaseous mixture are given by:

$$M_{A_w} = M_{Mix} \cdot Y_{A_w} - k \cdot \rho \cdot (Y_{A_p} - Y_{A_w}) \quad (97)$$

$$M_{B_w} = M_{Mix} \cdot Y_{B_w} - k \cdot \rho \cdot (Y_{B_p} - Y_{B_w}) \quad (98)$$

where Y is the mass fraction, ρ the density and k is the turbulent mass transfer coefficient, which is a function of y^+ and the molecular Schmidt number, as in Kader [72]. Here, w subscripts refer to wall quantities; p subscripts refer to near wall mesh points. The equations above are a particular form of Fick's first law [72]. Since component A does not condense, $M_{B_w} = M_{Mix}$. Hence, M_{B_w} can be obtained as follow:

$$M_{B_w} = -k(y^+, Sc) \cdot \rho \cdot \frac{Y_{B_p} - Y_{B_w}}{1 - Y_{B_w}} \quad (99)$$

The value of Y_{B_p} is obtained from the solution of a transport equation for the condensable substance. The value of Y_{B_w} is calculated from the condensable component's molar fraction X_{B_w} , which is determined by assuming that the vapor is in thermal equilibrium with the liquid film at the interface, and hence its partial pressure is equal to its saturation pressure at the interface temperature.

Lee et al. [56] also used the wall function to calculate the condensation mass flux. They used the following condensation rate formulation with different correction factors:

$$\begin{aligned}
\dot{m}'' &= -K_{g,i} B \quad (\text{without suction correction}) \\
\dot{m}'' &= -K_{g,i} B \theta_b \quad (\text{with Bird's suction correction factor } : \theta_b) \\
\dot{m}'' &= -K_{g,i} B \theta_c \quad (\text{with Dehbi's suction correction factor } : \theta_c)
\end{aligned} \tag{100}$$

where $K_{g,i}$ is the mass transfer coefficient, $B = \frac{m_{v,i} - m_{v,b}}{1 - m_{v,i}}$, $\theta_b = \frac{\ln(1+B)}{B}$ and $\theta_c = \frac{1}{2}(1 + \theta_b)$. The

mass transfer coefficient was obtained from the wall function approach introduced in Martin-Valdepenas et al. [73] based on the heat and mass transfer analogy as below:

$$K_{g,i} = H_{g,i} \left(\frac{\rho_g D_g}{k_g} \right) \left(\frac{Sc}{Pr} \right)^{1/3} \tag{101}$$

in this equation, the mass transfer coefficient ($K_{g,i}$) was evaluated from the convection heat transfer coefficient ($H_{g,i}$), calculated using the wall law.

1.19. Volumetric condensation

Volumetric condensation can be modeled by “return to saturation in constant time scale” method. Based on this method, the energy needed for heating up the mixture to the saturation temperature is released by condensation during the numerical time step Δt :

$$Q_{V1} = c_{p,m} \rho_m \frac{T_{sat}(p_v) - T_m}{\Delta t} [W/m^3] \quad \text{if } T < T_{sat}(p_v) \tag{102}$$

If the conditions for condensation exist in given cell, vapor starts to condense immediately, and temperature increases towards to saturation temperature in this cell. Energy Q_{V1} must be limited according to a mass fraction of vapor in the cell:

$$Q_{V2} = \rho_m Y_v \frac{h_{fg}}{\Delta t} [W/m^3] \tag{103}$$

$$Q_V = \min(Q_{V1}, Q_{V2}) \quad (104)$$

Amount of steam which condenses in volume is calculated from energy Q_V .

$$S_{v,V} = \frac{-Q_V}{h_{fg}} < 0 \quad [kg/m^3.s] \quad (105)$$

where, $c_{p,m}$ [J/kg/K] is the isobaric heat capacity of mixture, $T_{sat}(p_v)$ [K] is the saturation temperature, T_m [K] is the temperature of the mixture, Δt [s] is the numerical time step, p_v [Pa] is the partial pressure of vapor, h_{fg} [J/kg] is the latent heat and Y_v [kg/kg] is the vapor mass fraction. The time step in the unsteady simulation can be replaced with an under-relaxation factor as described in [74].

1.20. Numerical validation and implementation

Validation of the numerical cases for wall condensation has been carried out by comparing the results of the numerical simulations with previous analytical, experimental and numerical works. The simulations have been done by using ANSYS FLUENT commercial code [48] and the UDF which has been developed for the simulation of the condensation process. In all of the numerical simulations the following numerical schemes have been used unless it is mentioned:

- The coupled algorithm was to handle the pressure-velocity coupling.
- The Green-Gauss Cell-based method was utilized for spatial discretization of the gradient.
- For the pressure equation, the second order discretization was used.
- Third order MUSCL scheme was used for discretization of momentum, species transport, and energy equations.
- Second order upwind method was used for discretization of turbulence equations.

1.21. Validation of condensation rate against an analytical solution

The first validation test was performed against the analytical solution of condensation in forced convective laminar flow of vapor and air over a horizontal cold flat plate without considering the gravitational force. Sparrow et al. [50] have obtained the analytical solution for this problem by solving the boundary layer equations for both the gas mixture and film. Using the similarity transformations, they reduced the governing equations to a set of ODE's. The following simplifications have been done during solution procedure:

- Convection in the liquid film was neglected.
- Interface velocity in the streamwise was zero.
- Temperature jump across the interface and interfacial resistance.
- Volumetric condensation was neglected, and wall condensation was modeled.

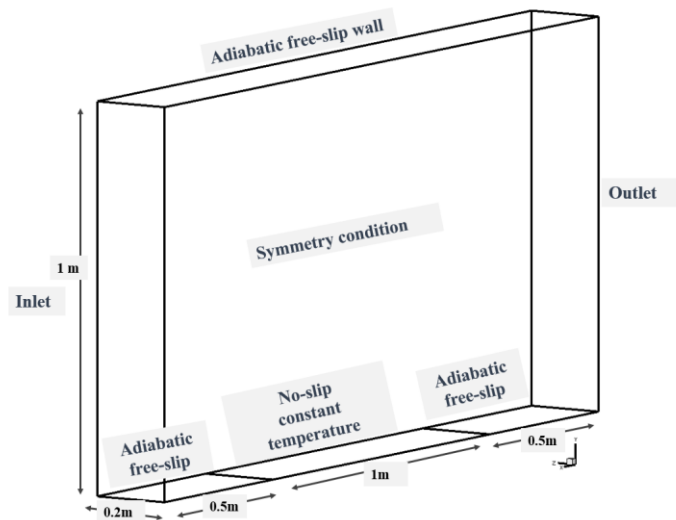
The condensation rate obtained from the analytical solution for the air-water vapor mixture when the non-condensable mass fraction was 0.05, and the surface temperature of the flat plate was 364.81 K. The condensation rate based on the analytical solution of condensation over a flat plate is obtained using the Matlab code [75] provided in the Appendix.

The numerical simulation of condensation over the flat plate, corresponding to the analytical solution [50], was performed using a 3D model in ANSYS FLUENT 16. For simulation of the condensation process, the UDFs for calculation of species and mixture properties, condensation rate, and pertinent sources/sinks have been implemented in the setup. The boundary conditions and setup parameter for the laminar forced convection wall condensation case are shown in Table 6. All the thermodynamic properties of air and water are a function of temperature.

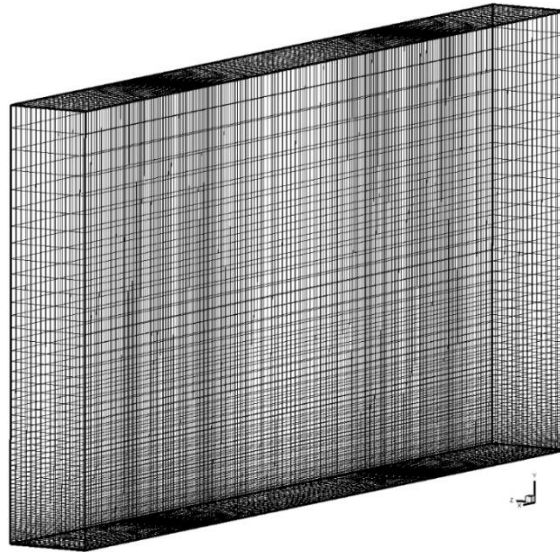
Table 6. Parameters for wall condensation over a flat plate in laminar forced convection flow.

Setting	Value
Inlet velocity [m.s-1]	1
Reference pressure [Pa]	101 325
Outlet relative average static pressure [Pa]	0
Inlet static temperature [K]	373.15
Flat plate temperature [K]	364.81
M (mass fraction of non-condensable gas)	0.05

Computational domain and grids are also shown in Figure 12. A uniform inlet velocity with constant water vapor mass fraction has been applied to the entrance of the computational domain while the outlet static gauge pressure is set to 0.



a) Computational domain



b) computational grid

Figure 12. Computational domain and grid for laminar wall condensation problem.

Figure 13 shows the comparison between the analytical solutions of condensation over a flat plate with the current numerical results. As can be seen, the results are in a good agreement.

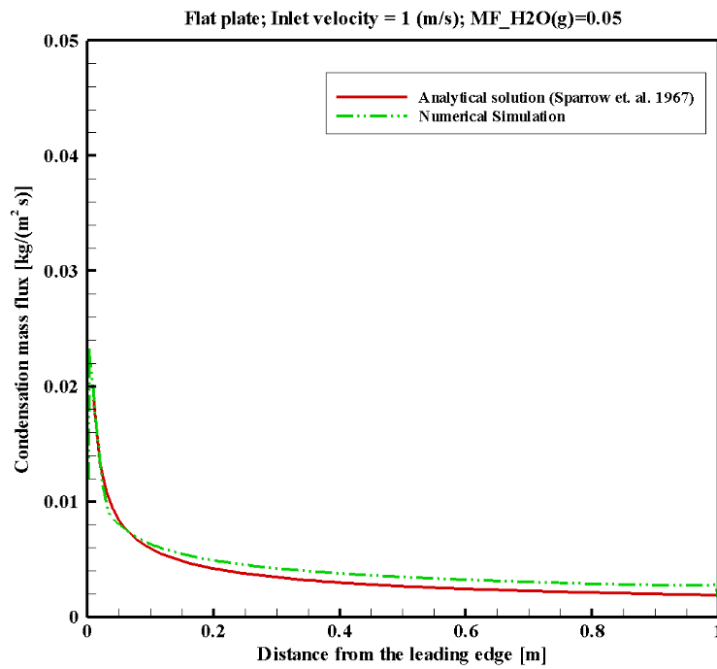


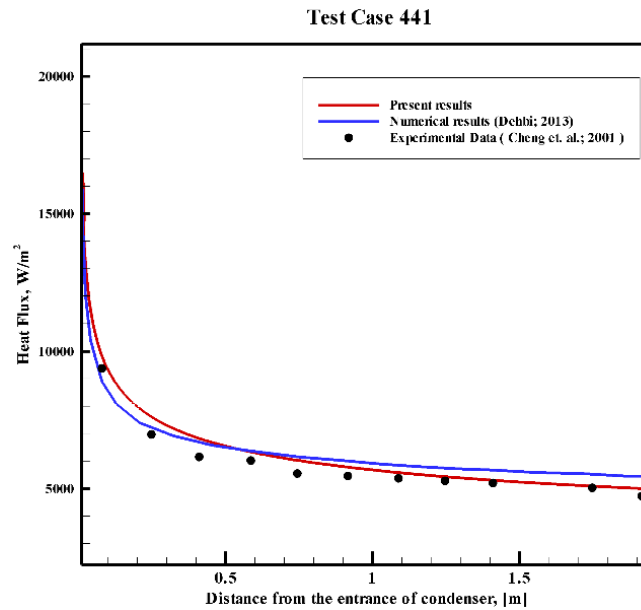
Figure 13. Condensation flux for at 1 m/s over an isothermal flat plate at 364.81 K, MF=0.05.

1.22. Validation of heat flux on a condensing wall

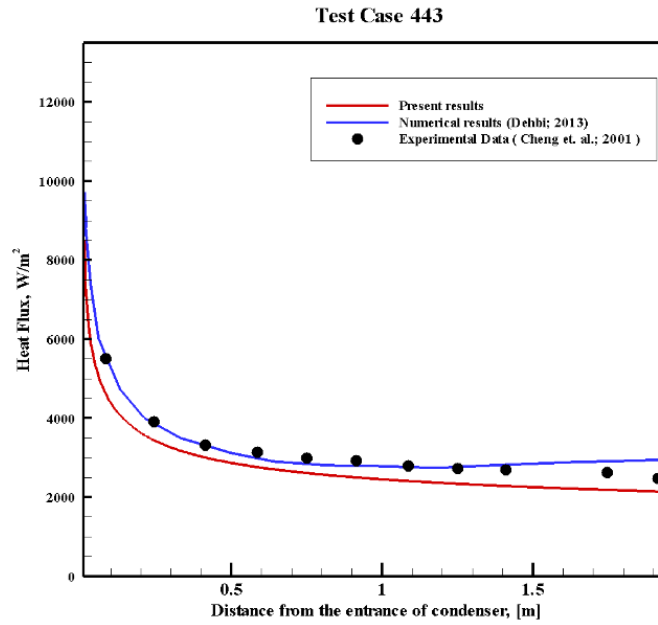
One of the most important parameters in condensation heat transfer is the value of heat flux on a condensing wall. This parameter is especially important for the case with an adiabatic wall or when conjugate heat transfer is one of the boundary conditions in a problem. The total heat flux on the wall can be calculated as [76]:

$$Q_{wall} = -k \left. \frac{\partial T}{\partial y} \right|_w + m_w'' \lambda_{fg} \quad (106)$$

where Q_{wall} is the total wall heat flux and k , m_w'' and λ_{fg} are thermal conductivity, condensation mass flux and latent heat of condensation for the water vapor. To verify the accuracy of the present setup and UDFs, the wall flux is compared with the numerical results obtained by Dehbi [53] and experimental results of Cheng et al. [76]. The k- ω -SST turbulent model is used for this simulation.



(a)



(b)

Figure 14. Validation of heat flux on the condensing wall.

Comparison between the present results and previous works shows the accuracy of the current implementation of the condensation model on a solid wall. In the next chapter, a condensation model based on this implementation will be applied for the condensation on a TMC tube. In the following chapters, the wall condensation model will be modified to consider the model the condensation over the TMC walls and capillary condensation inside the nanopores.

3. Chapter 3: Modeling and simulation procedure for TMC heat exchangers

1.23. Laboratory investigation and numerical simulations

In this chapter, the diffusion-based simulation of heat and mass transfer inside a TMC heat exchanger will be developed and described in detail. The method is based on the condensation model on a solid wall in which a correction factor has been implemented. These correction factors are obtained based on the experimental results provided by GTI. The experiment has been carried out at GTI's research laboratory, and the primary focus of this chapter is to provide an accurate simulation scheme for TMC heat exchangers. The details of the experiment will not be discussed here.

1.24. Critical dimensions and Schematic of the experimental apparatus

Figure 15 shows the test section and the experimental rig for the lab scale TMC heat exchanger. The experimental setup was equipped with pressure, different, humidity, temperature, flow rate measurements and complete gas analysis. The measured data during the experiments were collected and stored using the data acquisition system in the setup. The amount of recovered water was obtained from the difference between the inlet and outlet humidity of flue-gas passes through the TMC module. The TMC heat exchanger was installed horizontally, and the flue-gas was flowing upward through the TMC tube banks. The TMC heat exchanger has 78 TMC tubes each 18 inches length. The lab scale TMC heat exchanger module is shown in Figure 16. The TMC heat exchanger unit has been assembled using a two-part epoxy-based adhesive and glass-filled epoxy-based materials.



Figure 15. Experimental rig and the test section for the lab scale TMC heat exchangers.



Figure 16. Lab scale TMC heat exchanger [1].

Schematic of the test section and the location of different sensors and parts are shown in Figure 17. In the schematic of the test rig: 1 is the natural gas flow meter; 2 is the compressed air flow meter; 3 is the natural gas combustor; 4 is the water injection nozzle; 5 is the water flow meter; 6 is the flue gas cooling section; 7 is the test duct; and 8 is the porous membrane tube bundle or stainless steel.

As seen the exhaust flow gas from the combustor is cooled down to the desired temperature by using the cooling unit in the system. This temperature is in the range of flue gas temperature in the real-world application for the TMC heat exchangers. After passing the cooling unit the flue gas is directed upward through the tube banks of the test section. The cold water flows through the TMC tubes perpendicular to the direction of the flue gas which results in a cross-flow arrangement for the TMC heat exchangers. In the waterside, a negative pressure was held using a vacuum generator. The inlet temperature of the cooling water was also adjusted to the real world application temperature by using an electrical heating unit. To monitor the condensation process inside the TMC heat exchanger, an observation window was installed into the wall of the test section. The

temperature, flow rate, and humidity have been measured using thermocouples, flow meters and hygrometers at different parts of the test rig.

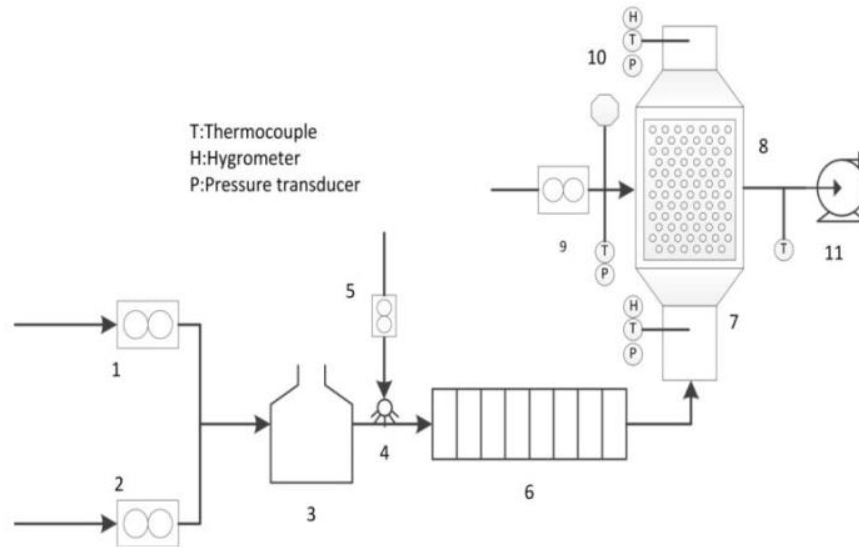


Figure 17. Schematic of experimental apparatus [25].

The schematic and critical dimensions of the test section with the symmetry plane is shown in Figure 18 and Table 7.

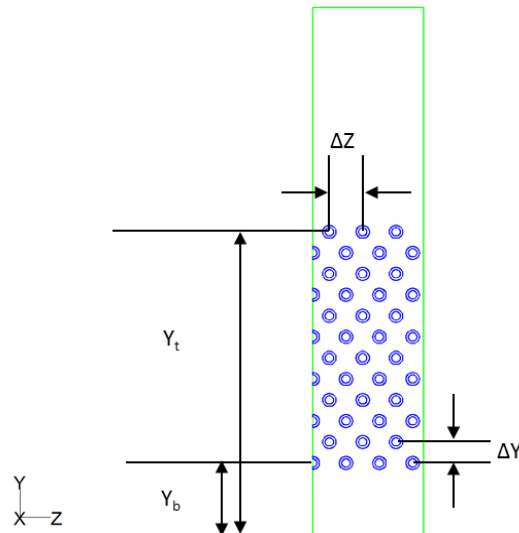


Figure 18. Schematic of the tube arrangement.

Table 7. Critical dimensions of the test section.

Coordinate	Direction	Dimension (inch)
X	Water flow direction	17
Y	Flue gas flow direction	8.7
Z	From the center-symmetric plane to the side wall	1.7875

Moreover, the tube sizes and pitches for the lab scale TMC heat exchanger is shown in Table 8.

Table 8. Critical dimensions of the tubes and bundle arrangement.

		Dimension (inch)
The ceramic tube	Inside Diameter (ID)	0.138
	Outside Diameter(OD)	0.216
	The thickness of the tube wall	0.039
The arrangement of the tubes	Tube spacing in the Y direction ΔY (center to center)	0.346
	Tube spacing in the Z direction ΔZ (center to center)	0.536
	The bottom row of tubes location Y_b from the inlet	1.200
	The top row of tubes location Y_t from the inlet	5.006

1.25. Boundary conditions and thermodynamic properties

Figure 19 shows the computational domain, inlet, and outlet for the cooling water and flue-gas streams inside a cross-flow TMC heat exchanger.

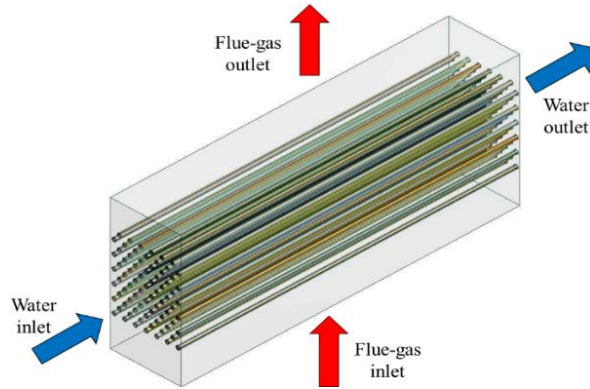


Figure 19. Schematic of the computational domain and boundary conditions.

Table 9 shows the boundary condition list for the numerical simulation setup. A single phase multi-species transport model is used to predict the heat and water transfer inside the TMC heat exchanger.

Table 9. Summary of the different zones and boundary conditions in the numerical setup.

Location	Zone name	Zone type
Flue-gas zone	Flue gas	Mixture
Water zone	Water	Mixture
Membrane zone	Porous	Mixture-porous
Flue-gas flow inlet	inlet flue	Velocity-inlet
Flue-gas flow outlet	outlet flue	Pressure-outlet
Water flow inlet	inlet water	Velocity-inlet
Water flow outlet	outlet water	Pressure-outlet
Central symmetric surface	Symmetry-porous Symmetry-water Symmetry-flue gas	Symmetry
Tube inside surface	Porous-water-interior	Interior
Tube outside surface	Flue gas-porous-wall	Wall (conjugate boundary condition)

Side Wall	Sidewall-flue gas Sidewall-porous	Wall (Adiabatic thermal condition, heat flux=0)
-----------	--------------------------------------	---

It should be mentioned that the interface wall between the porous and zones are changed to the interior type to make the water transfer from the Flue-gas zone to the permeable region and from that to the water zone possible. The data is related to a typical experimental setup for the TMC module test at GTI's lab is shown in Table 10.

Table 10. Typical experimental results for the lab scale TMC rig.

Case No.	48	Symbol
Gas Flow rate (SCFH)	201.6	
O ₂ at stack (%)	3.84%	F_{o_2}
Vacuum(psi)	-3	P_{vacuum}
Flue gas flow rate(SCFH)	2551	RF_{flue}
Water flow rate(gpm)	0.34	RF_{water}
Flue Inlet Temp (°F)	200	T_{fluein}
Flue Outlet Temp (°F)	137.6	$T_{flueout}$
Water Inlet Temp (°F)	100.2	$T_{waterin}$
Water Outlet Temp (°F)	129.3	$T_{waterout}$
Vapor Transportation Rate	24.4%	
Flue inlet dew point(°F)	134.75	T_{din}
Flue inlet relative humidity	21.93%	V_{in}
Flue outlet dew point(°F)	124.8	T_{dout}
Flue outlet relative humidity	69.9%	V_{out}

The flue-gas flow inlet temperature T_{fluein} is obtained from experimental data, and velocity U_{flue} is calculated using the following equation, from the volume flow rate of the flue-gas RF_{flue} .

$$U_{flue} = \frac{\dot{V}}{Area} = \frac{RF_{flue}(SCFH)}{2 \times 3600} \times \frac{(460 + T_{fluein})}{(460 + 80)} \times \frac{1}{1.7875/12 \times 17/12} \quad (107)$$

The inlet velocity of water U_{water} is calculated using the following equation RF_{water} .

$$U_{water} = \frac{\dot{V}}{Area} = \frac{RF_{water}(GPM) \times 3.785 \times 10^{-3} (m^{-3} / gallon)}{60 \times 78 \times \pi \times (3.5 \times 10^{-3} / 2)^2} \times 3.2808 (ft / meter) \quad (108)$$

The outlet pressure for the water and the flue gas are P_{vacuum} and atmosphere, respectively. The flue-gas inlet species mass fraction is shown in Table 11. There are four species in the flue gas, vapor, O₂, CO₂, and N₂. The vapor fraction of vapor F_{vapor} is calculated from the flue inlet dew point, T_{din} . The O₂ fraction comes from the experimental data, and the mass fraction of N₂ can be calculated by subtracting the sum of the specified mass fractions from 1.

Table 11. Inlet mass fraction of different species for the flue-gas.

Species	Mass Fraction
H ₂ O (vapor)	F_{vapor}
O ₂	F_{o2}
CO ₂	9%
N ₂	The balance of 100%

1.26. Thermodynamic properties of the flue-gas mixture

As it was mentioned in the previous chapter, the thermodynamic properties of the mixture will be calculated based on the thermodynamic properties of each species and the mass fraction for them in the mixture. The thermodynamic properties of the water vapor have already implemented in the numerical setup and been used for validation of the condensation model on the solid wall. Thermodynamic properties of the other non-condensable species (Table 12), i.e., N₂, O₂, and CO₂ are obtained from the NIST database [77]. These properties have been implemented in the numerical method using 5 points piecewise-linear function for the temperature variation range of the experiment. The temperature range for the experimental data is between 293.15 to 366.4 (K) which are the maximum flue-gas inlet and minimum cooling water inlet temperatures.

Table 12. Thermodynamic properties of the other non-condensable species.

Nitrogen (N ₂)					
Temperature	T ₁ = 293.15 (K)	T ₂ = 311.4 (K)	T ₃ = 329.8 (K)	T ₄ = 348.1 (K)	T ₅ = 366.4 (K)
Density (kg m ⁻³)	1.1648	1.0961	1.0351	0.98046	0.93135
Specific heat (J kg ⁻¹ K ⁻¹)	1041.3	1041.4	1041.7	1042.2	1043
Thermal conductivity (W m ⁻¹ K ⁻¹)	0.025398	0.026621	0.027817	0.028990	0.030142
Dynamic viscosity (kg m ⁻¹ s ⁻¹)	1.7580e-05	1.8422e-05	1.9243e-05	2.0044e-05	2.0828e-05
Oxygen (O ₂)					
Temperature	T ₁ = 293.15 (K)	T ₂ = 311.4 (K)	T ₃ = 329.8 (K)	T ₄ = 348.1 (K)	T ₅ = 366.4 (K)
Density (kg m ⁻³)	1.3312	1.2526	1.1828	1.1204	1.0642
Specific heat (J kg ⁻¹ K ⁻¹)	918.95	921.63	924.88	928.66	932.90
Thermal conductivity (W m ⁻¹ K ⁻¹)	0.026105	0.027581	0.029053	0.030524	0.031995
Dynamic viscosity (kg m ⁻¹ s ⁻¹)	2.0182e-05	2.1189e-05	2.2173e-05	2.3136e-05	2.4077e-05
Carbon dioxide (CO ₂)					
Temperature	T ₁ = 293.15 (K)	T ₂ = 311.4 (K)	T ₃ = 329.8 (K)	T ₄ = 348.1 (K)	T ₅ = 366.4 (K)
Density (kg m ⁻³)	1.8393	1.7294	1.6320	1.5451	1.4671
Specific heat (J kg ⁻¹ K ⁻¹)	846.06	863.56	880.72	897.43	913.61

Thermal conductivity (W m ⁻¹ K ⁻¹)	0.016242	0.017725	0.019237	0.020769	0.022313
Dynamic viscosity (kg m ⁻¹ s ⁻¹)	1.4689e-05	1.5575e-05	1.6451e-05	1.7315e-05	1.8168e-05

1.27. Turbulence model

One of the most important parameters which affect the accuracy of numerical simulation of the condensation process is the selection of an appropriate turbulence model. In case of turbulent model selection and boundary layer treatment, two options are available: using the wall-function or fully resolving the boundary layer. As it has been demonstrated by Dehbi [53] the grid resolution near the condensing wall is one of the most important parameters in the feasibility of the numerical simulation of condensation problems. Using the wall function near the solid wall is the natural choice which reduces the number of the computational grid in the solution domain. But it should be noted that using the wall function results in a substantial underprediction of heat transfer compared to the fully resolved boundary layer approach and experimental data. On the other hand, both near wall approaches can predict the condensation rate and heat transfer with acceptable accuracy.

Considering the point above and the physics of the flow through the tube bundles, the *K- ω -SST* model will be used for numerical simulation of the condensation in the cross-flow TMC heat exchanger. To achieve an acceptable accuracy a fine grid near the condensing wall ($Y^+ < 2$) needs to be generated near the outer wall of the TMC tubes.

1.28. Thermophysical properties of the TMC tubes

Thermophysical properties of the TMC tubes need to be calculated and applied in the numerical simulation. Table 13 [1], [78] show the thermophysical properties of the TMC tubes.

Table 13. Dimensions and physical properties of different types of TMC tubes.

Material	Ceramic
ID (inch)	0.138
OD (inch)	0.216
Density (kg m ⁻³)	3790
heat capacity (J K ⁻¹ kg ⁻¹)	775
Solid material thermal conductivity (W m ⁻¹ K ⁻¹)	30
Porosity	20%
Porous substrate pore size (μm)	4

The fluid flow and heat transfer inside the TMC tubes have been solved by considering the TMC tube/ membrane as a porous media [48]. The effective thermal conductivity for the TMC tube will be obtained based on the following equation:

$$k_{\text{eff}} = \gamma k_f + (1 - \gamma) k_s \quad (109)$$

where γ is the porosity of the medium, k_f is the fluid phase thermal conductivity and k_s is the solid medium thermal conductivity. Viscous resistance coefficient ($1/\alpha$) is one of the parameters which needs to be determined in the setup and α is the permeability of the porous medium. The permeability of the porous medium can be calculated using the following equation:

$$\alpha = \frac{\gamma d_p^2}{72(1 - \gamma)^2 \tau} \quad (110)$$

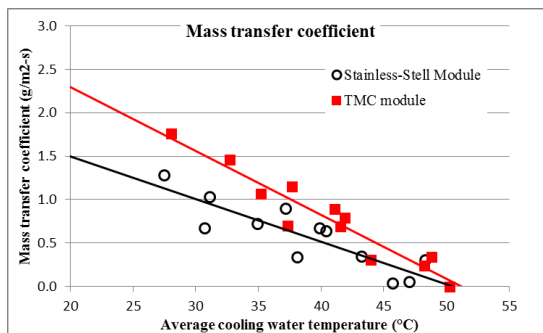
where τ is the tortuosity of the porous medium and can be obtained using the following equation [79]:

$$\tau = 1 - \frac{1}{2} \ln(\gamma) \quad (111)$$

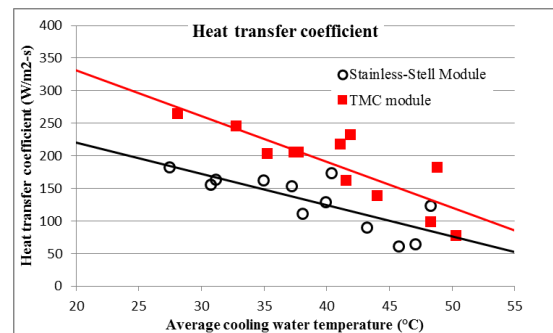
By using the specification of the TMC tubes, the value of the viscous resistance coefficient is 3.24×10^{11} .

1.29. Condensation model for the TMC heat exchanger and simulation algorithm

As it was mentioned before one of the options for simulation of condensation on the TMC tube surface is to use the solid wall condensation model with appropriate correction factors based on the experimental data. The data series provided by GTI [25] based on the lab scale TMC heat exchanger setup is shown in Figure 20. As seen in the figure, the heat and mass transfer coefficients for the lab scale TMC and stainless-steel heat exchangers follow the same trend. For both types of tubes, the mass transfer (condensation rate) and heat transfer coefficients are decreasing as the average cooling water or interface temperature increased. By comparison of the performance of the TMC heat exchanger with the stainless-steel heat exchanger, it can be concluded that using the solid wall condensation model by incorporating some correction factors would be possible.



(a)



(b)

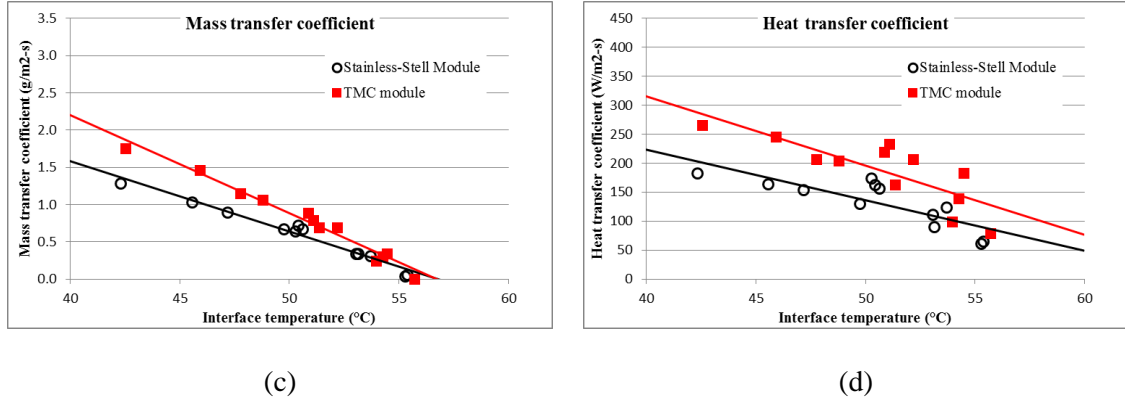


Figure 20. Heat and mass transfer coefficient of TMC and stainless-steel heat exchangers.

To adapt the solid wall condensation model for the TMC tubes the following points need to be taken into account:

- 1- Based on the Kelvin equation, capillary condensation in nano-pores occurs for the partial pressure of the condensing species lower than its vapor pressure (The capillary condensation will be addressed in detail in the next chapter using the mixed model).
- 2- The condensation rate on the surface of the TMC tubes needs to be adjusted based on the available experimental data points.

To address the points above, the condensation rate has been modified using the following equation:

$$\dot{m}'' = C_1 \frac{1}{(W_s - 1)} \rho D \frac{\partial W_s}{\partial n} \frac{A_{cell-wall}}{V_{cell}} \quad (112)$$

where the constant C_1 is obtained from the available experimental results. Moreover, the criteria for the starting point of condensation rate (vapor saturation pressure at the local wall temperature) has been modified by implementing the second correction factor C_2 . Figure 21 shows the schematics of different zones and domains which have been used for the numerical setup. The condensation rate in the flue-gas side is calculated using the modified equation which includes the

correction factors. The sink terms which have been used for the condensation rates in the flue gas domain include the mass, species, momentum and turbulent sinks.

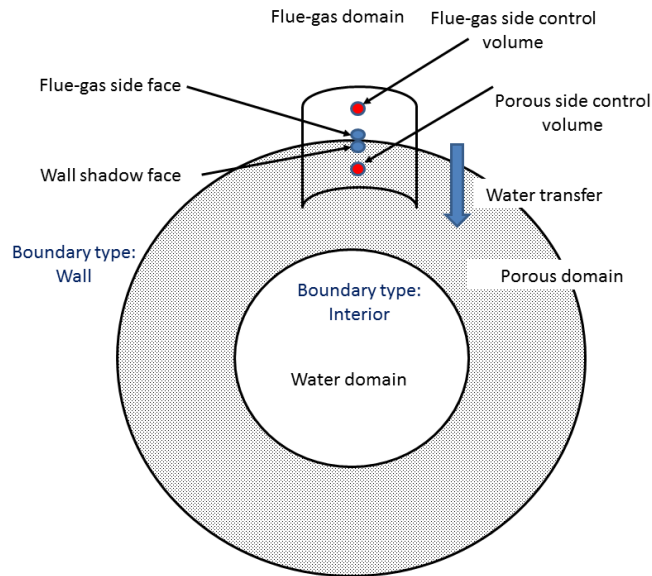


Figure 21. Schematic of different zones in the numerical setup.

To apply for the water and energy transfer from the flue-gas side to the porous wall in the numerical setup the appropriate source terms need to be applied to the cells adjacent to the wall in the porous zone. The source terms include mass, species, and energy sources. It should be noted the species sources has been added to the liquid water transport equation while in the flue-gas side the species sink term was applied to the water vapor equation. Moreover, the heat source has been applied only to the porous wall side. This is consistent with using the wall as an infinite reservoir [48]. List of the UDFs and they rule in the numerical simulations are presented in Appendix 2. Transport of the condensed water from the porous domain to the cooling water domain is applied by converting the interface type of the two domain from the wall to interior.

1.30. Numerical simulation of the heat and mass transfer in a TMC heat exchanger

Simulation of the heat and mass transfer inside the TMC heat exchanger has been performed using Ansys Fluent V16. A single multi-species transport model has been used to model the transport equations of different species in the computational domain. The second order upwind discretization scheme is used for the special discretization for all the governing equations except the turbulent equations. The coupled algorithm is used for pressure-velocity coupling with appropriate Courant number and under-relaxation. The convergence criteria are set to 10^{-8} for all the transport equations. Moreover, the outlet parameters i.e., the cooling water outlet temperature, flue-gas outlet temperature, and condensation rate are monitored to confirm the solution convergence. The UDFs are mounted to the solution setup to account for the condensation and water transfer process and the User Defined Memories (UDMs) is used to store the calculated values between the UDFs. The boundary conditions (inlet velocity, temperature, species mass fraction) and material properties are the same as the lab-scale experimental setup.

Figure 22 shows the geometry and computational grid for the numerical setup. The symmetry plane is used to reduce the computational time due to the symmetric pattern of the boundaries and geometry in all the simulations.



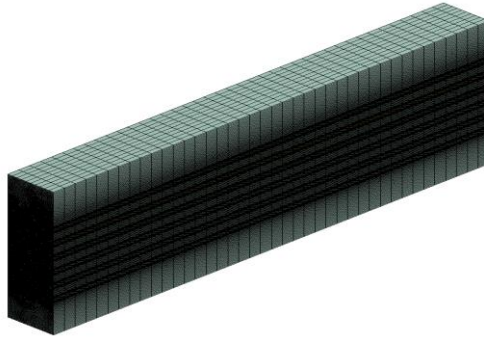


Figure 22. Geometry and computational grid for the lab scale TMC module.

The grid independence study is conducted for the case which has the closest inlet values to the averaged inlet condition of the experimental cases. Also, for the grid independence study is carried out for the case without condensation since the correction factors have not been specified before the grid independence study. different species is calculated to form the volume fraction from the experimental data.

Table 14 shows the boundary and working conditions for the experimental case which has been used for the grid independence study and calculation of the model constants. The inlet mass fraction of different species is calculated to form the volume fraction from the experimental data.

Table 14. Boundary and working conditions for the computational model.

Natural gas flow rate (SCFH)	201.3
Flue inlet T (°F)	179.0
Flue inlet dew point (°F)	132.4
Flue inlet Humidity (%)	32.306
Flue outlet T (°F)	129.208
Flue outlet Humidity (%)	87.756
Flue outlet dew point (°F)	124.37
Water inlet FR (gpm)	0.339
Water inlet T (°F)	89.40
Water outlet T (°F)	124.12
TMC vacuum ("Hg)	-5.93
CALCULATED PARAMETERS	
<i>Flue Gas SCF/SCF Gas (based on fuel and O2 reading)</i>	
O ₂	0.0945
N ₂	7.82

CO ₂	0.965
H ₂ O	2.119
Total Flue Gas Flow (SCFH)	2216.0
Inlet Mass Fraction of Species	
O ₂	0.04
N ₂	0.756
CO ₂	0.09
H ₂ O	0.114
Water transferred (lb/h)	3.1
Water transferred (%)	19.48

Variation of the outlet flue gas and water temperatures have been plotted in Figure 23. As seen the total number of 2.8 million control volume ensures the grid independence of the numerical simulations.

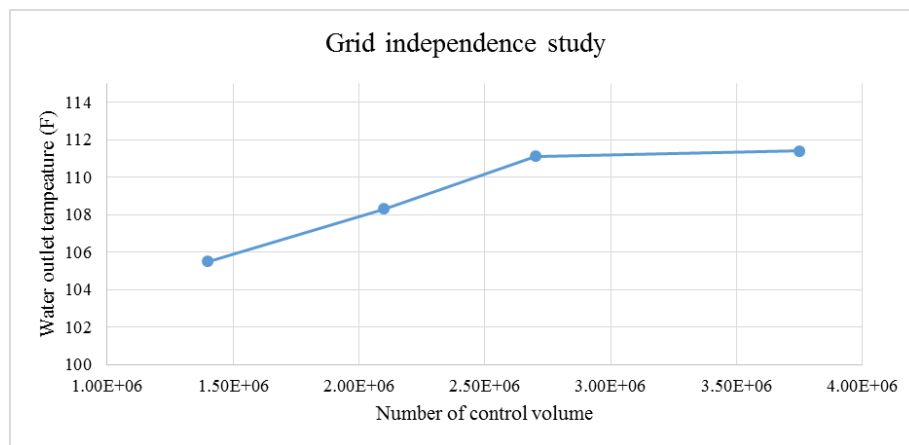


Figure 23. Grid independence study for the cross-flow heat TMC heat exchanger modeling

To validate the proposed simulation algorithm for modeling of TMC cross flow heat exchangers the numerical results are validated against the available experimental data from a lab scale TMC test rig. The data series for 11 test case are presented in Table 15 and Table 16 which are provided by GTI.

Table 15. Inlet and outlet conditions for the experimental cases 1-6.

Test Case		1	2	3	4	5	6
-----------	--	---	---	---	---	---	---

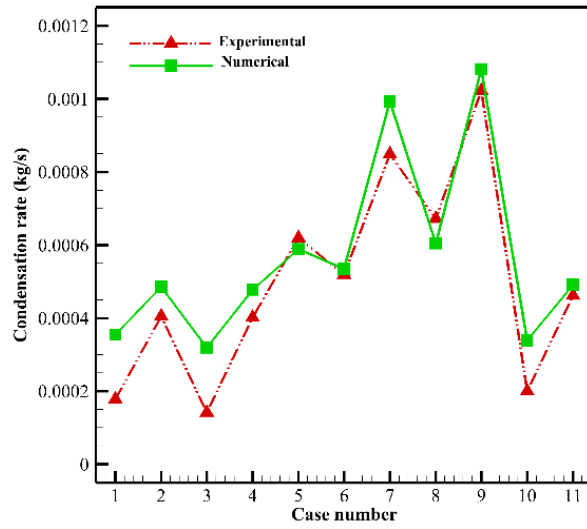
Natural gas flow rate	SCFH	201.23	201.23	200.44	201.35	201.29	200.89
Flue inlet T	°F	179.26	179.67	180.40	179.00	179.86	180.92
Flue inlet dew point	°F	132.59	132.72	131.83	132.43	132.75	132.83
Flue inlet Humidity	%	32.25	32.07	30.83	32.31	31.96	31.29
Flue outlet T	°F	127.34	122.10	134.20	129.21	124.47	121.44
Flue outlet Humidity	%	105.19	107.21	87.37	87.76	87.68	102.06
Flue outlet dew point	°F	129.22	124.64	129.11	124.37	119.69	122.18
Water inlet FR	gpm	0.20	0.20	0.32	0.34	0.33	0.51
Water inlet T	°F	90.99	69.41	108.57	89.41	70.22	89.81
Water outlet T	°F	131.30	129.03	129.21	124.13	120.61	122.04
Flue Gas SCF/SCF Gas (based on fuel and O2 reading)							
O2		0.095	0.095	0.095	0.095	0.095	0.095
N2		7.826	7.826	7.826	7.826	7.826	7.826
CO2		0.966	0.966	0.966	0.966	0.966	0.966
H2O		2.120	2.120	2.120	2.120	2.120	2.120
Total Flue Gas Flow	SCFH	2214.781	2214.772	2206.061	2216.091	2215.390	2210.983
Flue-gas inlet velocity	(ft/s)	1.726	1.727	1.722	1.726	1.728	1.727
Water inlet velocity	(ft/s)	0.055	0.056	0.088	0.094	0.090	0.140
*VOLUME FRACTION_FG_IN							
O2		0.00859	0.00859	0.00859	0.00859	0.00859	0.00859
N2		0.71110	0.71110	0.71110	0.71110	0.71110	0.71110
CO2		0.08773	0.08773	0.08773	0.08773	0.08773	0.08773
H2O		0.19259	0.19259	0.19259	0.19259	0.19259	0.19259
Water transferred	lb/h	1.40823	3.21313	1.12296	3.18729	4.91717	4.11997
Water transferred	%	8.57852	19.50375	7.00693	19.48402	29.81969	24.97918
Deviation from the ACR		2.53774	0.73284	2.82301	0.75868	-0.97120	-0.17400
Full geometry condensation rate (kg/s)		0.000177	0.00018	0.00041	0.00014	0.00040	0.00062
Half geometry condensation rate (kg/s)		8.87E-05	0.00009	0.00020	0.00007	0.00020	0.00031

Table 16. Inlet and outlet conditions for the experimental cases 7-11.

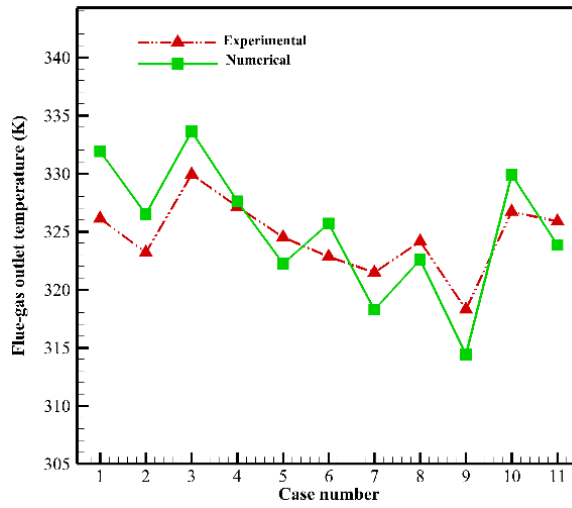
Test Case		7	8	9	10	11
Natural gas flow rate	SCFH	201.752	201.4995	201.7379	201.0938	201.767
Flue inlet T	°F	179.1097	180.3891	178.5629	161.2943	161.0441
Flue inlet dew point	°F	133.227	132.5709	132.7914	133.2667	133.0482
Flue inlet Humidity	%	32.91077	31.43956	32.93386	49.6194	49.62848
Flue outlet T	°F	118.9894	123.797	113.2607	128.4271	126.9047
Flue outlet Humidity	%	87.92478	85.55487	87.14712	102.9484	91.91912
Flue outlet dew point	°F	114.4093	118.1503	108.4766	129.512	123.8023
Water inlet FR	gpm	0.49642	1.013493	1.04987	0.335131	0.332944
Water inlet T	°F	68.27231	89.99988	69.42536	109.8368	89.02369
Water outlet T	°F	113.5186	109.6841	95.5274	129.8911	125.7128
Flue Gas SCF/SCF Gas (based on fuel and O2 reading)						
O2		0.094581	0.094581	0.094581	0.094581	0.094581
N2		7.826317	7.826317	7.826317	7.826317	7.826317
CO2		0.9655	0.9655	0.9655	0.9655	0.9655
H2O		2.119588	2.119588	2.119588	2.119588	2.119588
Total Flue Gas Flow	SCFH	2220.48	2217.7	2220.325	2213.236	2220.645
Flue-gas inlet velocity	(ft/s)	1.729671	1.730964	1.72807	1.67597	1.680904
Water inlet velocity	(ft/s)	0.136906	0.279508	0.28954	0.092425	0.091822
*VOLUME FRACTION_FG_IN				1		
O2		0.008594	0.008594	0.008594	0.008594	0.008594
N2		0.711096	0.711096	0.711096	0.711096	0.711096
CO2		0.087725	0.087725	0.087725	0.087725	0.087725
H2O		0.192585	0.192585	0.192585	0.192585	0.192585
Water transferred	lb/h	6.738574	5.331947	8.114353	1.585761	3.666283
Water transferred	%	40.25998	32.4536	49.04392	9.495273	22.00635
Deviation from the ACR		-2.7926	-1.38598	-4.16838	2.360209	0.279686
Condensation rate (kg/s)		0.000849	0.000672	0.001022	0.0002	0.000462

The inlet and working boundary conditions are set similar to the experimental setup for all of the 11 cases. Figure 24 shows the comparison between the numerical results and the experimental ones.

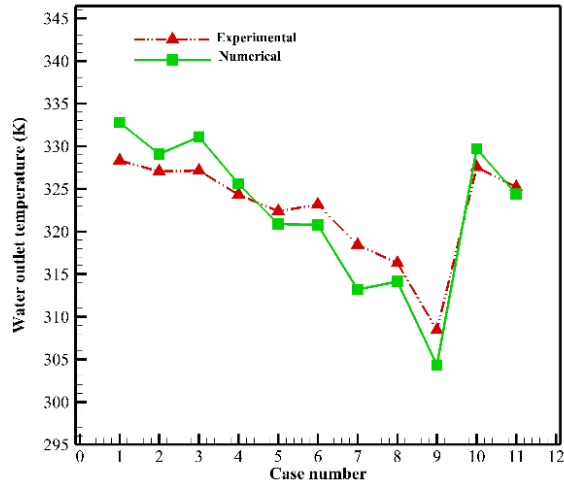
As can be seen in this figure the numerical results obtained using the present model are in an excellent agreement with the experimental results.



a) Condensation rate.



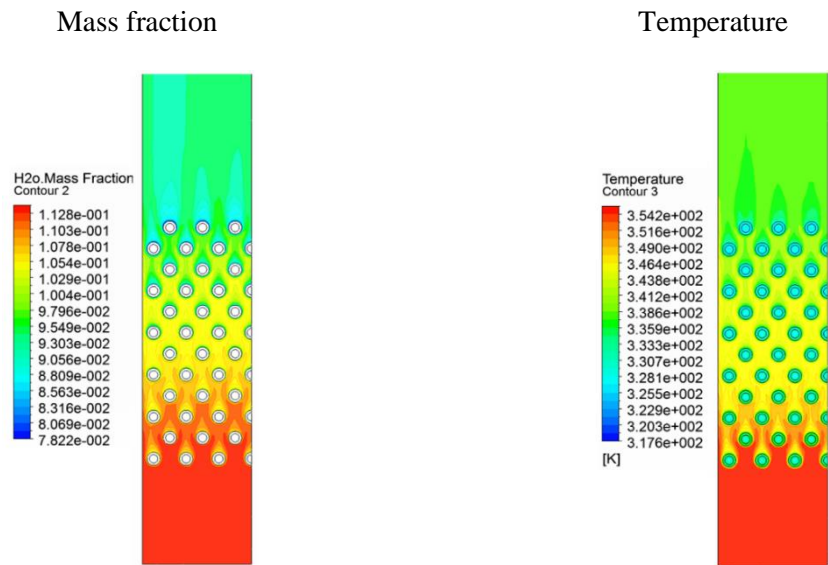
b) Outlet flue-gas temperature.



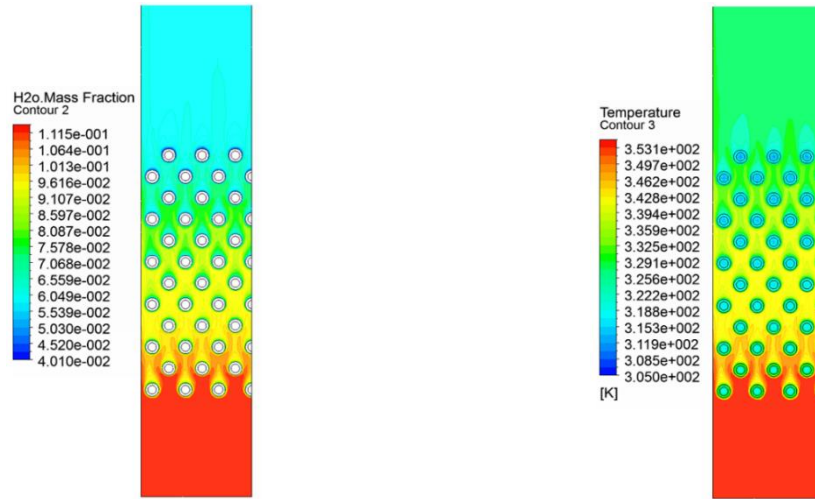
c) Outlet water temperature.

Figure 24. Comparison between the numerical simulation and experimental data.

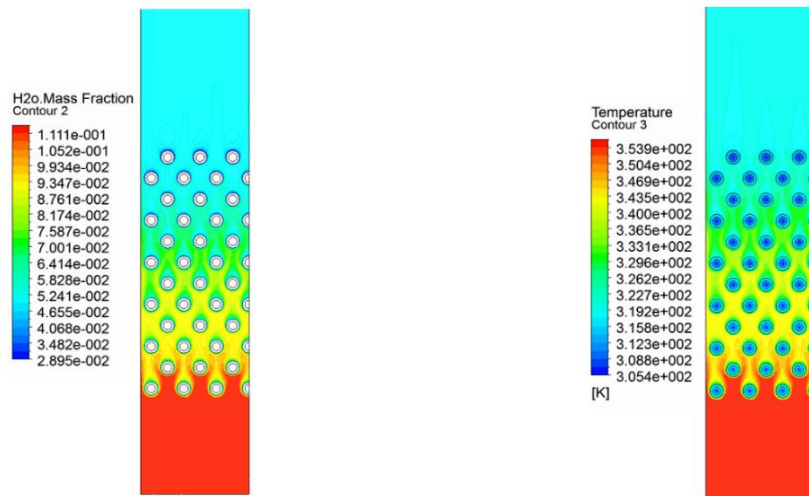
To briefly study the effect of the inlet conditions, the temperature and H₂O mass fraction contours for cases 1, 5 and 9 are shown in Figure 25. As seen in this figure, the water mass fraction along the cross flow TMC heat exchanger decreases as the cooling water temperature decreases (or mass flow rate increases).



a) Case 1



b) Case 5



c) Case 9

Figure 25. Temperature and water vapor mass fraction contours for cases 1, 5 and 9.

Figure 26 shows the deviation of the numerical results from the experimental data regarding condensation rate. As can be seen, the computational condensation rate deviates from the experimental data mainly for the cases with lower condensation rate (higher surface temperature). The deviation of numerical results from the experimental data could be related to the importance of capillary condensation in the cases with higher surface temperature. In the next chapter, the water

vapor mass flux for the capillary condensation will be derived, and the current model will be modified accordingly.

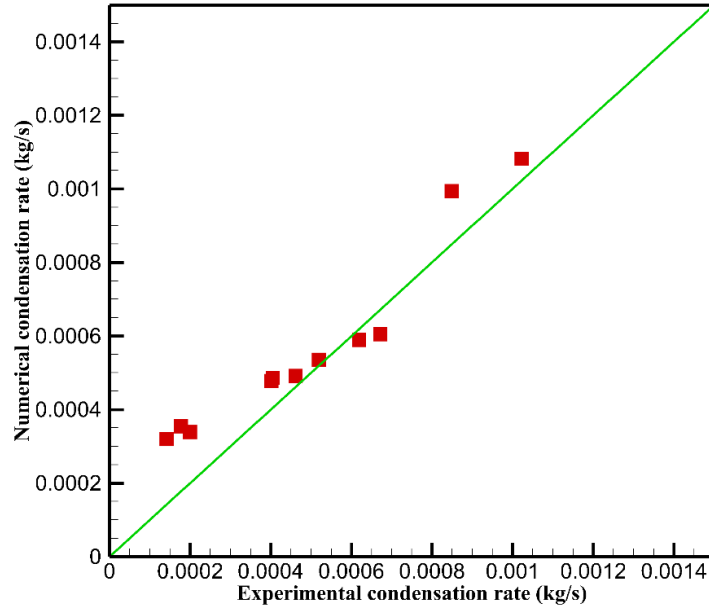


Figure 26. Deviation of numerical prediction from the experimental results.

4. Chapter 4: Mixed condensation model

In chapter 3 a simplified model based on the solid wall condensation with a constant as a correction factor was used for simulation of heat and mass transfer inside a TMC cross-flow heat exchanger. As it has been mentioned in chapter 1, micro and nanoscale phenomena such as capillary condensation and Knudsen flow could have significant effects on the condensation rate over a nanoporous surface. Hence the condensation model for a nanoporous layer needs to consider small-scale transport phenomena and physical properties of the membrane such as pore size and contact angle. In this chapter, a semi-experimental model based on the thermodynamic and transport equations in micro and nanoscale will be developed. The results from this hybrid model which is called Mixed Condensation Model is compared with the available experimental results in this chapter.

1.31. Adsorption and desorption

Adsorption is the process of formation of a thin film of liquid over a surface due to the Van der Waals force between the molecules of the fluid and surface. This process results in capillary condensation phenomena inside nanoporous materials. The reverse phenomena in which the fluid molecules return from the solid surface to the fluid is called desorption. Based on the IUPAC classification of the porous materials, they can be divided into three categories[80]:

- Micropores: pore size (d) < 2 nm
- Mesopores: 2 nm < pore size (d) < 50 nm
- Macropores: 50 nm > pore size (d)

In this chapter, the term nanoporous is used which refers to the size of the pore diameter which is between 6 to 8 nm.

1.32. Transport of an adsorbable gas in nanopores

The porous materials in each category have different adsorption behavior. In micropores, the effect of overlapping surface forces process is more dominant while in the mesopores the capillary forces become more critical in condensation. In the mesopores and macropores, the three essential transport mechanisms are capillary flow, gas-phase flow, and surface flow. The gas flow inside the pores can be categorized based on the Knudsen number:

$$Kn = \frac{\lambda}{d} \quad (113)$$

where λ is the mean free path of the vapor and d is the pore size. The following regimes based on the Kn can be classified as:

- Viscous flow $Kn \ll 1$
- Knudsen flow $Kn \gg 1$
- Transition flow $Kn = 1$

Viscous flow of the gas phase

For the ($Kn \ll 1$) the viscous flow is the dominant transport mechanism of gas inside nanopores, and the driven force is the pressure gradient. For laminar flow the molar flux J is governed by Hagen-Poiseuille equation:

$$J_v = \frac{\varepsilon r^2 p}{8\tau\mu RT} \frac{dp}{dz} \quad (\text{mol m}^{-2}\text{s}^{-1}) \quad (114)$$

Where ε , τ , and μ are the porosity, tortuosity factor, and gas viscosity, respectively. The permeability across the porous medium is:

$$B_v = \frac{J_v}{(\Delta P/L)} \frac{dp}{dz} = \frac{\varepsilon r^2}{8\tau\mu RT} P_m \quad (\text{mol m}^{-1}\text{s}^{-1}\text{Pa}^{-1}) \quad (115)$$

where the P_m is the mean pressure of the inlet P_1 and outlet pressures P_2 respectively.

Knudsen flow of the gas phase

Knudsen diffusion which is the transport of fluid due to the collision of fluid molecules with the wall of porous media. Knudsen diffusion occurs when the Knudsen number ($Kn \gg 1$) and fluid molecules-wall collisions are dominant. The molar flux regarding Knudsen equation can be written as:

$$J_{\kappa} = \frac{2}{3} \frac{\varepsilon r}{\tau} \left(\frac{8}{\pi RTM} \right)^{0.5} \frac{dp}{dz} \quad (116)$$

By integrating the above equation, the permeability can be obtained as:

$$B_{\kappa} = \frac{J_{\kappa}}{\Delta P/L} = \frac{2}{3} \frac{\varepsilon r}{\tau} \left(\frac{8}{\pi RTM} \right)^{0.5} \quad (117)$$

The Knudsen permeability is independent of pressure, while the viscous flow is linearly dependent on pressure.

Transition Flow in the Gas Phase

When the pore diameter and the mean free path of vapor molecules are in the same order ($Kn \approx 1$), both Knudsen and viscous diffusion mechanisms are important. This gas transport regime is known as transition flow, and the total molar flux can be obtained as:

$$J_t = J_v + J_{\kappa} = \frac{\varepsilon r^2 p}{8\tau\mu RT} \frac{\Delta P}{L} + \frac{2}{3} \frac{\varepsilon r}{\tau} \left(\frac{8}{\pi RTM} \right)^{0.5} \frac{\Delta P}{L} \quad (118)$$

The permeability of the transition flow is:

$$P_t = J_t / (\Delta P/L) \quad (119)$$

1.33. Flow in the Capillary Condensate

The capillary condensation happens at vapor pressure lower than the saturated pressure of liquid due to high van der Waals force inside the nanoporous medium. The difference between capillary condensation and condensation on a solid wall is shown in Figure 27. Inside a pore, the vapor molecule (adsorptive) experiences the van der Waals forces from all directions which reduce the adsorption energy required for the condensation process and the vapor condenses at a lower pressure than the saturated pressure of the pure liquid.

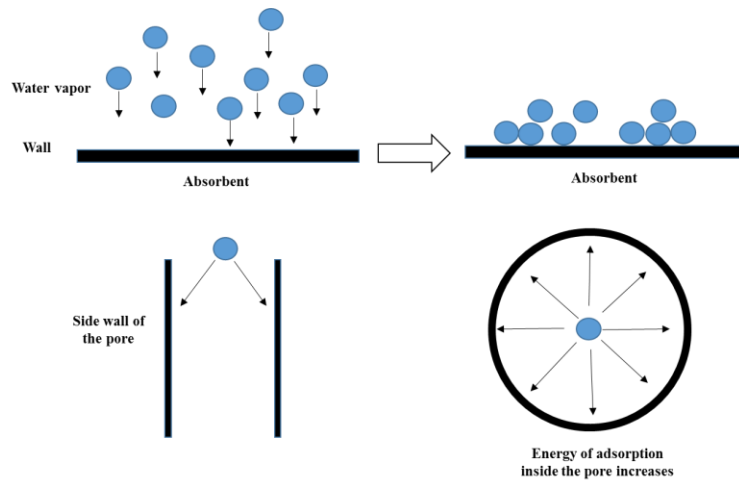


Figure 27. Adsorption and capillary condensation [80]

Capillary action

The capillary action is the rise of liquids inside a capillary tube when the tube is partially immersed in a liquid. The capillary action and the top curved boundary (meniscus) of liquid which is raised inside the capillary tube are the results of adhesive forces (attractive forces between unlike molecules), cohesive forces (intermolecular forces) and surface tension. The free surface of the liquid in a capillary tube is under the effect of both adhesion and downward cohesion forces. The imbalance of the effective forces on the free surface of the liquid causes the surface tension. The upward component of the surface tension results in the upward or downward pull of liquid inside

the capillary tube and the height of liquid column inside the capillaries depends on the weight of the liquid and the surface tension value.

Capillary pressure

The pressure difference across the meniscus between two immiscible fluids is called capillary pressure (See Figure 28).

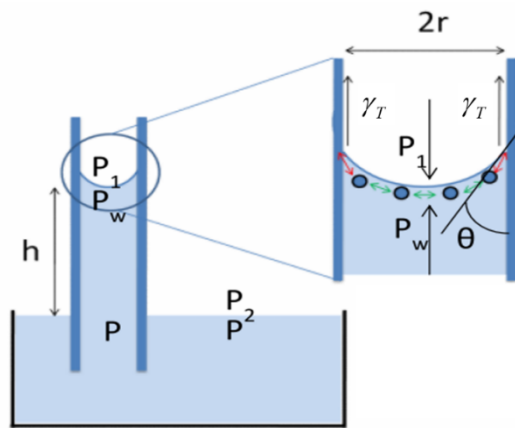


Figure 28. Capillary action and the pressure at different points [80].

The capillary pressure can be obtained from the balance of forces acting on the meniscus:

$$P_1(\pi r^2) = P_w(\pi r^2) + \gamma_T(2\pi r) \quad (120)$$

where T is the vertical component of surface tension γ . The capillary pressure is the pressure difference across the free surface:

$$P_c = P_1 - P_w = \frac{2\gamma_T}{r}(\pi r^2) = \frac{2\gamma \cos \theta}{r} \quad (121)$$

This above equation is known as Law of Laplace [75].

Kelvin Equation

This equation describes the higher vapor pressure of a curve interface between two immiscible fluid compared to a non-curved interface. Kelvin equation correlates the pore size (pore radius) and capillary condensation pressure [80].

$$\ln\left(\frac{P^*}{P_0}\right) = -\frac{2\gamma V \cos \theta}{RT r_m} \quad (122)$$

where P_0 is the saturated vapor pressure on a planner interface, P^* is the capillary condensation pressure, γ is the interfacial tension, r_m is the radius of the cylindrical capillary, V is the liquid molar volume, and θ is the contact angle, R is the ideal gas constant, and T is temperature. The Kelvin equation indicates that for a pore with a mean capillary radius of r_m when the contact angle θ is less than 90° the condensation occurs if the vapor pressure is higher than the capillary condensation pressure inside the nanopore.

1.34. Modeling of condensation in TMC heat exchangers

Although the transport of an adsorbable gas has been studied extensively, still different aspects of this phenomena are under investigation in many industries. Following are the most important shortcomings of the previous works which we will be address in the next sections:

- 1- The previous models are based on the zero or one-dimensional analysis of condensation phenomena inside nanoporous layers and could not be used for industrial application.
- 2- In the previous studies on the condensation over and inside nanoporous layers effect of noncondensable gases has not been studied, and the condensation process has been studied for a single species.

The modeling part of this project is divided into three main part:

- 1) Condensation of condensable gas over and inside the nanoporous layers.
- 2) Transport process and heat transfer inside the Flue-gas and cooling water domains including the species transport and heat transfer.
- 3) Heat transfer and fluid flow inside the porous wall of the TMC tubes.

1.35. Condensation of condensable gas over and inside the nanoporous layers

Previous research has shown that the dominant mechanism for the condensation on the outer side of a TMC tube is the capillary condensation [16]. In this section, the mass flux for the water vapor transport is derived for the general form in which the nanoporous layer is partially-filled with water. But as it has been discussed by Abeles et al. [81], the nanoporous layer will be filled by water as long as the outside pressure of the water vapor is equal or higher than the capillary pressure at the working condition. Hence in heat and water recovery of application of TMC tubes from the flue gas, the primary condensation mechanism will be the capillary condensation and this model will be used to modify the solid wall condensation model in chapter 3. In the present study, the following simplifications have been done in the derivation of the condensation rate and water flow rate over and inside the nanoporous layers:

- 1- In the Kelvin equations, the effect of statistical film thickness (t) has not been considered.
- 2- The model cannot capture the condensation/evaporation hysteresis since r_m is constant in this study. Variation of r_m could be significant for more sensitive and unsteady applications such as in sensor manufacturing industries.

The effect of the geometrical configuration of the nano-porous layer on the transport of water can be considered by considering the tortuosity of the porous layer. But in this study, the nanoporous layers are assumed to be made of straight nanopores. Figure 29 shows a partial field nanopore layer.

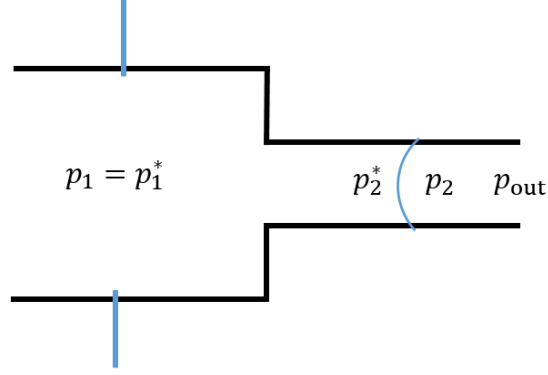


Figure 29. Pressure condition for in a multilayer pore configuration with one meniscus.

P_2^* and P_2 in Figure 29 are the pressure at each side of the liquid interface and P_{out} is the pressure of the flue-gas passing over the TMC tubes. We assume that the contact angles on both sides of the nanopore are the same. For a capillary nanopore the law of Laplace is:

$$P_1^* = P_1 - \frac{2\sigma \cos(\theta)}{r_1} \quad (123)$$

$$P_2^* = P_2 - \frac{2\sigma \cos(\theta)}{r_2} \quad (124)$$

And the Kelvin equation:

$$P_1^* = P_1 + \left(\frac{\rho_l RT}{M} \right) \ln(P_1/P_0) \quad (125)$$

$$P_2^* = P_2 + \left(\frac{\rho_l RT}{M} \right) \ln(P_2/P_0) \quad (126)$$

From Kelvin equation:

$$\Delta P = P_1^* - P_2^* = (P_1 - P_2) + \left(\frac{\rho_l RT}{M} \right) \text{Ln}(P_1/P_2) \quad (127)$$

$$\text{Ln}(P_1/P_2) = \text{Ln}\left(\frac{P_1/P_m}{P_2/P_m}\right) = \text{Ln}\left(\frac{1+(P_1-P_m)/P_m}{1+(P_2-P_m)/P_m}\right) = \text{Ln}\left(1+(P_1-P_m)/P_m\right) - \text{Ln}\left(1+(P_2-P_m)/P_m\right) \quad (128)$$

From truncated Taylor series of logarithm, we have:

$$\text{Ln}\left(1+(P_1-P_m)/P_m\right) - \text{Ln}\left(1+(P_2-P_m)/P_m\right) = (P_1-P_m)/P_m - (P_2-P_m)/P_m = (P_1-P_2)/P_m \quad (129)$$

$$\Delta P = (P_1 - P_2) + \left(\frac{\rho_l RT}{M} \right) \frac{(P_1 - P_2)}{P_m} = (P_1 - P_2) \left[1 + \frac{\rho_l RT}{MP_m} \right] \quad (130)$$

We assume the total length of nanopore is L and the length of portion filled by liquid x . The flux in the liquid filled part of the nanopore [82]:

$$J_{cap} = \frac{\rho_l \varepsilon r^2 \Delta P}{\tau M 8 \mu_l x} \quad (131)$$

By defining the diffusion flux coefficient in the liquid-filled part:

$$D_{cap} = \frac{\rho_l RT}{\tau M} \left(\frac{r^2}{8 \mu_l} \right) \left[1 + \frac{\rho_l RT}{P_m} \right] \quad (132)$$

Then the flux will be:

$$J_{cap} = \frac{D_{cap}}{x/\varepsilon} \frac{(P_1 - P_2)}{RT} \quad (133)$$

where ε is the porosity, τ is the tortuosity, T is temperature, r is the pore size, M is the molecular weight, R is the gas constant. μ_l and ρ_l are the viscosity and density of the condensed liquid and $P_m = 0.5 \times (P_1 + P_2)$ is the average value of the pressure on both sides of the porous layer.

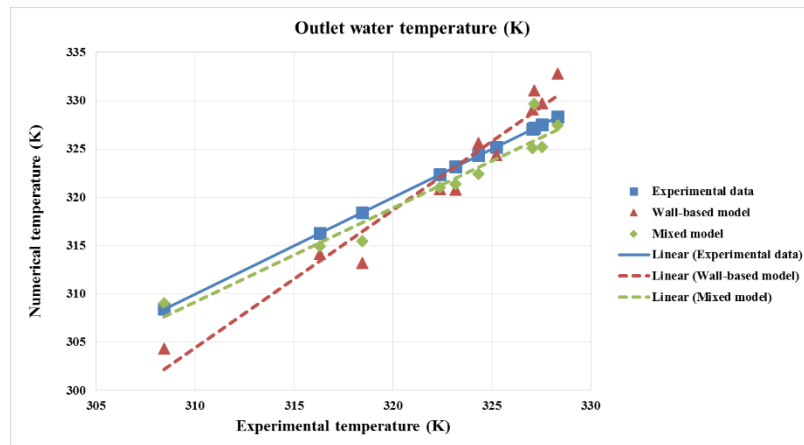
Modified condensation model (Mixed model)

As it was mentioned before, the micro-scale condensation model in this study is the capillary condensation. The experimental data also showed that the condensation rate decrease as the average wall temperature of the TMC tubes decreases. Based on the above point the modified condensation rate has been proposed:

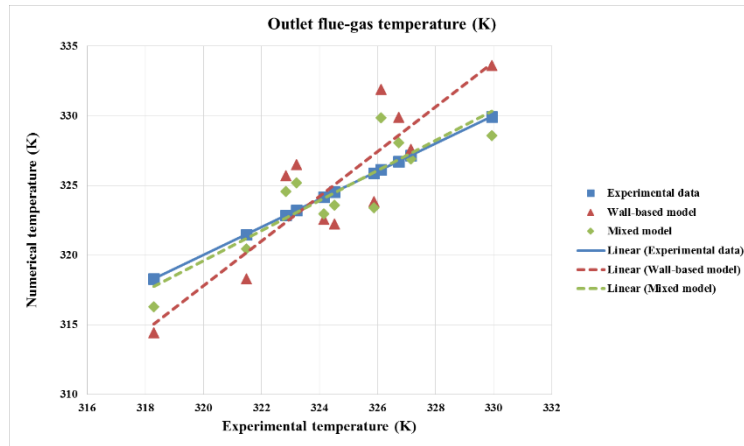
$$J_{Mix} = \frac{(T_{max} - T_{wall})}{(T_{max} - T_{min})} J_{WC} + J_{cap} \quad (134)$$

where J_{Mix} is the new condensation rate, T_{max} and T_{min} are the maximum and minimum temperature in the domain, T_{wall} is the TMC wall temperature, J_{cap} is the capillary condensation rate and J_{WC} is the modified condensation rate on the solid wall obtained in the previous chapter. The proposed condensation model has been applied into the numerical setup by using the condensation rate and UDFs.

Figure 30 shows the comparison between the results obtained by the solid-wall based and mixed condensation models with the experimental results [25]. As can be seen, the mixed model can predict the outlet cooling water and flue-gas temperatures more accurately.



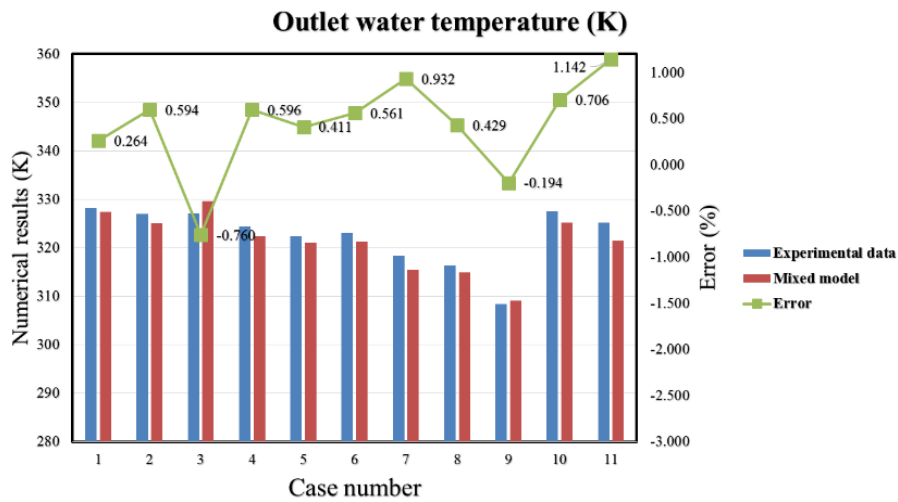
(a)



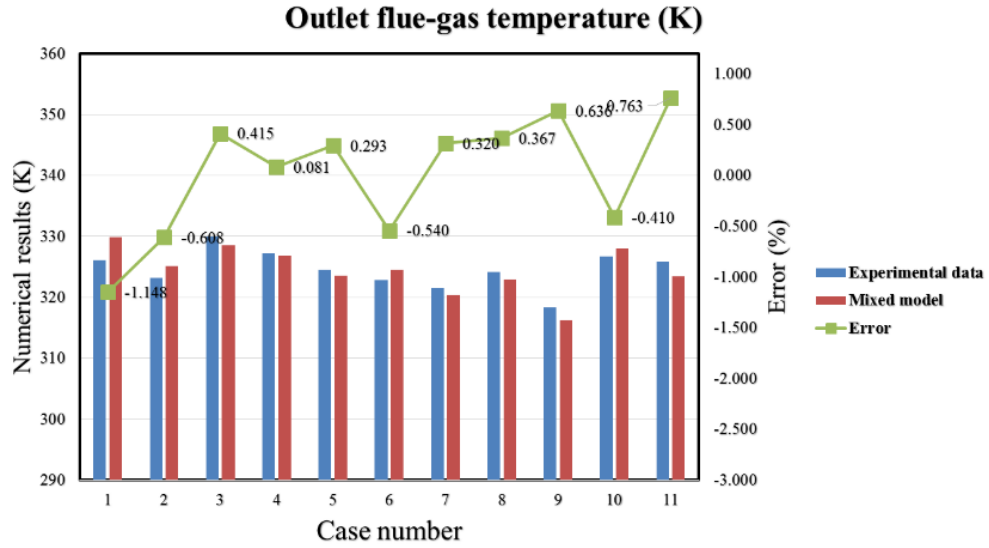
(b)

Figure 30. Comparison of numerical simulation results with the experimental data [25].

Figure 31 also shows the deviation of the results obtained by the mixed model and the experimental results.



(a)



(b)

Figure 31. Comparison between the results of the mixed model with the experimental data.

In the next chapter, a parametric study of the TMC heat exchanger will be presented using the mixed model. Optimization of TMC cross-flow heat exchanger will be addressed. For the numerical simulation of the TMC heat exchanger and the optimization process, the proposed mixed model will be used.

5. Chapter 5: Parametric Study of Optimum Performance

1.36. Parametric study of a cross-flow TMC heat exchanger

The effects of different inlet parameters and working conditions on the performance of the cross-flow TMC heat exchangers are investigated in this chapter. In the TMC crossflow heat exchanger, the water vapor transfers from the flue-gas flow to the cooling water through the TMC tubes. The total heat transfer in the heat exchanger module has two parts: the latent heat of condensation and the sensible heat in the form of convective heat transfer. The condensation rate can be calculated as:

$$\Delta \dot{m}_{cond} = \dot{m}_{fg,in} - \dot{m}_{fg,out} = \dot{m}_{w,in} - \dot{m}_{w,out} \quad (135)$$

where $\dot{m}_{fg,in}$, $\dot{m}_{fg,out}$, $\dot{m}_{w,in}$ and $\dot{m}_{w,out}$ are the inlet and outlet flow rate of the flue-gas and cooling water, respectively. The condensing water flux can be expressed as:

$$J_{cond} = \Delta \dot{m}_{cond} = (\dot{m}_{fg,in} - \dot{m}_{fg,out}) / A_o \quad (136)$$

where A_o is the outer surface of the TMC tubes. The water recovery efficiency is defined as:

$$\eta_{cond} = (\dot{m}_{fg,in} - \dot{m}_{fg,out}) / \dot{m}_{s,in} \times 100, \quad \dot{m}_{s,in} = \dot{m}_{fg,in} \times Y_{s,in} \quad (137)$$

where $\dot{m}_{s,in}$ is the water vapor inlet mass flow rate, and $Y_{s,in}$ is the water vapor mass fraction.

The total amount of the recovered heat can be obtained using the following equation:

$$q_T = (\dot{m}_{w,in} h_{w,in} - \dot{m}_{w,out} h_{w,out}) = (\dot{m}_{fg,in} h_{fg,in} - \dot{m}_{fg,out} h_{fg,out}) + \Delta \dot{m}_{cond} h_{fg} \quad (138)$$

where $h_{w,in}$ and $h_{w,out}$ are the inlet and outlet enthalpy of the cooling water, and h_{fg} is the latent heat of condensation of water. The latent heat of condensation (Q_L) and the sensible/convective (Q_S) heat transfer can be obtained as follow:

$$q_L = \Delta \dot{m}_{cond} h_{fg}, \quad q_S = q_T - q_L \quad (139)$$

and the thermal efficiency of the heat exchanger can be calculated by using the following equation:

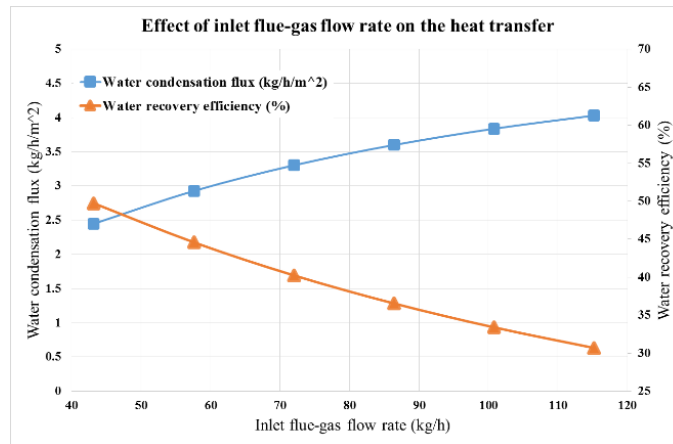
$$\eta_{TH} = (q_T / q_{max}) \times 100, \quad q_{max} = \dot{m}_{fg,in} \times c_{fg,in} \times T_{fg,in} \quad (140)$$

where q_{in} is the total heat flow rate of the inlet flue-gas stream and $c_{fg,in}$ is the heat capacity of the inlet flue-gas.

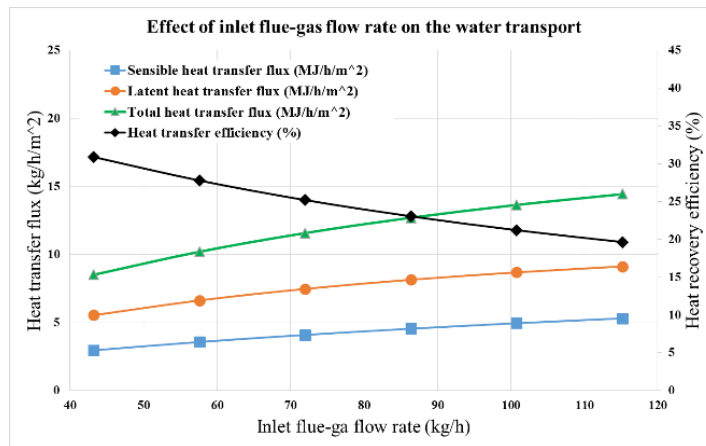
1.37. Effect of inlet flue-gas flow rate

Impact of the inlet flue-gas flow rate on the water transport and heat transfer are shown in Figure 32. The results are obtained for the inlet water vapor mass fraction 0.114, water mass flow rate of 54 kg/hr, and inlet flue-gas and water temperatures 350 K° and 300 K° respectively. As seen in figure 4(a), by increasing the flow rate of the inlet flue gas the water recovery for the TMC heat exchanger increases while the water recovery efficiency decreases adversely.

High condensation rate at high flue-gas flow rate is apparently because of higher feed water vapor in the TMC heat exchanger while the higher water recovery efficiency for the low flue-gas flow rate can be associated to the longer residence time of fluid in the heat exchanger. Figure 32(b) shows the effect of inlet flue-gas flow rate on the heat transfer flux and heat recovery efficiency. The figure shows that the sensible, latent and consequently the total heat flux rates increase as the flue-gas flow rate increases, but the heat transfer recovery efficiency decreases. As the inlet, the flue-gas flow rate increases the residence time becomes shorter and smaller portion of the total inlet flow rate transfers to the water inside the TMC tubes. The increase in the latent and sensible heat transfer is also because of the increase in the condensation rate and convective heat transfer coefficient at a higher mass flow rate of the feed flue-gas.



a) Variation of condensation rate and water recovery efficiency.



(b) Variation of heat transfer flux and heat recovery efficiency

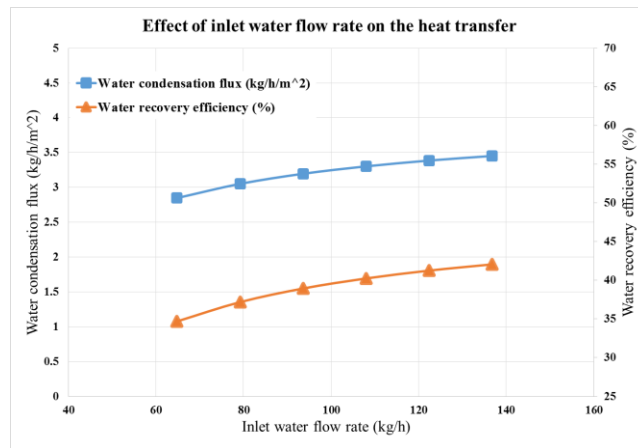
Figure 32. Effect of inlet conditions on the performance of TMC unit.

1.38. Effect of inlet water flow rate

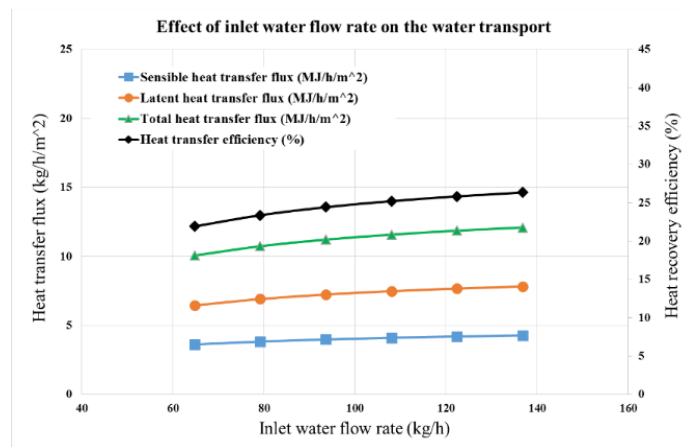
Figure 33 (a) and (b) show the effects of the inlet water flow rate on the overall water transport and heat transfer in the TMC heat exchanger. The inlet boundary conditions for the flue-gas and water are kept constant as it was mentioned previously. As seen in Figure 33 (a), both water condensation flux and water recovery efficiency increase as the inlet water flow rate increases. Since the flue-gas flow rate is fixed at 72 kg/hr, the residence time for the flue-gas stream is constant. Furthermore,

the increase in the water flow rate decreases the surface temperature of the TMC tubes which enhances the water condensation flux and water recovery efficiency.

Figure 33 (b) shows the variation of heat transfer fluxes and heat recovery efficiency with the inlet water flow rate. As it is expected the latent and sensible heat transfer fluxes increase with the increase of water flow rate due to the increase in the water condensation rate and the temperature difference between the cold and hot flow streams. The heat recovery efficiency also increases in Figure 33 (b) as the total heat transfer grows and the residence time remains constant.



a) Variation of condensation rate and water recovery efficiency.



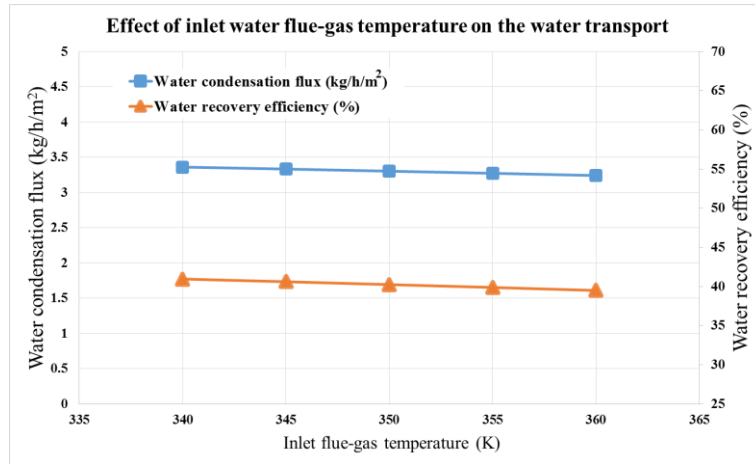
b) Variation of heat transfer flux and heat recovery efficiency

Figure 33. Effect of inlet water flow rate on the water and heat recovery efficiency

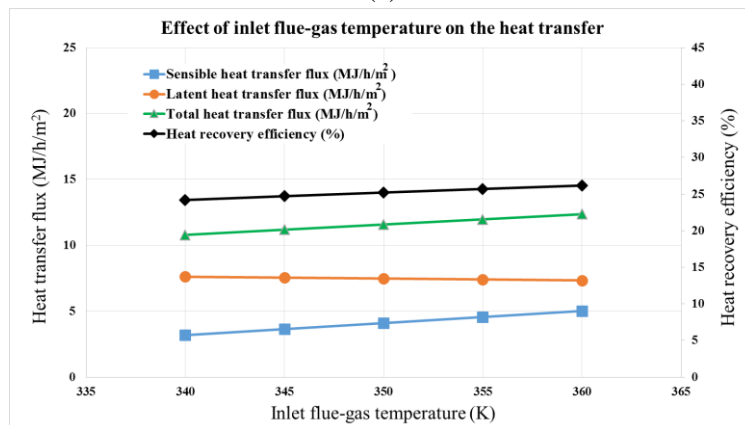
1.39. Effect of inlet flue-gas temperature

Figure 34 shows the effect of inlet flue-gas temperature on the water and heat recovery in a TMC heat exchanger. As seen, by increasing the inlet flue-gas temperature the condensation rate and water recovery slightly decreases while the total heat transfer flux and heat recovery increased.

Increasing the flue-gas temperature results in an increase of the TMC surface temperature and a decrease of the condensation rate. On the other hand, the temperature difference between the hot and cold flow stream increase which leads to a higher sensible heat transfer rate and heat recovery efficiency.



(a)

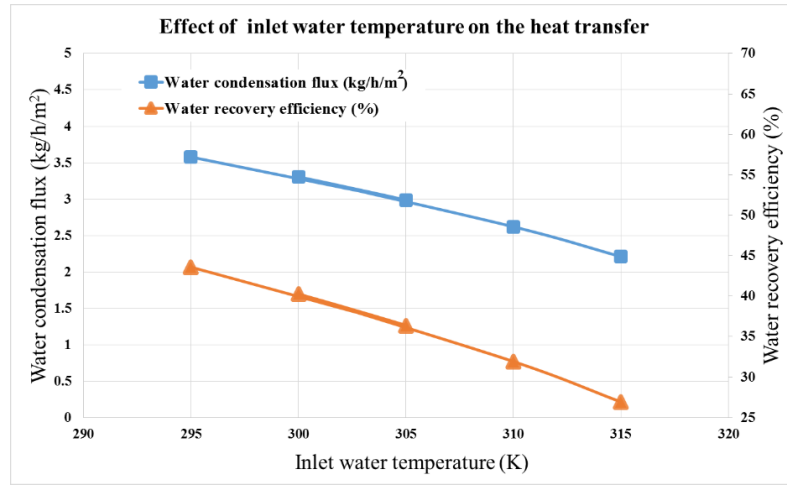


(b)

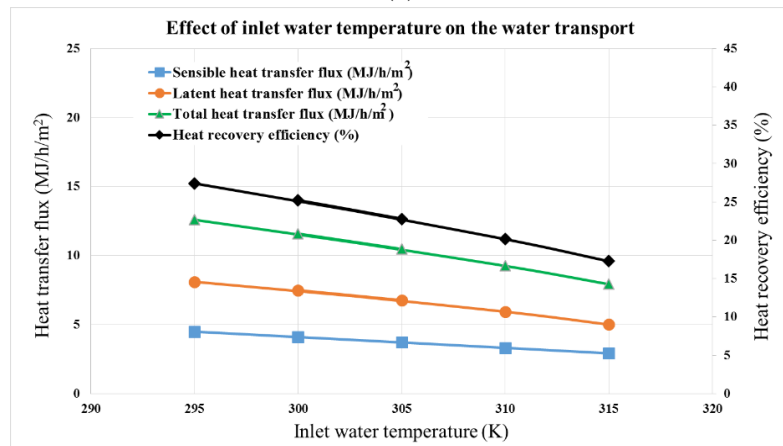
Figure 34. Effect of inlet flue-gas temperature on the water and heat recovery efficiency.

1.40. Effect of inlet water temperature

Figure 35 shows the effect of inlet water temperature on the water and heat recovery in a TMC heat exchanger. The graph shows that increasing the water temperature decreases water and heat transfer rates and efficiencies. As the inlet cooling water temperature increases, both condensation and latent heat decrease. Increasing the TMC surface temperature decreases the condensation rate and the latent heat of condensation. Also with increasing the inlet water temperature, the temperature difference between the flue-gas and water streams decreases and as a result the sensible heat transfer rate decreases.



(a)



(b)

Figure 35. Effect of inlet water temperature on the water and heat recovery efficiency.

1.41. Effect of inlet flue-gas relative humidity

The relative humidity of the flue-gas at the inlet and outlet condition of the TMC heat exchangers are calculated based on the mass fraction of different species [83]:

$$RH = \frac{P_{H_2O}}{VP_{H_2O}(T)} \quad (141)$$

where RH is the relative humidity of the flue-gas P_{H_2O} is the partial pressure off the water vapor and $VP_{H_2O}(T)$ is the vapor pressure of the water at a specific temperature and can be obtained using Antoine's equation:

$$VP_{H_2O}(T) = 133.32 \times 10^{\left[A - \frac{B}{C+T(^{\circ}C)} \right]} \quad (Pa) \quad (142)$$

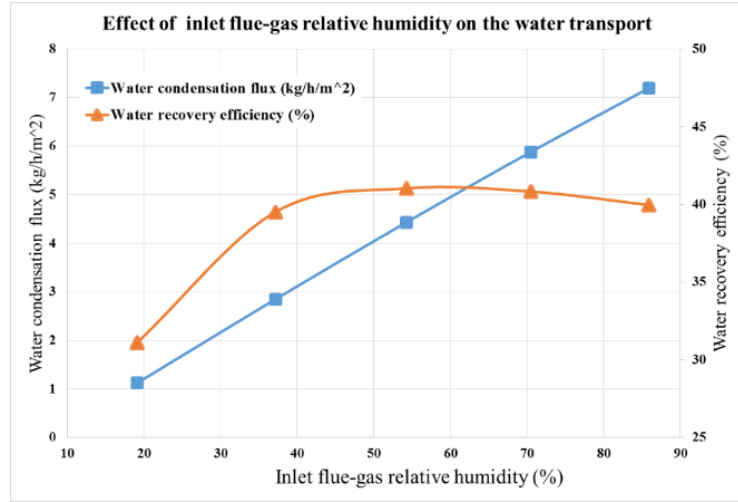
where the consistent numbers A, B, and C are 8.07,1730.6 and 233.4 respectively. The partial pressure of the water vapor can be obtained as:

$$P_{H_2O} = MF_{H_2O} \times P_{total} \quad (143)$$

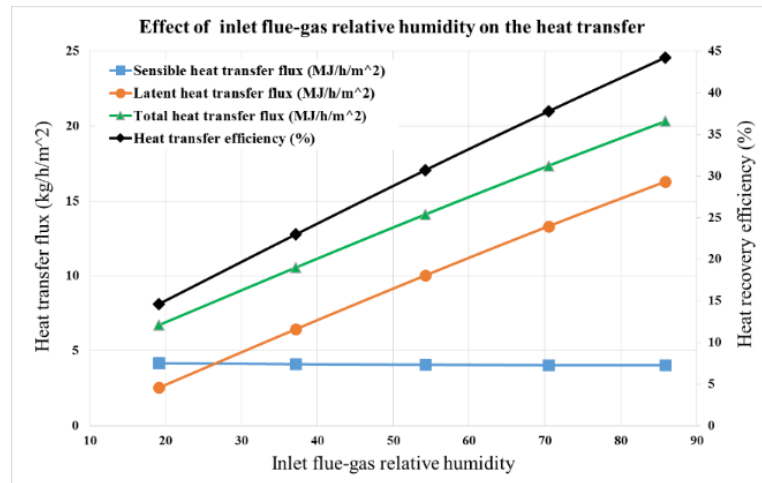
where MF_{H_2O} and P_{total} are the mole fraction of the water and total pressure of the flue-gas, respectively. The mole fraction of the water has been obtained based on the mass fraction of the water vapor calculated in by the developed algorithm in Ansys Fluent.

Figure 36(a) and (b) show the effects of inlet relative humidity on the water and heat transfer rate inside the TMC heat exchanger. As can be seen in Figure 36 (a) the water condensation flux increases as the relative humidity increases while the water recovery efficiency increases at the beginning and then slightly decreases. The higher relative humidity of the feed glue-gas the more inlet water vapor and the higher condensation flux. Figure 36 (a) also shows that the water recovery efficiency increases rapidly with the increase of relative humidity and then levels off at the relative

humidity of around 50%. From this figure, it appears that by the rise in relative humidity the water vapor mass fraction gradient near the TMC walls, which is the driving force for the water vapor transfer outside of the TMC tube, does not change significantly. Figure 36 (b) shows that the total heat and latent heat fluxes increase as the relative humidity of the inlet flue-gas increases. But the convective heat transfer flux remains almost constant with the increase inlet relative humidity.



a) Variation of condensation rate and water recovery efficiency.

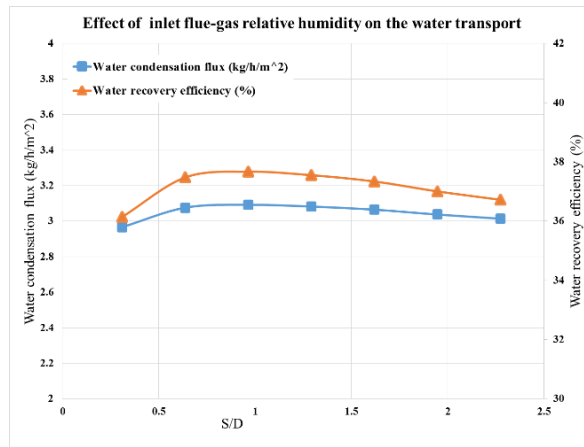


b) Variation of heat transfer flux and heat recovery efficiency

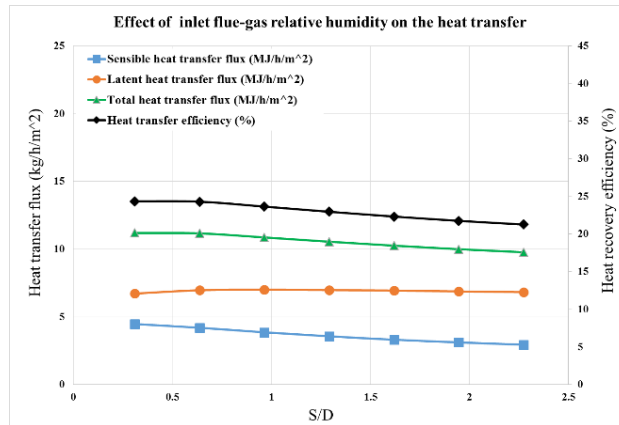
Figure 36. Effect of flue-gas relative humidity on the water and heat recovery efficiency.

1.42. Effect of tube pitch

Variation of the total water and heat transfer with the tube pitches for a 45-degree arrangement of the bundled tube is shown in Figure 37 (a) and (b). In the figures, S is the diagonal pitches of the tubes and D is the outer diameter of the TMC tubes. As seen in Figure 37 (a), the water condensation rate and the water recovery efficiency increase by the increase of pitches at the beginning and then decreases continuously. Similar trend for the total heat transfer and the heat the recovery efficiency can be seen in Figure 37 (b).



a) Variation of condensation rate and water recovery efficiency.



b) Variation of heat transfer flux and heat recovery efficiency

Figure 37. Effect of tube pitch on the water and heat recovery efficiency.

1.43. Tube pitch effect on the TMC volumetric heat transfer

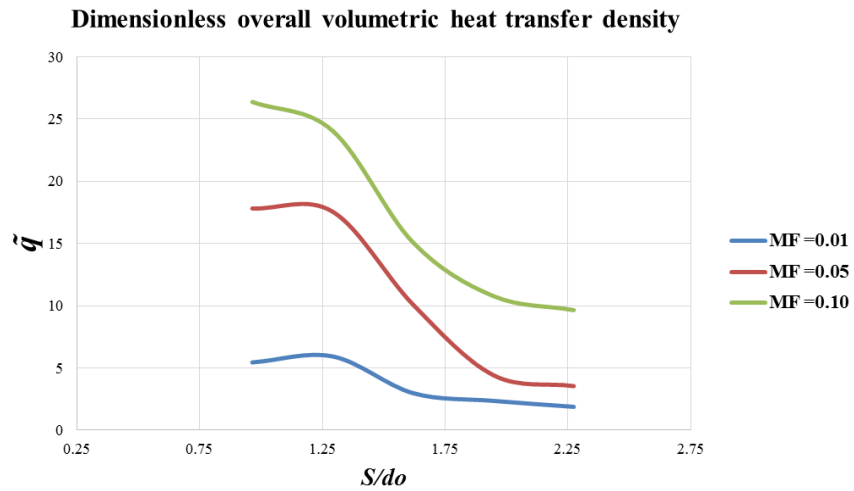
To study the impact of tube pitch and water vapor content of the flue gas on the volumetric heat transfer inside the TMC heat exchanger, a new series of simulations have been carried out for the constant inlet flue-gas velocity of 0.5 m/s and water inlet velocity 0.015 m/s. The inlet mass fraction (MF) of the flue-gas was set to 0.04 for O_2 , 0.09 for CO_2 and $1-MF_{O_2}-MF_{CO_2}-MF_{H_2O}$ for the N_2 mass fraction. The inlet mass fraction of water vapor was changed between 0.01 to 0.1. The inlet temperature of the flue-gas and cooling water were 350 K and 300 K, respectively. To evaluate the effect of different tube arrangements on the performance of the TMC heat exchangers, the dimensionless space between the tubes (S/d_o) was also varied. The dimensionless overall volumetric heat transfer density for the TMC heat exchanger was defined as:

$$q = \frac{q/(T_{fg,in} - T_{w,in})}{kLHW/(d_o)} \quad (144)$$

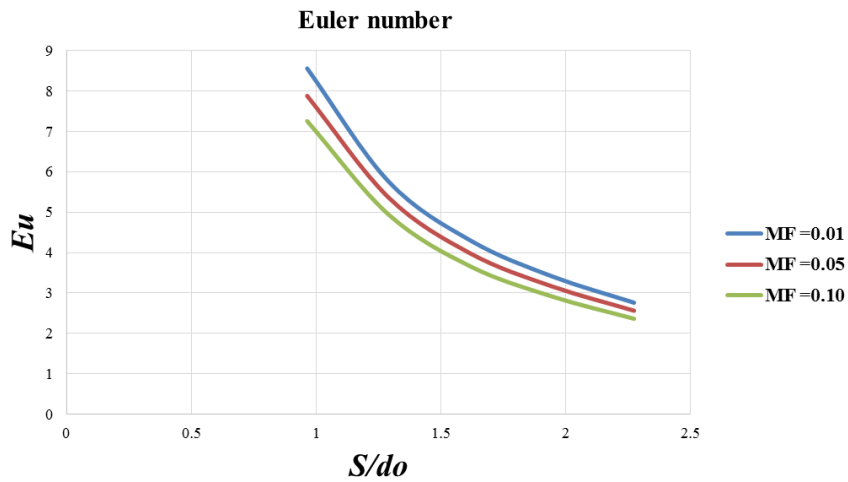
where q is the total heat transfer between the flue-gas stream and the cooling water, $T_{fg,in}$ and $T_{w,in}$ are the inlet flue-gas and cooling water temperatures, respectively. LHW gives the total volume of the heat exchanger, k is the flue-gas thermal conductivity of W/(m K), and d_o is the outer diameter of the TMC tubes.

Figure 38 (a) shows the effect of an inlet water vapor mass fraction of the flue gas and dimensionless space between the tubes on the dimensionless overall volumetric heat transfer density. As can be seen, the volumetric heat transfer density increases noticeably with an increase of inlet water vapor mass fraction. With the increase of the water vapor mass fraction, the condensation rate increases, which leads to the increase of latent and overall heat transfer rate between the flue-gas and the cooling water (Q). Figure 38 also shows that volumetric heat transfer

density decreases with increasing the dimensionless distance between the tubes. With the increase of the dimensionless tube distance, the increase in the volume of the TMC heat exchanger will be more dominant compared to the change in the heat transfer rate which decreases the volumetric heat transfer density.



(a)



(b)

Figure 38. Effect of inlet humidity and tubes pitch on the heat transfer and Euler number.

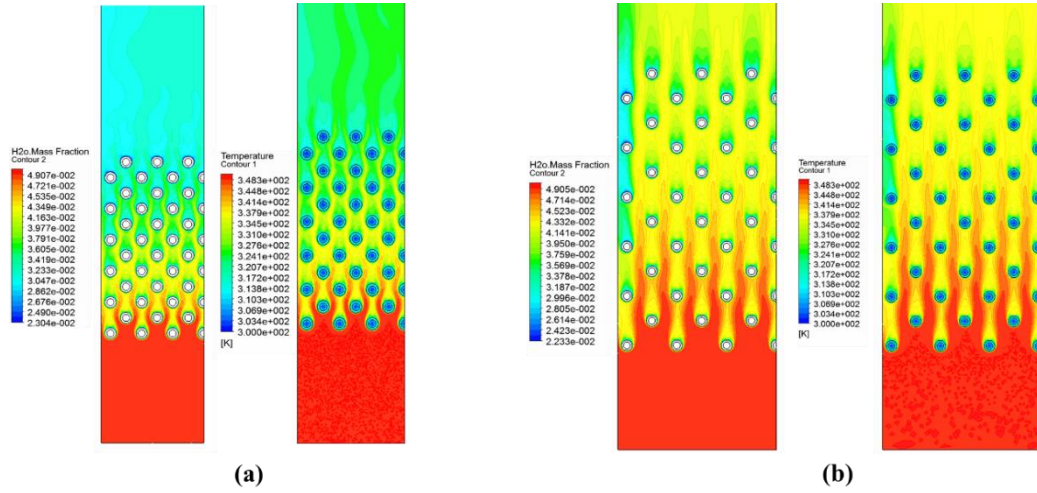
The graph of volumetric heat transfer density has an optimum value ($S/d_o \approx 1.2$), as can be seen in Figure 38 for lower values of the inlet water vapor mass fraction. Contrary, the graph shows that q continuously decreases as the dimensionless distance between the tubes increases for higher values of the inlet water vapor mass fraction. For the larger amount of the inlet mass fraction ($MF=0.1$), the latent heat of condensation is more dominant compared to the convective heat transfer hence and effect of the flow structure and tube distance on q will be less critical.

The static pressure drop along the TMC heat exchanger is defined as $\Delta P = P_{in,FG} - P_{out,FG}$. Based on the pressure drop, the Euler number can be defined as:

$$Eu = \frac{\Delta P}{\rho_{in,FG} (U_{in,FG})^2} \quad (145)$$

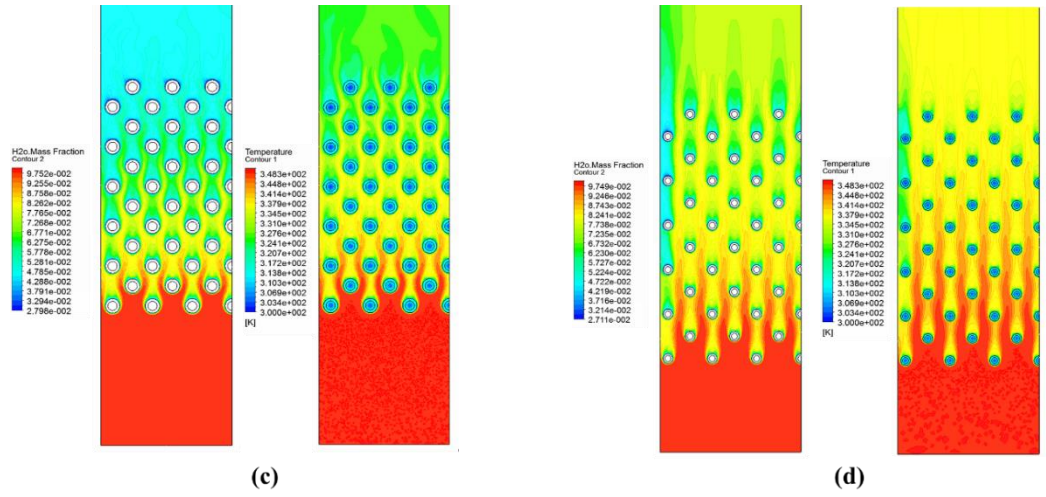
where $\rho_{in,FG}$ and $U_{in,FG}$ are the inlet flue-gas density and velocity. Effect of inlet water vapor mass fraction and dimensionless space between the tubes on Eu is shown in Figure 38 b. As seen in this figure the Euler number decreases with the increase of the inlet water vapor mass fraction and the dimensionless tube distance. The higher inlet mass fraction results in, the higher condensation rate and hence more water transfer from the flue gas stream into the cooling water stream and more pressure drop in the flue-gas side.

Figure 39 shows the effects of tube spacing and the inlet mass fraction on the temperature distribution and water vapor mass fraction inside the TMC heat exchangers. As seen with an increase of the tube spacing, the water vapor mass fraction remains considerably high toward the outlet of the TMC heat exchanger. The figure also shows that the cooling water temperatures inside the TMC tubes increase with the increase of the inlet vapor mass fraction and a decrease of the tube spacing which increase the overall heat transfer from the flue-gas stream to the cooling water.



a) $MF=0.05, S/d_o = 0.965$

b) $MF=0.05, S/d_o = 2.27$



c) $MF=0.10, S/d_o = 0.965$

d) $MF=0.10, S/d_o = 2.27$

Figure 39. Effect of tube spacing and humidity on temperature and vapor mass fraction.

6. Chapter 6: Waste heat and water recovery from pressurized oxy-coal systems

1.44. Pressurized oxy-coal combustion

The pressurized oxy-coal combustion system has been developed to provide a higher efficiency compared to the conventional oxy-coal boilers. The exhaust flow gas from an oxy-coal boiler has a high pressure, temperature and water vapor content which is a perfect working condition for a TMC heat exchanger unit. Gas Technology Institute in collaboration with Media & Process Technology, Florida International University, and SmartBurn LLC [27] has designed and developed a TMC based shell and tube heat exchanger which is capable of recovering heat and water from the exhaust flow from an oxy-combustion burner.

Application of TMC heat exchangers in oxy-coal combustion provides the following advantages[84]:

- 1- Latent heat recovery can increase the efficiency of pressurized oxy-coal boiler up to 14%.
- 2- TMC heat exchangers can recover clean water from flue gas equal to 2.0% of steam.
- 3- There is no need for changing the boiler's design.
- 4- The dew point of flue gas reduces.

Figure 40 shows different inner parts of the designed shell and tube heat exchangers including the TMC tubes and baffles.



Figure 40. TMC Bundle Fabrication Layout [84].

Figure 41 shows the final assembly and details of the housing for the shell and tube heat exchangers.



Figure 41. Pilot test module of the TMC shell and tube heat exchangers [84].

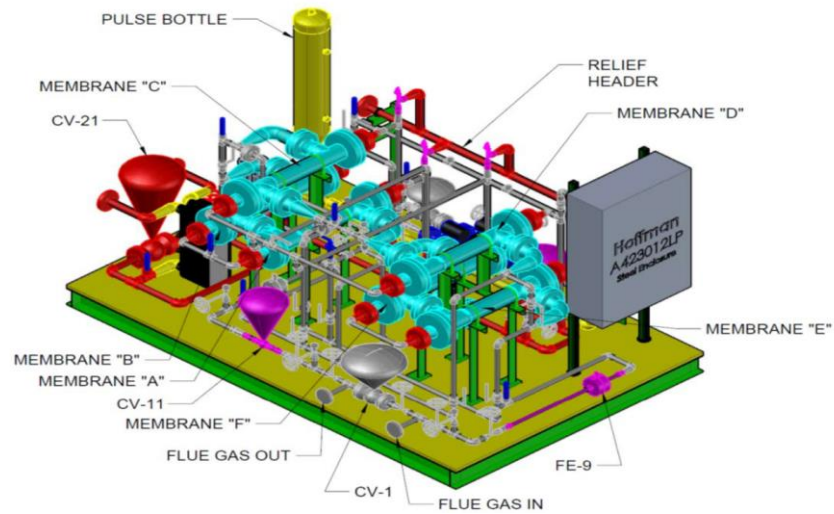
1.45. Critical dimensions for the shell and tube heat exchanger

The dimensions for the shell and tube heat exchanger are provided by GTI based on the manufactured module. Table 17 shows the membrane bundle specifications/dimensions and bundle tube spacing/layout including the baffle design.

Table 17. Membrane Bundle Dimensions/Specifications.

Overall Diameter [in]	4.0
Overall Length [in]	34
Number of Tubes [-]	90
Tube Diameter, OD [in]	0.285
Tube Diameter, ID [in]	0.14
Bundle Collar Length [in]	1.5
Tube Effective Length [in]	31
Tube Spacing, Nominal [mm]	2mm (wall to wall)
Pore Size [μm]	0.05 (outside coated)
O-ring Seals	Viton Dash Size –421

Two different configurations for a TMC heat exchanger system have been considered. A 2 by 3 and a 3 by 2 arrangement has been installed by GTI based on the results of simulation provided by FIU. The figure shows the schematic and the installed TMC system at GTI test facility.



(a)



(b)

Figure 42. a) TMC Test System Configuration and Installation [84]

1.46. Numerical modeling of shell and tube TMC unit

The current shell and tube heat exchanger is design to work in the operating condition of: (1) inlet flue-gas mass flow rate 0.0345864 (kg/s), (2) flue-gas temperature 450 (K), (3) H₂O mass fraction 0.3576, (4) O₂ mass fraction 0.01249, (5) N₂ mass fraction 0.00122, and (6) inlet water mass flow rate 0.325 (kg/s) and temperature 100 (K). The working pressure of the TMC heat exchanger is set to 200 psi, and all of the thermodynamic parameters were calculated based on the working pressure and by interpolating over the range of the working temperature [77]. In this study to different arrangements of the TMC unit with six shell and tube, TMC heat exchangers were studied (see Figure 43).

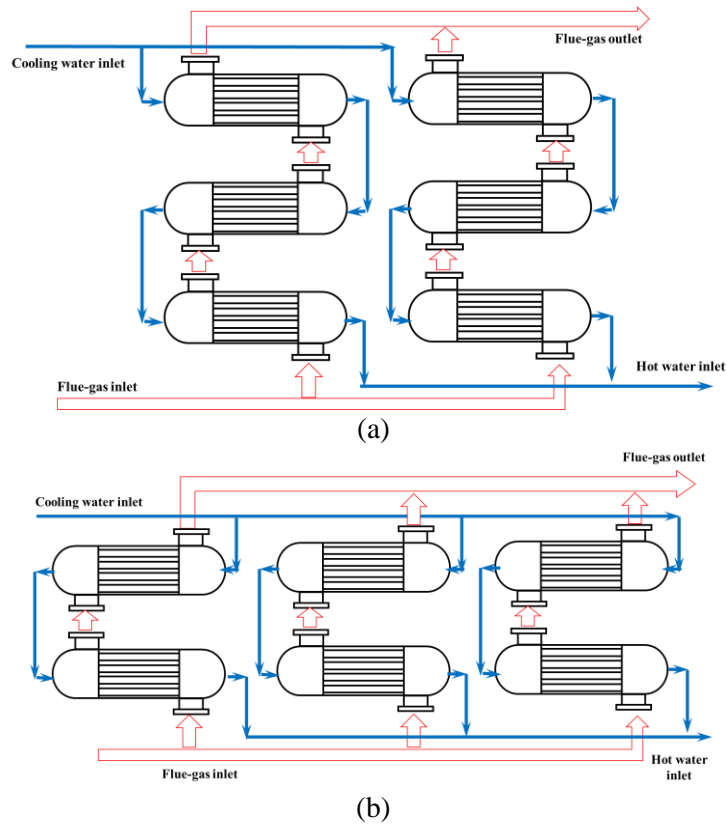
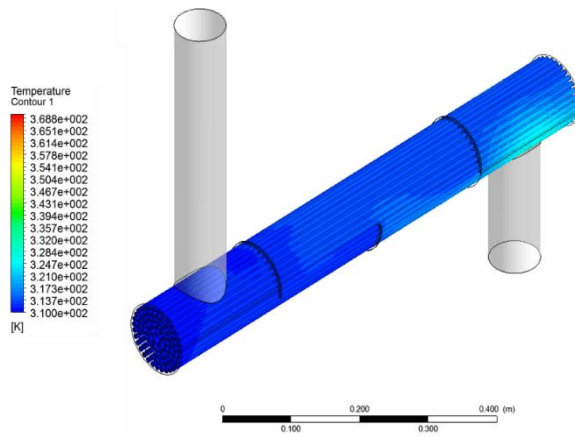


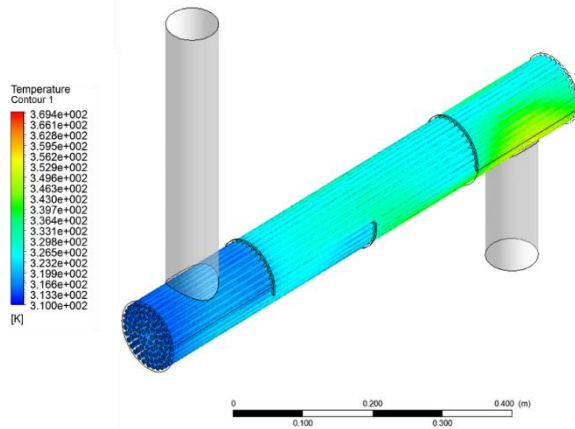
Figure 43. 2 and 3 stage configurations of the shell and tube TMC heat exchanger unit

The inlet flu-gas and water streams are evenly divided into 2 or 3 branches based on the configuration of the heat exchangers. Figure 44 shows the temperature contour for each stage of

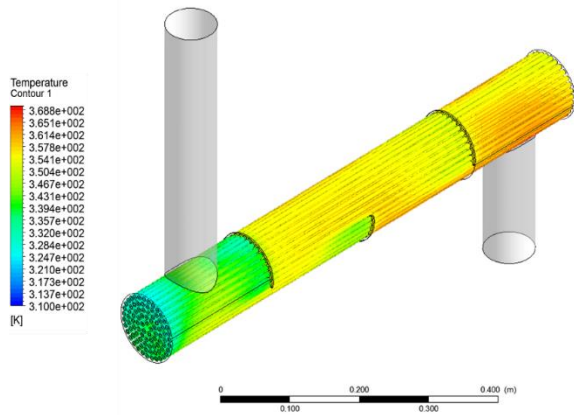
the 3-stage TMC unit. As seen in this figure, the TMC wall temperature is higher in the first stage where the flue-gas enter the heat exchanger unit. The temperature gradually decreases when the flue-gas passes through the second and third stage. For all the stages, the maximum wall temperature was near the entrance of the shell and tube heat exchangers. Moreover, the temperature contours show that there are some cold regions behind each baffle. The existence of these regions is due to the presence of the recirculation zones after the baffles.



a) 3rd stage



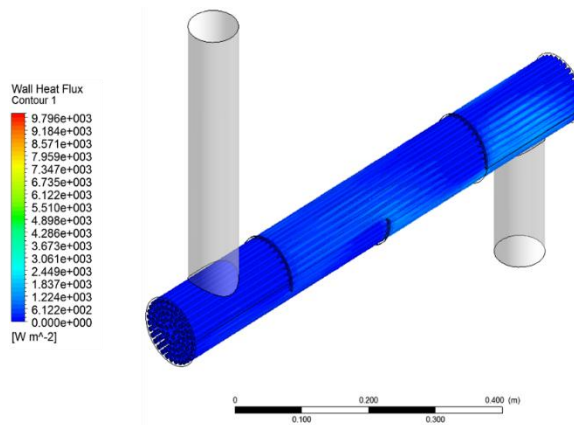
b) 2nd stage



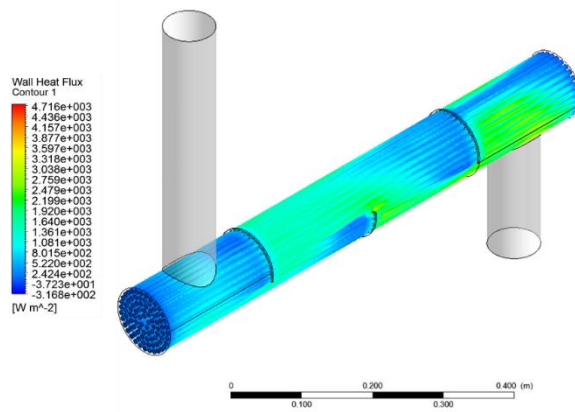
c) 1st stage

Figure 44. The contour of temperature on the TMC walls.

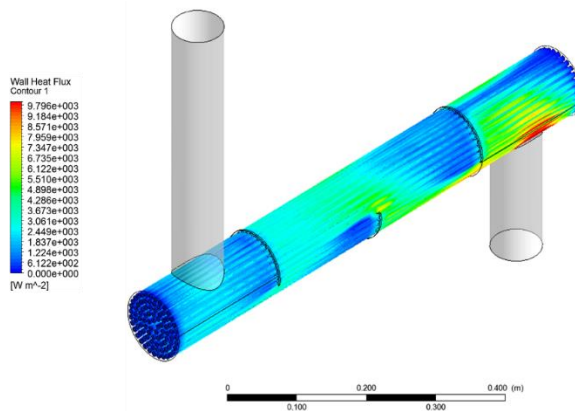
Figure 45 shows the wall heat flux contours for the 3-stage TMC heat exchanger. As can be seen, the heat flux pattern in each stage is consistent with the temperature contour in each stage. The maximum heat flux on the wall occurs in the areas in which the maximum temperature difference and hence the maximum heat transfer exist. So, the maximum wall flux occurs near the entrance of each heat exchanger and the areas behind the baffles have lower heat flux values.



a) 3rd stage



b) 2nd stage

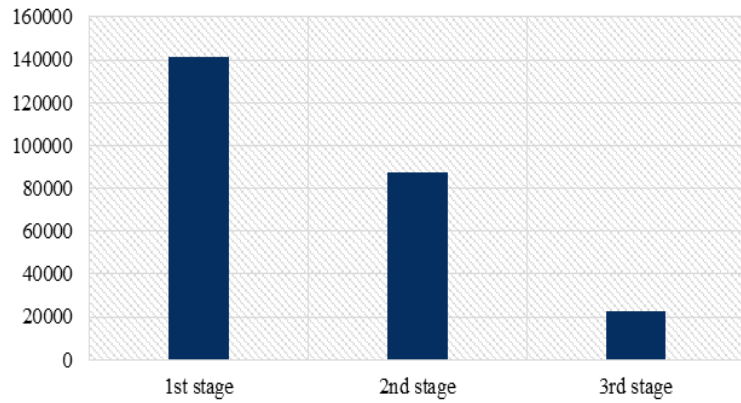


c) 1st stage

Figure 45. The contour of heat flux on the TMC walls.

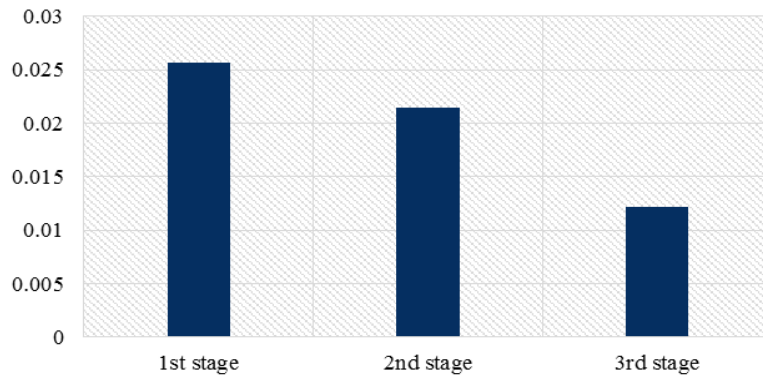
Heat transfer condensation rate of each stage for the 3-stage unit is shown in Figure 46. The maximum heat transfer and condensation rate belong to the first stage of the unit, and the performance of the shell and tube heat exchangers dramatically decrease from in the last stage of the heat exchanger.

Heat transfer rate (BTU/hr)



a) Heat transfer rate

Condensation rate (lb/s)



b) Condensation rate.

Figure 46. Heat transfer and condensation rate at each stage of the heat exchanger unit.

Figure 47 compares the overall performance of the 2-stage with the 3-stage configuration. As shown in this figure, the total heat transfer rate is higher for 2 stage TMC than that of 3 stage. As also can be seen from the figure the condensation rate for the 2 stage TMC is higher compared to the 3 stage one.

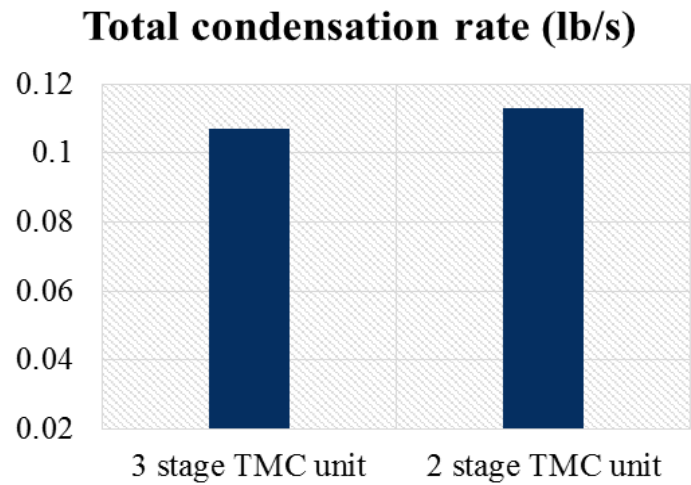
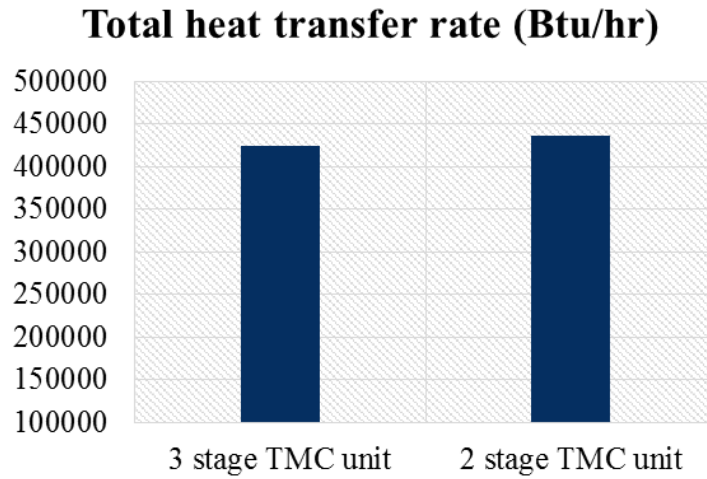


Figure 47. Heat transfer and condensation rate for 2 and 3 stage TMC units.

Comparison between the flue-gas and water outlet temperature for the 2- and 3- stage configurations is shown in Figure 48. The outlet-water temperature of the 2-stage configuration is higher while the flue-gas outlet temperature is lower than those of the 3- stage unit. This outcome is consistent with the result in Figure 47.

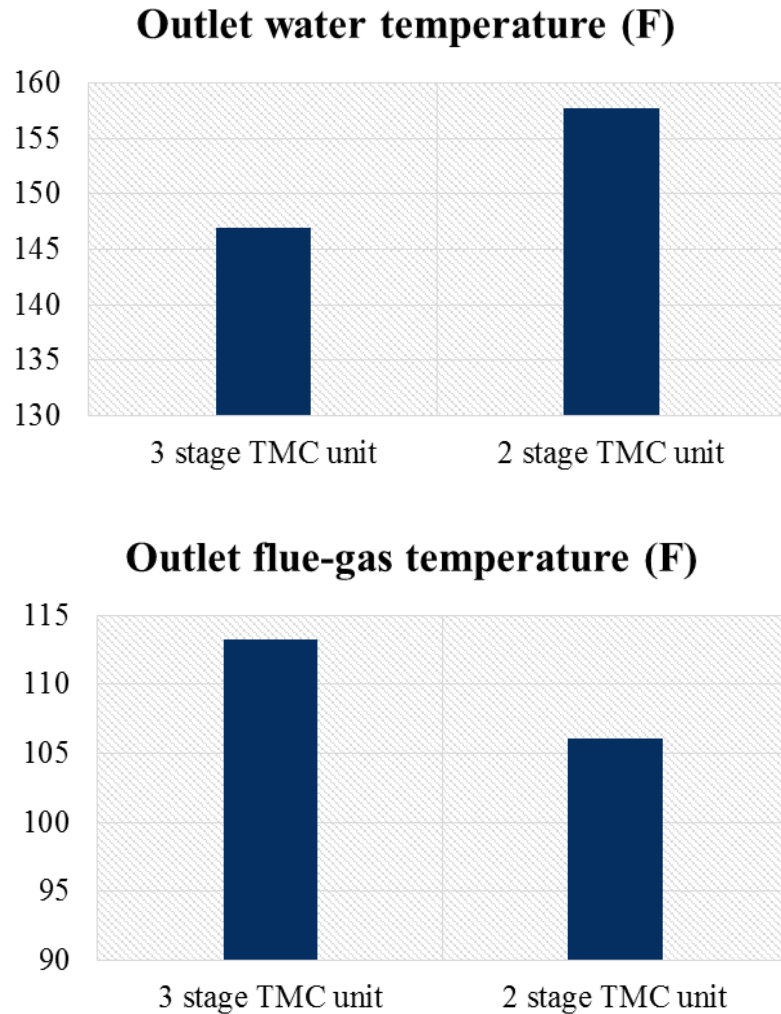
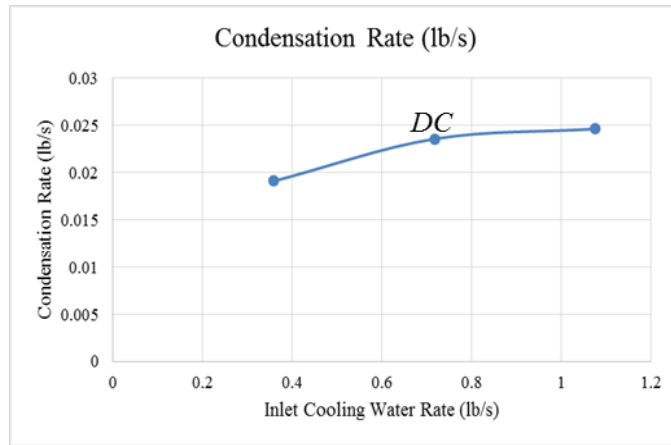


Figure 48. Comparison of the outlet temperatures between the 2 and 3 stage TMC units.

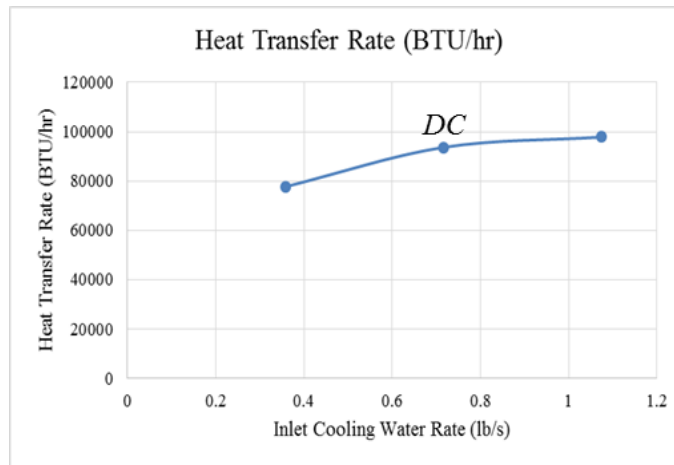
1.47. Effect of working conditions on the performance of the TMC unit

To investigate the off-design performance of the TMC shell and tube heat exchanger, the total heat transfer and condensation rate are obtained for the different range of inlet parameters. Figure 49 shows the effect of inlet cooling water flow rate on the condensation rate and total heat transfer in the TMC shell and tube heat exchanger. As it can be seen from this figure, increase of the cooling water flow rate increases both total heat transfer and condensation rate. By the increase of the water

flow rate, the average temperature of the water decreases in the TMC heat exchanger and the temperature difference between the cold and hot streams and consequently the heat transfer rate increases. Moreover, reducing the water temperature inside the TMC tubes results in lower surface temperature for the tubes and higher condensation rate for the system.



(a)

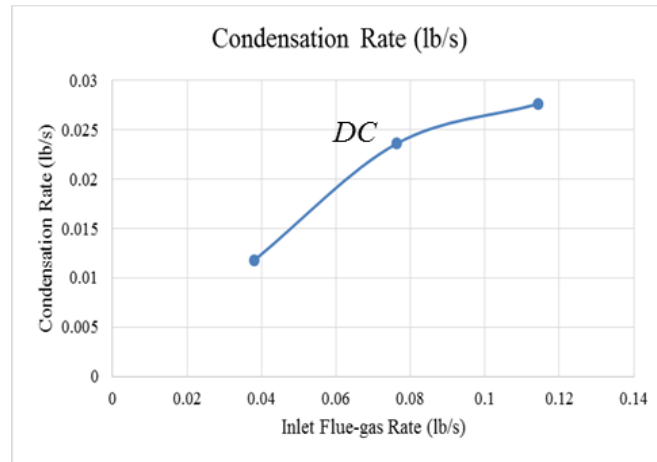


(b)

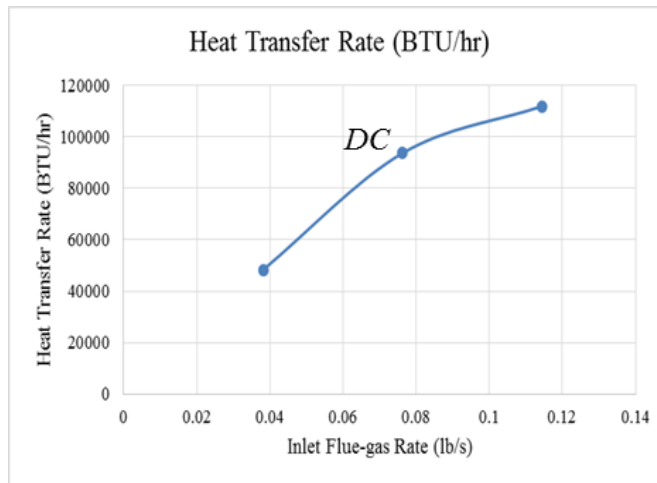
Figure 49. Effect of inlet cooling water flow rate.

The effect of inlet flue-gas mass flow rate on the heat transfer and condensation rate is shown in Figure 50. The figure indicates that both parameters increase with the increase of the flue-gas mass

flow rate. With the rise in the flow rate, the overall mass flow rate of the water vapor entering the TMC unit increases. With the increase of the water vapor, the condensation rate and the latent heat of condensation and accordingly the total heat transfer increases.



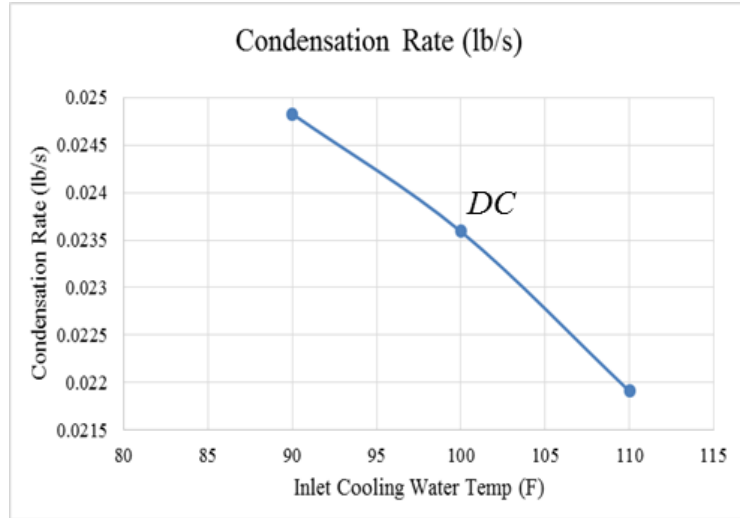
(a)



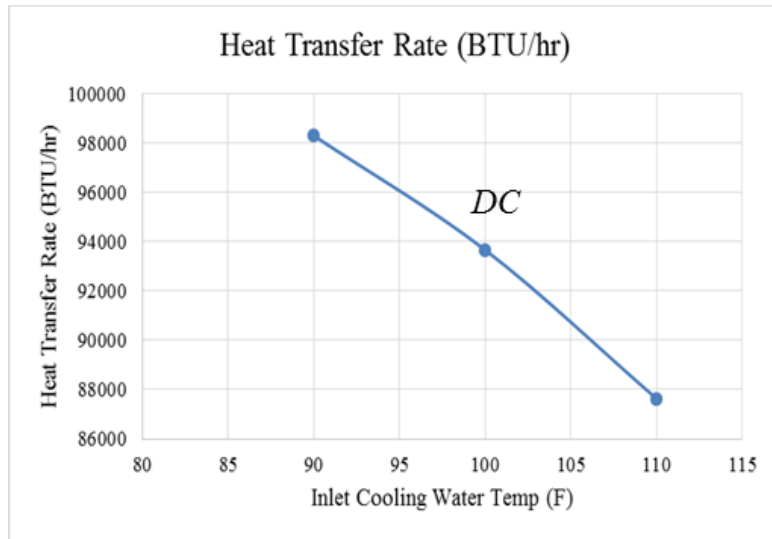
(b)

Figure 50.Effect of inlet flue-gas flow rate.

As seen in Figure 51 the condensation rate and heat transfer decrease with the increase of cooling water temperature. The rise in the water temperature decreases the temperature difference between the cold and hot stream and total heat transfer and condensation rate accordingly.



(a)



(b)

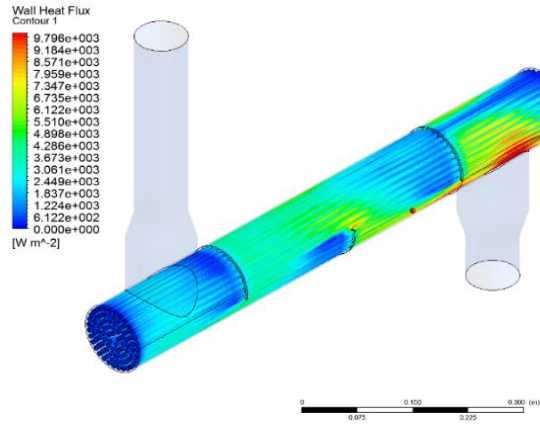
Figure 51. Effect of inlet cooling water temperature.

Table 18 shows the changes in condensation rate and heat transfer for the different off-design conditions in comparison with the performance of the TMC heat exchanger under the design condition. As seen, increasing the flue-gas flow rate causes the maximum change in the condensation rate and heat transfer. Moreover decreasing the flue gas or water flow rate decrease both heat transfer and condensation rate less than 20%. The effect of the change in the water temperature (+10 F or -10 F) is also negligible on the heat transfer and condensation rate of the TMC shell and tube heat exchanger.

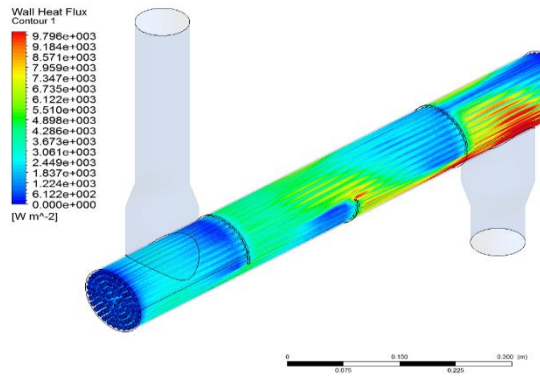
Table 18. Off-design performance of the TMC shell and tube heat exchanger.

Case	Condensation (%)	Heat transfer (%)
Flue-gas rate (+50%)	+17.1	+19.4
Flue-gas rate (-50%)	-49.9	-48.4
Water rate (+50)	+4.4	+4.4
Water rate (-50)	-18.9	-17.1
Water T (+10)	-7.1	-6.4
Water T (-10)	+5.2	+4.9

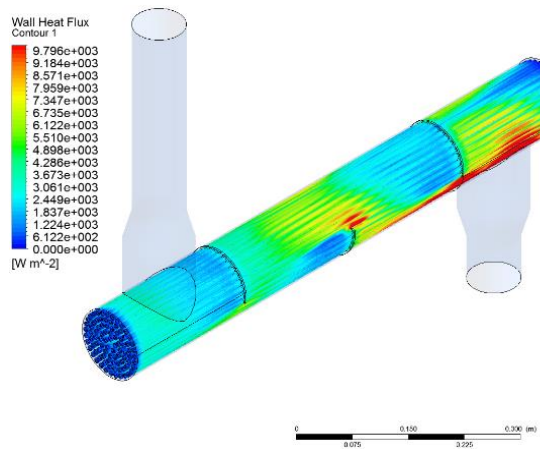
Figure 52 shows the wall heat flux inside the shell and tube TMC heat exchanger for the design condition, flue-gas inlet temperature +30 F and flue-gas flow rate +50% cases. As seen with the increase of flow rate and inlet temperature the wall heat flux increases. Moreover, the inlet region and the open region near the baffles are the high flux areas. The high heat flux in those areas is due to the high-temperature difference or higher flue-gas velocity in these regions. Moreover, the high heat flux regions also show the area with higher condensation rate inside the heat exchanger.



(a)



(b)



(c)

Figure 52. (a) design condition (b) FG temperature +30 F, (c) FG flow rate +50%.

7. Chapter 7: Conclusion and recommendations

Conclusion

In this research, a numerical procedure was proposed to simulate the condensation and heat transfer on the surface and inside of a Transport Membrane Condenser (TMC) heat exchanger. To estimate the condensation rate on the surface of the ceramic membrane two approaches were used. In the first approach (wall-based model) the condensation rate was obtained using the Fick's diffusion law and a correction factor based on the available experimental data. In the second approach (Mixed model), a condensation rate by considering the capillary condensation and the diffusion-based condensation was proposed.

The model has been implemented using User Defined Functions (UDFs) in Ansys Fluent and has been validated against the available experimental data provided by the industrial partner of the project from a lab scale test setup. The comparison showed that the mixed model predicts the performance of the heat exchangers more accurately regarding heat transfer and condensation rate.

Using the developed model, the effects of different inlet parametereters such as temperature, mass flow rate and the relative inlet humidity on the overall heat and water transfer inside the cross-flow TMC heat exchanger have been investigated. The performance of the cross-flow TMC heat exchangers was obtained for inlet flue-gas flow rate of 40 to 120 kg/h, inlet water flow rate 60 to 140 kg/h, inlet flue-gas temperature 340 to 360 K, inlet water temperature 295 to 315 K, inlet flue-gas relative humidity 20 to 90 %, and tube pitch ratio of 0.25 to 2.25.

The results showed that within the range of the investigated range, the water condensation flux continuously increases with the increase of the inlet flue-gas flow rate, water flow rate and the flue-gas humidity. The total heat flux also follows the same trend due to the pronounced effect of the latent heat transfer from the condensation process. The water condensation flux and the overall heat

transfer increase at the beginning for small values of the tube pitches and then decreases as the tube pitch rises furthermore.

Also, the effects of tube spacing and a flue-gas inlet water vapor mass fraction on the heat transfer and pressure drop along the TMC heat exchanger have been investigated. The results showed that for the small water vapor mass fractions, there is an optimum tube spacing for the TMC heat exchanger which results in maximum overall volumetric heat transfer density.

In the second part of this research, the performance of shell and tube TMC heat exchangers for high pressure and temperature applications has been studied. Two different configurations of the TMC heat exchanger unit including six shell and tube heat exchangers have been considered. The simulations were carried out for the inlet flue-gas mass flow rate 0.0345864 (kg/s), flue-gas temperature 450 (K), H₂O mass fraction 0.3576, O₂ mass fraction 0.01249, N₂ mass fraction 0.00122, and inlet water mass flow rate 0.325 (kg/s) and temperature 100 (K).

Comparison between the overall performance of the 2-stage with the 3-stage configuration shows that the total heat transfer of the 2-stage TMC unit is higher than that of the 3-stage TMC unit. The condensation rate for the 2-stage TMC unit is also higher compared to the 3-stage one. Moreover, a variation of the condensation rate and heat transfer for the shell and tube TMC units have been studied and reported.

Recommendations

Considering the importance of the nanoscale transport phenomena such as capillary condensation inside the nanopores during the condensation in TMC tubes, using a multi-scale could effectively increase the accuracy and application range of the current model. Molecular Dynamics (MD) has been used previously to predict the condensation inside a nanopore. The main issue of using MD

is the high computational cost of this numerical technique for the large-scale application. Using the current modeling procedure, the prediction of the condensation rate by the MD can be used. Hence the Control Volume Method will be used for all regions except the nanoporous layer. The surface of the TMC tubes can be divided into different sections based on the availability of computational resources.

The TMC tubes have a multi-layer structure, and each layer has different thickness, pore size, thickness and surface tension. Optimization of the construction of the different layer of the TMC in order to obtain higher total performance of TMC tubes specifically for lower temperature applications could be beneficial to many other engineering fields including HVAC and producing clean water from the atmosphere.

References

- [1] D. Wang, "Final technical report, Advanced Energy and Water Recovery Technology from Low Grade Waste Heat, No. DOE/EE0003477-1," 2011.
- [2] E. Use, "Loss, and Opportunities Analysis: US Manufacturing & Mining Industrial Technologies Program.," 2004.
- [3] A. Prasad, "Power generation from waste heat using organic rankine cycle systems," 1980.
- [4] A. Thekdi and S. U. Nimbalkar, "Industrial Waste Heat Recovery-Potential Applications, Available Technologies and Crosscutting R&D Opportunities," Oak Ridge National Lab.(ORNL), Oak Ridge, TN (United States), 2015.
- [5] X. Gou, H. Xiao, and S. Yang, "Modeling, experimental study and optimization on low-temperature waste heat thermoelectric generator system," *Appl. Energy*, vol. 87, no. 10, pp. 3131–3136, Oct. 2010.
- [6] M. W. Browne and P. K. Bansal, "An overview of condensation heat transfer on horizontal tube bundles," *Appl. Therm. Eng.*, vol. 19, no. 6, pp. 565–594, 1999.
- [7] M. Osakabe, K. Ishida, K. Yagi, T. Itoh, and K. Ohmasa, "Condensation heat transfer on tubes in actual flue gas," *Heat Transf. - Asian Res.*, vol. 30, no. 2, pp. 139–151, 2001.
- [8] W. Zhou, G. Henderson, and S. T. Revankar, "Condensation in a vertical tube bundle passive condenser - Part 1: Through flow condensation," *Int. J. Heat Mass Transf.*, vol. 53, no. 5–6, pp. 1146–1155, 2010.
- [9] W. Zhou, G. Henderson, and S. T. Revankar, "Condensation in a vertical tube bundle passive condenser - Part 1: Through flow condensation," *Int. J. Heat Mass Transf.*, vol. 53, no. 5–6, pp. 1146–1155, 2010.
- [10] D. Che, Y. Da, and Z. Zhuang, "Heat and mass transfer characteristics of simulated high moisture flue gases," *Heat Mass Transf.*, vol. 41, no. 3, pp. 250–256, Jul. 2004.
- [11] Y. Liang, D. Che, and Y. Kang, "Effect of vapor condensation on forced convection heat transfer of moistened gas," *Heat Mass Transf.*, vol. 43, no. 7, pp. 677–686, Mar. 2007.
- [12] K. Mosthaf *et al.*, "A coupling concept for two-phase compositional porous-medium and single-phase compositional free flow," *Water Resour. Res.*, vol. 47, no. 10, 2011.
- [13] H. Nabati, "Investigation on Numerical Modeling of Water Vapour Condensation from a Flue Gas with High COR2R Content," *Energy Power Eng.*, vol. 03, no. 02, pp. 181–189, 2011.
- [14] R. Ray, "Research on an energy-efficient drying process.," *Final Rep. (No. DOE/ID/12293-1). Bend Res. Inc., OR (USA).*, 1986.
- [15] B. Us, R. A. Knight, and I. K. Rabovitser, "Method and apparatus for enhanced heat

- recovery from steam generators and water heaters,” *No. 7,066,396. Gas Technol. Institute, Des Plaines, (United States)*, pp. 1–8, 2014.
- [16] D. Wang, “Transport Membrane Condenser for Water and Energy Recovery from Power Plant Flue Gas,” *Natl. Energy Technol. Lab.*, 2012.
- [17] T. Devitt, P. Spaite, and L. Gibbs, “Population and characteristics of industrial/commercial boilers in the US Final report Mar 78-May 79,” 1979.
- [18] E. Series, “Residential Energy Consumption Survey,” 1993.
- [19] U. S. D. of E. (DOE’s), “Energy Intensive Processes (EIP) Portfolio - Waste Heat Minimization and Recovery platform,” 2011.
- [20] H. Strathmann, B. Bauer, and J. Kerres, “Polymer membranes with selective gas and vapor permeation properties,” *Makromol. Chemie. Macromol. Symp.*, vol. 33, no. 1, pp. 161–178, 1990.
- [21] J. Randan and R. Paterson, “Preliminary studies on the potential for gas separation by mesoporous ceramic oxide membranes surface modified by alkyl phosphonic acids,” *J. Memb. Sci.*, vol. 134, pp. 219–223, 1997.
- [22] R. G. Grant, “Membrane Separations,” *Mater. Manuf. Process.*, vol. 4, no. 4, pp. 483–503, 1989.
- [23] R. Dittmeyer and J. Caro, “Catalytic Membrane Reactors,” in *Handbook of Heterogeneous Catalysis*, 2008.
- [24] M. M. Qiu and S. T. Hwang, “Continuous vapor-gas separation with a porous membrane permeation system,” *J. Memb. Sci.*, vol. 59, no. 1, pp. 53–72, 1991.
- [25] A. B. and D.-X. Wang, “Nanoporous Membrane Tube Condensing Heat Transfer,” *Imece2011*, pp. 1–7, 2011.
- [26] “Gas Technology Institute.” [Online]. Available: <http://www.gastechnology.org/Pages/default.aspx>.
- [27] “SmartBurn LLC.” [Online]. Available: <http://www.smartburn.com/>.
- [28] T. Wang, M. Yue, H. Qi, P. H. M. Feron, and S. Zhao, “Transport membrane condenser for water and heat recovery from gaseous streams: Performance evaluation,” *J. Memb. Sci.*, vol. 484, pp. 10–17, 2015.
- [29] H. Chen, Y. Zhou, S. Cao, X. Li, X. Su, and L. An, “Heat exchange and water recovery experiments of flue gas with using nanoporous ceramic membranes,” *Appl. Therm.*, vol. 110, pp. 686–694, 2017.
- [30] M. Yue, S. Zhao, P. H. M. Feron, and H. Qi, “Multichannel Tubular Ceramic Membrane for Water and Heat Recovery from Waste Gas Streams,” *Ind. Eng. Chem. Res.*, vol. 55, no. 9, pp. 2615–2622, 2016.

- [31] H. W. Hu, G. H. Tang, and D. Niu, “Wettability modified nanoporous ceramic membrane for simultaneous residual heat and condensate recovery,” *Sci. Rep.*, vol. 6, p. 27274, 2016.
- [32] Ramesh K. Shah and Dušan P. Sekulic, *Fundamentals of Heat Exchanger Design*. 2003.
- [33] Y. A. Cengel and J. Hernán Pérez, “Heat transfer: a practical approach. Transferencia de calor/,” 2004.
- [34] K. Karkoszka, “Mechanistic Modeling of Water Vapour Condensation in Presence of Noncondensable Gases,” *Dr. Diss. KTH*, 2007.
- [35] A. Dehbi and S. Guentay, “A model for the performance of a vertical tube condenser in the presence of noncondensable gases,” *Nucl. Eng. Des.*, vol. 177, no. 1–3, pp. 41–52, 1997.
- [36] T. Tagami, “NoInterim Report on Safety Assessments and Facilities,” 1965.
- [37] H. Uchida, A. Oyama, and Y. Togo, “Evaluation of post-accident cooling systems of LWR’s,” *Proc. Int. Conf. Peac. Uses At. Energy*, vol. 13, pp. 93–102, 1965.
- [38] A. P. Colburn and O. A. Hougen, “Design of Cooler Condensers for Mixtures of Vapors with Noncondensing Gases,” *Ind. Eng. Chem.*, vol. 26, no. 11, pp. 1178–1182, 1934.
- [39] A. Dehbi, F. Janasz, and B. Bell, “Prediction of steam condensation in the presence of noncondensable gases using a CFD-based approach,” *Nucl. Eng. Des.*, vol. 258, pp. 199–210, 2013.
- [40] C. K. Chen and Y. T. Lin, “Turbulent film condensation in the presence of non-condensable gases over a horizontal tube,” *Int. J. Therm. Sci.*, vol. 48, no. 9, pp. 1777–1785, 2009.
- [41] I. Kljenak, M. Babić, B. Mavko, and I. Bajsić, “Modeling of containment atmosphere mixing and stratification experiment using a CFD approach,” *Nucl. Eng. Des.*, vol. 236, no. 14–16, pp. 1682–1692, 2006.
- [42] H. Uchida, “Evaluation of Post incident cooling system of light water power reactors,” in *International Conference on the Peaceful Uses of Atomic Energy, Geneva, Switzerland.*, 1965, pp. 93–102.
- [43] J. Malet, E. Porcheron, F. Dumay, and J. Vendel, “Code-experiment comparison on wall condensation tests in the presence of non-condensable gases - Numerical calculations for containment studies,” *Nucl. Eng. Des.*, vol. 253, pp. 98–113, 2012.
- [44] J. C. de la Rosa, L. E. Herranz, and J. L. Muñoz-Cobo, “Analysis of the suction effect on the mass transfer when using the heat and mass transfer analogy,” *Nucl. Eng. Des.*, vol. 239, no. 10, pp. 2042–2055, 2009.
- [45] M. Bucci, M. Sharabi, W. Ambrosini, N. Forgiione, F. Oriolo, and S. He, “Prediction of transpiration effects on heat and mass transfer by different turbulence models,” *Nucl. Eng. Des.*, vol. 238, no. 4, pp. 958–974, 2008.

- [46] K. Karkoszka and H. Anglart, “Multidimensional effects in laminar filmwise condensation of water vapour in binary and ternary mixtures with noncondensable gases,” *Nucl. Eng. Des.*, vol. 238, no. 6, pp. 1373–1381, 2008.
- [47] M. Houkema, N. B. Siccama, J. A. Lycklama à Nijeholt, and E. M. J. Komen, “Validation of the CFX4 CFD code for containment thermal-hydraulics,” *Nucl. Eng. Des.*, vol. 238, no. 3, pp. 590–599, 2008.
- [48] “Ansys, Inc.” [Online]. Available: <http://www.ansys.com/>.
- [49] M. Asbik, A. Daif, P. K. Panday, and A. Khmou, “Numerical study of laminar condensation of downward flowing vapour on a single horizontal cylinder or a bank of tubes,” *Can. J. Chem. Eng.*, vol. 77, no. 1, pp. 54–61, 1999.
- [50] E. M. Sparrow, W. J. Mtnkowycz, and M. Saddy, “Forced convection condensation in the presence of noncondensables and interfacial resistances,” *J. Heat Mass Transf.*, vol. 10, pp. 1829–1845, 1967.
- [51] G. Zschaecck, T. Frank, and A. D. Burns, “CFD modelling and validation of wall condensation in the presence of non-condensable gases,” *Nucl. Eng. Des.*, vol. 279, pp. 137–146, 2014.
- [52] W. Ambrosini, N. Forgione, D. Mazzini, and F. Oriolo, “Computational Study of Evaporative Film Cooling in a Vertical Rectangular Channel,” *Heat Transf. Eng.*, vol. 23, no. 5, pp. 25–35, 2002.
- [53] A. Dehbi, “On the adequacy of wall functions to predict condensation rates from steam-noncondensable gas mixtures,” *Nucl. Eng. Des.*, vol. 265, pp. 25–34, 2013.
- [54] F. Moukalled, S. Verma, and M. Darwish, “The use of CFD for predicting and optimizing the performance of air conditioning equipment,” *Int. J. Heat Mass Transf.*, vol. 54, no. 1–3, pp. 549–563, 2011.
- [55] R. Benelmir, S. Mokraoui, and A. Souayed, “Numerical analysis of filmwise condensation in a plate fin-and-tube heat exchanger in presence of non-condensable gas,” *Heat Mass Transf. und Stoffuebertragung*, vol. 45, no. 12, pp. 1561–1573, 2009.
- [56] J. Lee, G.-C. Park, and H. K. Cho, “Improvement of CUPID code for simulating filmwise steam condensation in the presence of noncondensable gases,” *Nucl. Eng. Technol.*, vol. 47, no. 5, pp. 567–578, Aug. 2015.
- [57] J. Lehmkuhl, S. Kelm, M. Bucci, and H.-J. Allelein, “Improvement of wall condensation modeling with suction wall functions for containment application,” *Nucl. Eng. Des.*, vol. 299, pp. 105–111, Apr. 2016.
- [58] L. Vyskocil, J. Schmid, and J. Macek, “CFD simulation of air–steam flow with condensation,” *Nucl. Eng. Des.*, vol. 279, pp. 147–157, Nov. 2014.
- [59] H. Sun, G. Lauriat, and X. Nicolas, “Natural convection and wall condensation or evaporation in humid air-filled cavities subjected to wall temperature variations,” *Int. J.*

Therm. Sci., vol. 50, no. 5, pp. 663–679, May 2011.

- [60] R. C. Reid, J. M. Prausnitz, and T. K. Sherwood, “The Properties of Gases and Liquids, McGraw-Hill, New York, 1987,” *Google Sch.*, p. 592.
- [61] D. R. Lide and H. V. Kehiaian, *CRC Handbook of Thermophysical and Thermochemical Data*. CRC Press, 1994.
- [62] V. Dharma Rao, V. Murali Krishna, K. V. Sharma, and P. V. J. M. Rao, “Convective condensation of vapor in the presence of a non-condensable gas of high concentration in laminar flow in a vertical pipe,” *Int. J. Heat Mass Transf.*, vol. 51, no. 25–26, pp. 6090–6101, 2008.
- [63] M. Saraireh, “Heat transfer and condensation of water vapour from humid air in compact heat exchangers,” 2012.
- [64] J. P. Holman, “Heat transfer, 1986,” *Mc Gran--Hill B. Company, Soythern Methodist Univ.*, 1986.
- [65] H. A. McGee, *No Title*. New York: McGraw-Hill, 1991.
- [66] K. K. Kenneth, *Principles of combustion*. New York: John Willey & Sons, 1986.
- [67] C.-X. Lin, D. Wang, and A. Bao, “Numerical modeling and simulation of condensation heat transfer of a flue gas in a bundle of transport membrane tubes,” *Int. J. Heat Mass Transf.*, vol. 60, pp. 41–50, 2013.
- [68] F. R. Menter, “Two-equation eddy-viscosity turbulence models for engineering applications,” *AIAA J.*, vol. 32, no. 8, pp. 1598–1605, 1994.
- [69] V. Yakhot and S. A. Orszag, “Renormalization Group Analysis of Turbulence: I. Basic Theory,” *J. Sci. Comp.*, vol. 1(1), pp. 1–51, 1986.
- [70] H. K. Versteeg and Weeratunge Malalasekera, *An introduction to computational fluid dynamics: the finite volume method*. Pearson Education, 2007.
- [71] A. Dehbi, F. Janasz, and B. Bell, “Prediction of steam condensation in the presence of noncondensable gases using a CFD-based approach,” *Nucl. Eng. Des.*, vol. 258, pp. 199–210, 2013.
- [72] B. A. Kader, “Temperature and Concentration Profiles in Fully Turbulent Boundary Layers,” *Int. J. Heat Mass Transf.*, vol. 24, no. 9, pp. 1541–1544, 1981.
- [73] J. M. Martín-Valdepeñas, M. A. Jiménez, F. Martín-Fuertes, and J. A. F. Benítez, “Comparison of film condensation models in presence of non-condensable gases implemented in a CFD Code,” *Heat Mass Transf.*, vol. 41, no. 11, pp. 961–976, Sep. 2005.
- [74] K. Das, C. Manepally, R. Fedors, D. Basu, and S. Antonio, “NUMERICAL AND EXPERIMENTAL STUDY OF IN-DRIFT HEAT AND MASS TRANSFER

PROCESSES Prepared for Center for Nuclear Waste Regulatory Analyses U . S . Nuclear Regulatory Commission Washington DC September 2011,” no. September, 2011.

- [75] M. Lejon, “Wall Condensation Modelling in Convective Flow.” 2013.
- [76] X. Cheng *et al.*, “Experimental data base for containment thermalhydraulic analysis,” *Nucl. Eng. Des.*, vol. 204, no. 1–3, pp. 267–284, Feb. 2001.
- [77] “NIST webbook.” [Online]. Available: <http://webbook.nist.gov/chemistry/>.
- [78] B. Bischoff, *ADVANCED MEMBRANE SEPARATION TECHNOLOGIES FOR ENERGY RECOVERY FROM INDUSTRIAL* Prepared by. 2013.
- [79] H. L. Weissberg, “Effective Diffusion Coefficient in Porous Media,” *J. Appl. Phys.*, vol. 34, no. 9, pp. 2636–2639, 1963.
- [80] J.-G. Choi, D. D. Do, and H. D. Do, “Surface Diffusion of Adsorbed Molecules in Porous Media: Monolayer, Multilayer, and Capillary Condensation Regimes,” *Ind. Eng. Chem. Res.*, vol. 40, no. 19, pp. 4005–4031, 2001.
- [81] B. Abeles, L. F. Chen, J. W. Johnson, and J. M. Drake, “Capillary Condensation and Surface Flow in Microporous Vycor Glass,” *Isr. J. Chem.*, vol. 31, no. 2, pp. 99–106, 1991.
- [82] P. Uchytíl, R. Petrickovic, and A. Seidel-Morgenstern, “Study of capillary condensation of butane in a Vycor glass membrane,” *J. Memb. Sci.*, vol. 264, no. 1–2, pp. 27–36, 2005.
- [83] R. E. Sonntag, C. Borgnakke, G. J. Van Wylen, and S. Van Wyk, *Fundamentals of thermodynamics*, vol. 6. Wiley New York, 1998.
- [84] D. Wang, “Flue Gas Water Vapor Latent Heat Recovery for Pressurized Oxy-Combustion,” *Gas Technol. Inst.*, vol. DE-FE00253.

Appendix

Matlab code and list of the user defined functions:

- Main program is the modified version of the code which has been developed by Lejon [75]:

```
% condensation rate; analytical solution

clear

clc

close all

%-----

% Tabulated data from (E. M. Sparrow, 1967)

F_table=[0.05 0.10 0.15 0.20 0.25 0.30 0.35 0.40 0.45 0.50 0.60 0.70 1.0 1.5 2.0 3.0 4.0 5.0 6.0
10.0];

Rlarge_table=[0.013358 0.036827 0.066008 0.099244 0.13556 0.17431 0.21501 0.25733 0.30098
0.34575 0.43799 0.53298 0.82825 1.3360 1.8495 2.8759 3.8967 4.9125 5.9244 9.9518];

Wratio_table=[0.95073 0.90510 0.86273 0.82332 0.78658 0.75225 0.72013 0.69002 0.66175
0.63517 0.58654 0.54321 0.43803 0.31857 0.24075 0.14927 0.10047 0.07173 0.05322 0.02161];

% tabulated data obtained from "Fundamentals of Heat and Mass Transfer",
% Third edition, Frank P. Incropera, David P. De Witt

Temp_table=[273.15; 290; 315; 340; 365; 385];

Pr_water_table=[12.99; 7.56; 4.16; 2.66; 1.91; 1.53];

Cp_water_table=[4217; 4184; 4179; 4188; 4209; 4232];

rho_water_table=[1000/1; 1000/1.001; 1000/1.009; 1000/1.021; 1000/1.038; 1000/1.053];

mu_water_table=[1750e-6; 1080e-6; 631e-6; 420e-6; 306e-6; 248e-6];

h_fg_table=[2502e3; 2461e3; 2402e3; 2342e3; 2278e3; 2225e3];

rho_vapor_temp=[380 400 450 500];
```

```

rho_vapor_table=[0.5863 0.5542 0.4902 0.4405];
Temp_air_table=[250; 300; 350; 400; 450];
rho_air_table=[1.3947; 1.1614; 0.9950; 0.8711; 0.7740];

T_inf=373.15; %free stream temperature
T_w=364.81; % wall temperature
W=0.05; % Mass fraction of the non-condensable component

p_v= satpress(T_inf);
M_v=18.01528; %g/mol, Molecular mass for water
M_g=28.97; %g/mol, Molecular mass for air

p=p_v*(1-W*(1-M_v/M_g))/(1-W); %Eq. 35 from article
T_i=(T_w+T_inf)/2; % Trial value of interface temperature T_i

for index=1:15

p_i=satpress(T_i);
W_i=(1-p_i/p)/(1-(p_i/p)*(1-M_v/M_g));% interpolate values at the interface temperature
rho_water=interp1(Temp_table,rho_water_table,T_i);
mu_water=interp1(Temp_table,mu_water_table,T_i);

rho_interface=0.5879; % obtained from CAE
mu_interface=0.000014009; % obtained from CAE

```

```

mu=1.2901e-5; % obtained from CAE

R=sqrt((rho_water*mu_water)/(rho_interface*mu_interface));

Pr=interp1(Temp_table,Pr_water_table,T_i); %Pr for water

Cp=interp1(Temp_table,Cp_water_table,T_i); %Cp for water

h_fg=interp1(Temp_table,h_fg_table,T_i); %latent heat

sum=R*Cp*(T_i-T_w)/(h_fg*Pr);

Wratio=interp1(Rlarge_table,Wratio_table,sum);

W_i=W/Wratio;

p_i=p*(1-W_i)/(1-W_i*(1-M_v/M_g));

T_i=sattemp(p_i);

if index>1

    disp([index T_i abs(T_i_old-T_i)/T_i*100])

end

T_i_old=T_i;

end

F=interp1(Wratio_table,F_table,W/W_i);

rho=0.5663; % obtained from CFD solution

Uinf=1;

index=0;

for x=0.01:0.01:1

    index=index+1;

```

```

xcoord(index)=x;
massflux(index)=0.5*sqrt(rho*mu*Uinf/x)*F;
end

figure(1)
plot(xcoord,massflux,'b--','LineWidth',3);
axis([10^-2 1 10^-3 0.01])
title('Flat plate; Inlet velocity = 1 (ms^{-1}); MF-H_2O(g)=0.05')
xlabel('Distance from the leading edge [m]')
ylabel('Condensation mass flux [kg m^{-2} s^{-1}]')
legend('Analytical solution (Sparrow et. al. 1967)',1)

```

➤ functions:

```

function press = satpress(temp)
press = exp( 23.1512 - 3788.02 / ( temp-47.3018 ));
end

function temp = sattemp(press)
temp = 47.3018 - 3788.02 / ( log(press) - 23.1512 );
end

```

Table 19. List of the UDFs which have been used in the numerical simulation.

real H2O_vapor_pressure(real T)	Returns saturated pressure of water vapor
real H2O_vapor_temperature(real P)	Returns saturated temperature of water vapor
real mean_MW(cell_t c, Thread *tc)	Returns molar weight of the mixture
real Latent_Heat(real T)	Returns latent heat of condensation for water
real H2O_Air_diff(real P,real T)	Returns diffusion coefficient of water in the air
DEFINE_PROPERTY(air_density, c, t)	Returns the air density based on ideal gas law
DEFINE_ADJUST(evap_condense_adjust, domain)	Condensation rate and assigns the pertinent user-defined memories
DEFINE_SOURCE(mass_sink_fg, c, tc, dsourc, mass)	Defines mass sink term for continuity equation in the flue-gas side
DEFINE_SOURCE(energy_sink_fg, c, tc, dsourc, energy)	Defines energy sink term for condensing species in flue-gas side
DEFINE_SOURCE(k_sink_fg, c, tc, dsourc, kequation)	Defines k sink term for condensing species in flue-gas side
DEFINE_SOURCE(epsilon_sink_fg, c, tc, dsourc, epsilonequation)	Defines epsilon sink term for condensing species in flue-gas side
DEFINE_SOURCE(omrgas_sink_fg, c, tc, dsourc, omeganequation)	Define omega sink term for condensing species in flue-gas side
DEFINE_SOURCE(U_sink_fg, c, tc, dsourc, Uequation)	Defines U sink term for condensing species in flue-gas side
DEFINE_SOURCE(V_sink_fg, c, tc, dsourc, Vequation)	Defines V sink term for condensing species in flue-gas side
DEFINE_SOURCE(W_sink_fg, c, tc, dsourc, Wequation)	Defines W sink term for condensing species in flue-gas side
DEFINE_SOURCE(mass_source_tube, c, tc, dsourc, energy)	Defines mass source term for in porous-tube side
DEFINE_SOURCE(species_source_tube, c, tc, dsourc, energy)	Defines species source term for in porous-tube side
DEFINE_SOURCE(energy_source_tube, c, tc, dsourc, energy)	Defines flue-gas energy source term for in porous-tube side
DEFINE_PROFILE(YI_condensing_surf, tf, eqn)	Mass fraction of vapor profile on the surface with condensation

VITA

SOHEIL SOLEIMANIKUTANA EI

- 2013 – 2018 Ph.D., Mechanical Engineering, Florida International University, Miami, Florida
- 2009 – 2011 M.Sc., Mechanical Engineering, Babol University of Technology
- 2003 – 2007 B.Sc., Mechanical Engineering University of Mazandaran

SELECTED PUBLICATIONS:

1. Soleimanikutanaei, Soheil, Cheng-Xian Lin, and Dexin Wang. "Numerical modeling and analysis of Transport Membrane Condensers for waste heat and water recovery from flue gas." *International Journal of Thermal Sciences* 136 (2019): 96-106.
2. Soleimanikutanaei, Soheil, C. X. Lin, and Dexin Wang. "Modeling and simulation of cross-flow transport membrane condenser heat exchangers." *International Communications in Heat and Mass Transfer* 95 (2018): 92-97.
3. Ghasemi, E., H. Bararnia, Soheil Soleimanikutanaei, and C. X. Lin. "Direct numerical simulation and analytical modeling of electrically induced multiphase flow." *International Journal of Mechanical Sciences* 142 (2018): 397-406.
4. Soleimanikutanaei, Soheil, Esmail Ghasemisahebi, and Cheng-Xian Lin. "Numerical study of heat transfer enhancement using transverse microchannels in a heat sink." *International Journal of Thermal Sciences* 125 (2018): 89-100.
5. Ghasemi, E., H. Bararnia, Soheil Soleimanikutanaei, and C. X. Lin. "Simulation of deformation and fragmentation of a falling drop under electric field." *Powder Technology* 325 (2018): 301-308.
6. Chapter book: Olubunmi Popoola, Soheil Soleimanikutanaei and Yiding Cao, Reciprocating Mechanism Driven Heat Loop (RMDHL) Cooling Technology for Power Electronic Systems" in "Electronics Cooling", InTechOpen publication, page 129-150.
7. Popoola, Olubunmi, Soheil Soleimanikutanaei, and Yiding Cao. "Numerical Simulation of a Reciprocating-Mechanism Driven Heat Loop (RMDHL)." *Heat Transfer Research*.
8. M Sheikholeslami, S Soleimani, DD Ganji, Effect of electric field on hydrothermal behavior of nanofluid in a complex geometry, *Journal of Molecular Liquids* 213, 153-161.
9. Sheikholeslami, M., Soheil Soleimani, and D. D. Ganji. "Effect of electric field on hydrothermal behavior of nanofluid in a complex geometry." *Journal of Molecular Liquids* 213 (2016): 153-161.

10. S.M. Seyyedi, M. Dayyan, Soheil Soleimani, E. Ghasemi, Natural convection heat transfer under constant heat flux wall in a nanofluid filled annulus enclosure, *Ain Shams Engineering Journal* (2015) 6, 267–280.
11. E. Ghasemi, Soheil Soleimani, M.A. Almas, Finite Element Simulation of Jet Combustor Using Local Extinction Approach with Eddy Dissipation Concept, *Journal of Advanced Thermal Science Research*, 2014, 1, 57-65.
12. Soheil Soleimani, E. Ghasemi, M.A. Almas, Effects of Pressure Gradients on Energy Dissipation Coefficient, *Journal of Advanced Thermal Science Research*, 2014, 1, 71-77.
13. M. Alinia, M. Gorji-Bandpy, D.D. Ganji, S. Soleimani, E. Ghasemi, A. Darvand, Two-phase natural convection of SiO₂-water nano fluid in an inclined square enclosure, *Scientia Iranica B* (2014) 21(5), 1643-1654.
14. M. Sheikholeslami, R. Ellahi, M. Hassan, Soheil Soleimani, "A study of natural convection heat transfer in a nanofluid filled enclosure with elliptic inner cylinder." *International Journal of Numerical Methods for Heat & Fluid Flow* 24.8 (2014): 1906-1927.
15. E. Ghasemi, S. Soleimani, C.X. Lin, Secondary reactions of turbulent reacting flows over a film-cooled surface, *International Communications in Heat and Mass Transfer* 55, 93-101.
16. E. Ghasemi, S. Soleimani, C.X. Lin, RANS simulation of methane-air burner using local extinction approach within eddy dissipation concept by OpenFOAM, *International Communications in Heat and Mass Transfer* 54, 96-102.
17. M. Sheikholeslami, M. Gorji-Bandpy, D.D. Ganji, S. Soleimani, Heat flux boundary condition for nanofluid filled enclosure in presence of magnetic field, *Journal of Molecular Liquids* 193, 2014, 174-184.
18. M. Sheikholeslami, M. Gorji-Bandpy, D.D. Ganji, P Rana, S. Soleimani, Magnetohydrodynamic free convection of Al₂O₃-water nanofluid considering Thermophoresis and Brownian motion effects, *Computers & Fluids* 94, 2014, 147-160.
19. M. Sheikholeslami, M. Gorji-Bandpy, D.D. Ganji, S. Soleimani, Thermal management for free convection of nanofluid using two phase model, *Journal of Molecular Liquids*, 194, 2014, 179–187.
20. M. Sheikholeslami, M. Gorji Bandpy, R. Ellahi, M. Hassan, S. Soleimani, Effects of MHD on Cu–water nanofluid flow and heat transfer by means of CVFEM, *Journal of Magnetism and Magnetic Materials* 349, 2014, 188-200.